Università degli Studi
di Genova

Dark Matter induced annual modulation analysis in CUORE-0

Simone Copello

Supervisors:
Sergio Di Domizio
Marco Pallavicini

This thesis is submitted for the degree of
Doctor of Philosophy
XXIX cycle

March 21, 2017

Contents

List of Figures

List of Tables

Introduction

During my Ph.D. program I worked in the context of the CUORE collaboration on several tasks in different experimental fields. The primary goal of CUORE is the search of the neutrinoless double beta decay ($0\nu\beta\beta$) of ^{130}Te and it is approaching the data taking phase in Gran Sasso National Laboratories. Its predecessor, CUORE-0, took data from March 2013 to March 2015 and provided the most stringent limit on $0\nu\beta\beta$ half-life of ^{130}Te.

The main task I covered within the collaboration consisted in the development of the CUORE data acquisition system, by adapting the preexisting one, used for CUORE-0, to the new requirements. Since CUORE has $\sim$19 times as many as the CUORE-0 channels, it was necessary to move on from a single computer system to a multi-host system, able to acquire simultaneously six National Instruments chassis. For the same reason several user-based procedures have been automatized and parallelized. The new DAQ, described in chapter 3, manages the custom electronics via CANBus and uses a Postgres database to store settings information. In addition, a new raw data format permits to save the entire baselines and to apply an offline trigger, with lower energy thresholds. Aside from this, I took part in the CUORE cryostat commissioning: working on thermometry, run monitoring, very preliminary data acquisition and helping to solve temperature instability issues.

Finally I worked on the Dark Matter search in CUORE-0 by looking for the annual modulation signature. Indeed Dark Matter represents one of the most important open questions in fundamental physics and a strong effort is currently put into its direct detection. Such analysis is the topic of this thesis.

In the first chapter a theoretical introduction is provided both for neutrinoless double beta decay and Dark Matter, along with a brief overview on $0\nu\beta\beta$ experiments. In chapter 2 the experimental technique for Dark Matter direct search is discussed and the key elements of annual modulation signature are illustrated. In chapter 3 the CUORE and CUORE-0 experiments are presented; in particular two sections are dedicated to the CUORE data acquisition system and the CUORE cryostat commissioning. In chapter 4 the first

level of data processing is covered, from digitized samples to the CUORE-0 low energy spectrum. Finally, in chapter 5, the annual modulation analysis of CUORE-0 data is described and results are discussed.

Chapter 1

Neutrinoless double beta decay and Dark Matter

In this chapter two of the most important open questions of modern physics will be presented. The first is the neutrinoless double beta decay and represents the main scientific goal of the CUORE experiment. The Standard Model (SM) of particle physics, which describes the interaction between particles and thus, as far as we know, the fundamental constituents of the Universe, is probably one of the biggest milestones of the scientific process. For decades it has been in good agreement with the experimental observations, except for some anomalies. Some of these are related to neutrino physics, especially the origin of their mass. Neutrinoless double beta decay is a promising probe to investigate the neutrino nature and obtain a deeper comprehension of our Universe, beyond the SM.

In the second part of this chapter the Dark Matter problem will be presented. Dark Matter is the generic name that we use to designate a set of possible explanations for anomalies observed at the cosmological scale, mainly, but not only, related to gravitational effects. During the last century many hypothesis were introduced to explain these discrepancies, such as new theories for gravity or the presence of non-luminous celestial bodies inside the observed galaxies. Nevertheless the idea of a halo made of neutral particles, the Dark Matter particles, remains the most attractive one.

These two, apparently uncorrelated, problems of modern physics are associated by similar experimental techniques: as shown, an experiment designed for neutrinoless double beta decay search like CUORE can give a contribution also in the Dark Matter field.

1.1 Neutrinoless double beta decay

Double beta decay is basically the transition between two isotopes in which the atomic number changes by two units. Being a second order process it is suppressed with respect to the ordinary beta decay but, when this last process is energetically forbidden or strongly disfavored, it is possible to observe the double transition. The simplest decay of this kind is the two-neutrino double beta decay ($2\nu\beta\beta$):

$$(A, Z) \rightarrow (A, Z+2) + e^- + e^- + \overline{\nu}_e + \overline{\nu}_e \tag{1.1}$$

It doesn't imply any particular property of the involved particles and has been observed for several isotopes. Aside from this, we can imagine an other decay mode: the so called neutrinoless double beta decay ($0\nu\beta\beta$):

$$(A, Z) \rightarrow (A, Z+2) + e^- + e^- \tag{1.2}$$

Different from the $2\nu\beta\beta$, the $0\nu\beta\beta$ still remains hypothetical for the simple fact that we don't know any fundamental law that forbids it, but it has never been observed before. Its observation would answer to several fundamental questions related to neutrino nature: it would prove that lepton number is not conserved and that neutrinos are Majorana particles, which means that they are their own anti-particles, and could provide an explanation for the smallness of the neutrino masses. Furthermore the measurement of $0\nu\beta\beta$ decay half life could be the most promising way for determining the absolute neutrino mass scale with a sensitivity a few tens of meV.

1.1.1 A brief history of double beta decay

The idea of a double beta decay, formally the two-neutrino double beta decay was born in 1935 [17], one year after that Fermi created his weak interaction theory. Two years later Ettore Majorana suggested the idea that the neutrino ν and the antineutrino $\overline{\nu}$ are indistinguishable, in contradiction with the assumption that neutrinos are Dirac particles like all other known fermions. In particular neutrinos seem not to have a charge to highlight the distinction between particle and antiparticle (e.g. the electrical charge for electron and positron). Only if neutrinos were Majorana particles it would be possible, but not certain, to have a neutrinoless double beta decay ($0\nu\beta\beta$). In fact this interaction is possible only if the two produced neutrinos can, somehow, annihilate. In 1939 Wolfgang Furry [18] suggested to search for a $0\nu\beta\beta$ decay as proof of the nature, Majorana or Dirac, of neutrinos. At that time the chirality suppression of $0\nu\beta\beta$-decay was unknown, and, thanks to the advantage

in terms of phase-space, this reaction was considered dominant with respect to the $2\nu\beta\beta$-decay. For this reason, when several experiments set an half-life lower limit of the order of 10^{12} - 10^{15} years, bigger than the expected one, it was interpreted as a signal of the Dirac nature of neutrinos. In 1950 double beta decay of the isotope ^{130}Te was first observed by Ingram and Reynolds [19]; the half life was estimated in 1.4×10^{21} years. This prompted the introduction of the lepton number, which, if conserved, avoids the neutrinoless beta decay and allows $2\nu\beta\beta$ decay.

With the successive experiments the parity violation in weak interaction was discovered. In particular the observation of the polarization of the photon emitted back to back with respect to the neutrino in the decay of an excited atom of ^{152}Eu* [20], shows that neutrino spin is always anti-parallel to its momentum. This means that the helicity, which is the projection of the spin in the direction of the momentum, of the emitted neutrino is always negative, while it is positive in case of the emission of an anti-neutrino. This behavior was mathematically formalized in the vector - axial vector (V - A) theory of weak interactions. In this theory the concept of chirality was introduced. In the Dirac formalism, a particle can be seen as made of two independent chirality components called left-handed and right-handed

$$\psi = \psi_L + \psi_R \tag{1.3}$$

The charge-conjugation operator, which transforms a particle into its antiparticle and vice versa, swaps the two components:

$$(\psi)^C = (\psi_L)^C + (\psi_R)^C = \overline{\psi}_R + \overline{\psi}_L \tag{1.4}$$

where $(\psi)^C$ denotes the charge-conjugated state of ψ. The chirality is an intrinsic property of the particle and the weak processes, in this picture, produce neutrinos as chirality eigenstates, left-handed neutrinos (ν_L) and right-handed antineutrinos ($\overline{\nu}_R$), while the remaining ν_R and $\overline{\nu}_L$ can be called sterile, in the sense that they can not take part to any interaction.

From the experimental point of view we are able to measure only the helicity, which is the projection of the spin on the direction of the momentum and is not an intrinsic property but is related to chirality. For massless particles it is impossible to measure a different helicity by changing the reference frame, in this case the helicity becomes an intrinsic property of the particle and coincides with its chirality: a left-handed massless neutrino will always have negative helicity, according to the experimental observations. On the contrary, for massive particles it is possible to measure a positive (negative) helicity even if the chirality is negative (positive). The experimental evi-

dence of precise helicity states can be explained with chirality eigenstates, for massless or light neutrinos. This new theoretical framework reopened the question regarding the nature of neutrino.

If we consider $0\nu\beta\beta$ as a beta decay followed by the absorption of a neutrino by a neutron,

$$n \rightarrow p + e^- + \overline{\nu}_e^R, \qquad \nu_e^L + n \rightarrow p + e^- \tag{1.5}$$

we see that the neutrino produced in the first reaction has the wrong helicity for absorption by the neutron. For this reason the $0\nu\beta\beta$ decay is forbidden, for a massless neutrino, or strongly suppressed, for a light neutrino. Under the hypothesis of a light neutrino, this suppression could justify a half-life long enough to be compatible with the observed lower limits, without excluding the Majorana neutrino hypothesis.

More recently, data from oscillation experiments proved that neutrinos are massive and boosted the importance of $0\nu\beta\beta$ decay.

1.1.2 Neutrino oscillation

Neutrinos can be of three different kinds, that we call flavors: electron (ν_e and $\overline{\nu}_e$), muon (ν_μ and $\overline{\nu}_\mu$) and tau (ν_τ and $\overline{\nu}_\tau$). This definition formally represents the fact that, in a weak interaction, ν_e and $\overline{\nu}_e$ are associated with e^- and e^+, similarly ν_μ with μ leptons and ν_τ with τ leptons. These three states represent flavor eigenstates (and are necessarily orthogonal to each other). To take into account this and the fact that all the observed neutrinos (antineutrinos) that participate to a weak interaction have helicity of -1/2 (+1/2), the Standard Model (SM) describes neutrinos in flavor-chirality eigenstates and establishes that only ν_l^L and $\overline{\nu}_l^R$, for a fixed l, can take place in a weak interaction.

The first hint of neutrino oscillation raised from the observation of neutrinos produced by the Sun. Solar neutrinos represent a way to investigate the fusion reactions of a star because several of the involved reactions produce ν_e. In the 1960's the Homestake experiment by Raymond Davis and collaborators measured a flux significantly smaller than the one described by the Standard Solar Model [21]. This deficit was called "solar neutrino problem" and remained unsolved until 1998 when Super-Kamiokande's data [22] showed $\nu_\mu \leftrightarrow \nu_\tau$ oscillation evidence in atmospheric neutrino flux. In 2001 the SNO experiment [23] definitively proved that the deficit in solar neutrino flux was due to the conversion of ν_e in ν_μ and ν_τ. After that, the neutrino oscillation has been observed also for neutrinos produced in nuclear reactors and particle accelerators (for example by KamLAND [24][25], MI-

NOS [26][27], T2K [28][29], and NOνA [30], a general review can be found in [31], and in references there contained).

This behavior can be easily explained by assuming that neutrinos are massive and that the mass eigenstates do not correspond to the flavor eigenstates, but the firsts are a linear combination of the seconds, and vice versa. The Pontecorvo-Maki-Nakagawa-Sakata matrix (U_{PMNS}) describes how the states are mixed:

$$\nu_l^L(x) = \sum_{j=1,2,3} U_{lj}\ \nu_j^L(x), \qquad l = e, \mu, \tau \tag{1.6}$$

Where $\nu_j(x)$ are the mass eigenstates with mass m_j, and $\nu_l(x)$ are the flavor eigenstates.

U_{PMNS} that can be expressed as the combination of three rotations in the space of neutrino mass eigenstates $U_{PMNS} = R_{23}\tilde{R}_{13}R_{12}$:

$$R_{23} = \begin{pmatrix} 1 & 0 & 0 \\ 0 & c_{12} & s_{12} \\ 0 & -s_{12} & c_{12} \end{pmatrix}, \ R_{12} = \begin{pmatrix} c_{12} & s_{12} & 0 \\ -s_{12} & c_{12} & 0 \\ 0 & 0 & 1 \end{pmatrix},$$
$$R_{13} = \begin{pmatrix} c_{13} & 0 & s_{13}e^{-i\delta_{CP}} \\ 0 & 1 & 0 \\ -s_{13}e^{i\delta_{CP}} & 0 & c_{13} \end{pmatrix} \tag{1.7}$$

where s_{ij} and c_{ij} are respectively sine and cosine of the mixing angle θ_{ij} and δ_{CP} is the CP-violating phase.

To give a simple example of how the oscillation happens, assume to have a neutrino ν_l of flavor l produced by a certain source and detected by a detector after a flight of length L and a time of flight T. The state at the production time t_0 is expressed as a combination of the three mass states

$$|\nu_l(t_0)\rangle = \sum_{j=1,2,3} U_{lj}^*\ |\nu_j(t_0); \tilde{p}_j\rangle \tag{1.8}$$

where $|\nu_j; \tilde{p}_j\rangle$ indicates the state of mass m_j and four-momentum $\tilde{p}_j$ in the laboratory frame. After the time $T = t_f - t_0$, the probability to detect a neutrino of flavor l' is given by the square of

$$\langle\nu_{l'}(t_0)|\nu_l(t_f)\rangle = \sum_{j=1,2,3} \langle\nu_{l'}(t_0)|\ U_{l'j}D_jU_{jl}^\dagger\ |\nu_l(t_0)\rangle \tag{1.9}$$

where $D_j = e^{-i\tilde{\mathbf{p}}_j(\mathbf{x}_f - \mathbf{x}_0)} = e^{-i(E_jT - p_jL)}$ is the time evolution operator for the state of mass m_j. In particular these probabilities are related to terms

Parameter	NO (bfp $\pm 1\sigma$)	IO (bfp $\pm 1\sigma$)
$\sin^2\theta_{12}$	$0.304^{+0.013}_{-0.012}$	$0.304^{+0.013}_{-0.012}$
$\theta_{12}(^\circ)$	$33.48^{+0.78}_{-0.75}$	$33.48^{+0.78}_{-0.75}$
$\sin^2\theta_{23}$	$0.452^{+0.052}_{-0.028}$	$0.579^{+0.025}_{-0.037}$
$\theta_{23}(^\circ)$	$42.3^{+3.0}_{-1.6}$	$49.5^{+1.5}_{-2.2}$
$\sin^2\theta_{13}$	$0.0218^{+0.0010}_{-0.0010}$	$0.0219^{+0.0011}_{-0.0010}$
$\theta_{13}(^\circ)$	$8.50^{+0.20}_{-0.21}$	$8.51^{+0.20}_{-0.21}$
$\delta_{CP}(^\circ)$	306^{+39}_{-70}	254^{+63}_{-62}
$\Delta m^2_{21}(10^{-5}eV^2)$	$7.50^{+0.19}_{-0.17}$	$7.50^{+0.19}_{-0.17}$
$\Delta m^2_{3l}(10^{-3}eV^2)$	$+2.457^{+0.047}_{-0.047}$	$-2.449^{+0.048}_{-0.047}$

Table 1.1: *Three-flavor neutrino oscillation parameters assuming Normal Ordering (NO, second column) and Inverted Ordering (IO, third column), NO and IO are explained in section 1.1.3. Data from [15]*

proportional to $\sin^2\frac{\Delta m^2_{ij}}{4E}L$ where Δm^2_{ij} is the difference of the square of the masses m_i and m_j and E is the energy of the emitted neutrino. The updated values of θ_{ij}, Δm^2_{ij} and δ_{CP} can be found in table 1.1.

In conclusion, the observation of the oscillation and the confirmation of a survival probability proportional to $\sin^2\frac{\Delta m^2_{ij}}{4E}L$ proved that neutrinos can be described with three non-degenerate mass eigenstates or, in other words, that at least two over three neutrinos are massive. This certainty gave new interest in $0\nu\beta\beta$ decay because, in a weak interaction such as the one described in formula 1.5, if neutrinos are massive and thus helicity doesn't correspond to chirality, it is still possible to have the production of a ν ($\overline{\nu}$) with helicity equal to +1/2 (-1/2) that can be absorbed by the second neutron.

1.1.3 Neutrinoless double beta decay implications

The oscillation experiments represent an evidence of lepton flavor violation, which means that the number of leptons of a certain flavor, minus the number of anti-leptons of the same flavor (L_i with $i = e, \mu, \tau$) is not conserved. At the same time, as far as we know, the total number of leptons ($L = L_e + L_\mu + L_\tau$) is conserved in every process. This rises the suspect that the conservation of the leptonic number is a law of nature. On the other hand, since we do not know any fundamental reason for this conservation law, it is also possible that its validity is an approximation, broken at some energy scale. The observation of $0\nu\beta\beta$ decay would be an incontrovertible evidence of lepton

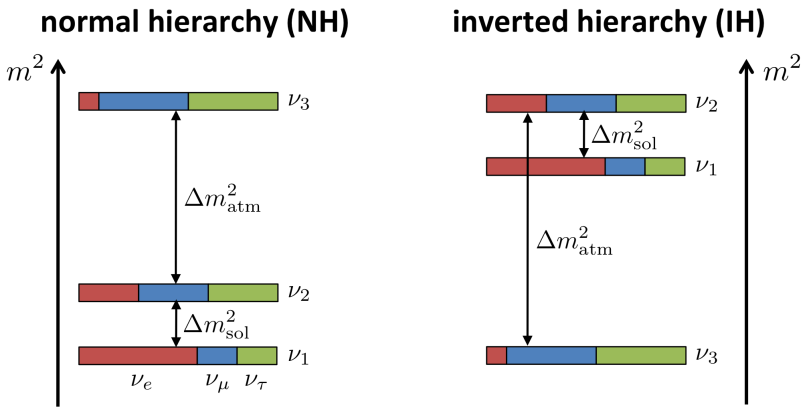

Figure 1.1: *Neutrino oscillation experiments has been used to measure several parameters related the neutrino mass mixing, such as the mixing angles and the square difference between the mass eigenvalues, but they cannot discriminate between these two possible scenarios.*

number violation, regardless of how it takes place.

In case of Majorana particles, the matrix U_{PMNS} is multiplied by a diagonal matrix, which contains the two additional CP-violating Majorana phases α_1 and α_2. Oscillation experiments give us indication about the values of the mixing angles (see table 1.1) but leave open other fundamental questions. The first is the absolute mass scale, in other words we do not know the value of the lightest ν ($m_{lightest}$) and, as consequence, the other two values. In addition to this, data from atmospheric neutrinos tell us the difference between the two neutrino masses m_3 (by definition the most splitted eigenstate) and m_2 (the heaviest of the two remainig eigenstates) through the term δm^2_{23} but the two cases $m_2 < m_3$ and $m_2 > m_3$ are both valid. We can imagine two possible scenarios for the neutrino masses ordering: the *normal ordering* in which $m_1 < m_2 < m_3$ and the *inverted ordering* in which $m_3 < m_1 < m_2$. Combining these with different values of $m_{lightest}$ we get three main possibilities:

- *Normal hierarchy*: $m_1 \ll m_2 < m_3$
- *Inverted hierarchy*: $m_3 \ll m_1 < m_2$
- *Quasi-degenerate*: $m_1 \simeq m_2 \simeq m_3$

In principle the absolute scale could be evaluated also from astrophysical observations that are sensitive to the sum of the three neutrino masses [32] but the obtained limits can vary depending on the adopted technique and on

the considered observation. A global analysis can be found in [33], in which the upper bound $\sum m_\nu < 0.14\ eV$ (95% C.L.) is reported.

Regarding direct measurements, the ordinary beta decay process can be used to measure the value of the effective neutrino mass of β decay

$$\langle m_\beta \rangle = \sqrt{c_{12}^2 c_{13}^2 m_1^2 + c_{13}^2 s_{12}^2 m_2^2 + s_{13}^2 m_3^2} \tag{1.10}$$

Since the ordinary beta is a three body decay, the emitted β particle shows a continuous spectrum. $\langle m_\beta \rangle$ can be evaluated by measuring the difference between the Q-value and the maximum energy of the β (the so-called end-point, corresponding to the case in which the neutrino is at rest). On the contrary the $0\nu\beta\beta$ decay, in addition to the fact that it is sensitive to the Majorana phases α_1 and α_2 that appear in the $0\nu\beta\beta$ decay effective neutrino mass $\langle m_{\beta\beta} \rangle$:

$$\langle m_{\beta\beta} \rangle = c_{12}^2 c_{13}^2 e^{2i\alpha_1} m_1 + c_{13}^2 s_{12}^2 e^{2i\alpha_2} m_2 + s_{13}^2 m_3 \tag{1.11}$$

offers an alternative and, for some aspects, more sensible measurement. Assuming the $0\nu\beta\beta$ decay to happen through the exchange of a light left handed neutrino, the effective mass can be extracted from the decay time. This equation shows how the inverse of the half-life can be expressed as product of three terms.

$$\left(T_{1/2}^{0\nu}\right)^{-1} = G_{0\nu} \langle m_{\beta\beta} \rangle^2 |M_{0\nu}|^2 \tag{1.12}$$

$G_{0\nu}$ is the phase space factor, $\langle m_{\beta\beta} \rangle$ is the effective mass term and $M_{0\nu}$ is the nuclear matrix element, and is related to the nuclear physics involved in the process. While the phase space factor can be calculated with some uncertainties, the nuclear matrix element is the biggest source of uncertainty in this calculation. It depends on the structure of the parent and daughter nuclei and consists in a many body problem that cannot be analytically solved; for this reason the assumption of an approximated model is necessary. The obtained values are strongly model-dependent and in some cases they differ by a factor two or three. Three main families of models can be identified: the quasi-particle random phase approximation [34], the nuclear shell model [35] and the interacting boson model [36].

Even if the $0\nu\beta\beta$ decay search offers good experimental perspectives, it remains a big technological challenge. Different from $2\nu\beta\beta$, whose signature is a continuous spectrum as well as β decay, $0\nu\beta\beta$ decay is expected to produce a peak at specific nucleus-dependent energy $Q_{\beta\beta}$ because it is a second-order two body decay. Thus the observation of this hypothetical process consists in counting the number of events in a predetermined region

of interest (ROI). The absence of particular features of its signature and the background uncertainty make that the simple observation of an excess in the ROI can not be considered an evidence of $0\nu\beta\beta$ decay. Such excesses will be considered an evidence only when obtained for several isotopes, so the experimental effort must necessarily involve different nuclei. A good comprehension of the nuclear matrix elements is therefore required to compare results from different experiments.

1.1.4 Experimental effort

The most significant parameter to categorize a neutrinoless double beta decay experiment is the sensitivity F (or factor of merit). It is defined as the process half-life corresponding to the maximum signal that can be hidden by the background fluctuations for a given confidence level. Since the number of background events per unit of energy can be assumed to be proportional to detector mass (in good approximation) and acquisition time, we have that the expected number of background events is $N_b = B \cdot T \cdot M \cdot E$, where B is the number of background events per unit of mass, energy and time, T is the acquisition time, M the detector mass and E is the energy interval where the search is performed (normally an interval equal to 1 FWHM of the energy resolution is chosen). Its standard deviation is $\sigma_N = \sqrt{B\ T\ M\ E}$. By using the relation that links the number of events to the half-life, we get

$$F_{1\sigma} \ = \ \ln 2 \ N_{\beta\beta} \ \epsilon \ \frac{T}{M_b} \ = \ \ln 2 \ \frac{x \ \eta \ \epsilon \ N_A}{A} \sqrt{\frac{M \ T}{B \ E}} \tag{1.13}$$

where ϵ is the detection efficiency and $N_{\beta\beta}$ is the number of double beta decaying nuclei which can be written with the Avogadro number N_A, the compound molecular mass A, the number of beta beta decaying atoms per molecule x and their isotopic abundance η. The particular case in which the background level is so low that the expected number of background events, in the region of interest, during the entire experiment life is not larger than one ($N_b = B \cdot T \cdot M \cdot E \lesssim 1$) is called "zero background". Under this condition, a better approximation for the sensitivity is obtained by

$$F_L^{0B} \ = \ \ln 2 \ \frac{x \ \eta \ \epsilon \ N_A}{A} \frac{M \ T}{n_L} \tag{1.14}$$

where n_L is a value that depends on the confidence level and the number of observed events.

Equations 1.13 and 1.14 highlight the most important features of a $0\nu\beta\beta$ decay experiment: large mass, long measuring time and background suppression. These criteria drives the detection strategies, but their simultaneous op-

timization is rarely possible. Long measuring time, for the current-generation experiments (prototypes), means one or few years, while the next-generation ones will take data for several years. Background reduction is obtained by placing the experiments in underground laboratories and by using active or passive shielding in addition to a very careful material selection for the detector itself and the components that can not be shielded. In some cases the detectors are able to register different signals, such as scintillation, ionization, thermal variation, and to get information such as electron energies or event topology. In these cases also the particle discrimination contributes to the background reduction. The large mass requirement is often satisfied by using homogeneous experiments, in which the detector coincides with the decay source and, more in general, it drives the research and development projects (R&D) to scalable technologies. To give an indication, the investigation of the inverted hierarchy ($\langle m_{\beta\beta} \rangle \geq$ tens of meV), which represents the current-development main goal, requires active masses of the order of one ton. This aspect also affects the choice of the isotope because of the cost, the isotopic natural abundance and the isotopic enrichment perspectives. For this last reason, the number of considered isotopes is restricted to few elements: mainly ^{76}Ge, ^{82}Se, ^{100}Mo, ^{130}Te and ^{136}Xe.

Up to now the only isotope that produced a positive claim is the ^{76}Ge ($Q_{\beta\beta}$=2039 keV) from the Heidelberg-Moscow experiment (HdM), which measured $T^{0\nu}_{1/2} = (2.23^{+0.44}_{-0.31}) \cdot 10^{25}$ years [37]. ^{76}Ge is used also by the GERDA experiment [2] in Gran Sasso National Laboratories, Italy. The GERDA detectors (High-Purity Germanium detectors, HPGe) are semiconductors with 86% of ^{76}Ge. They are operated inside a liquid argon cryostat, which provides both the cooling and a shielding against external gamma particles, surrounded by an ultra-pure water shield used as Cherenkov detector for muons. During GERDA Phase I, from November 2011 to May 2013, they collected an exposure of 21.6 kg·year. In the 10 keV wide ROI seven events were observed, while 5.1 ± 0.5 were expected. After the pulse shape discrimination cut, no event remained in the energy window $Q_{\beta\beta} \pm \sigma_E$. The limit on the half-life is $T^{0\nu}_{1/2} > 2.1 \cdot 10^{25}$ years (90% C.L.). That limit consistent with the ones found by IGEX and HdM experiments, and, by combining the three limits, we obtain $T^{0\nu}_{1/2} > 3.0 \cdot 10^{25}$ years (90% C.L.) which contradicts the positive claim from HdM.

The most investigated isotope, thanks to EXO-200 and KamLAND-Zen experiments, is probably ^{136}Xe. EXO-200 [3] is a cylindrical time projection chamber (TPC) filled with about 200 liters of liquid xenon (LXe). The background reduction is obtained by placing the detector in an underground facility in New Mexico (at a depth of more than 1500 meters water equiva-

lent), with a shield of ∼50 cm of cryogenic fluid (HFE-7000) surrounded by more than 25 cm of lead in all directions and a muon veto made of plastic scintillators. The LXe is enriched to 80.6% in ^{136}Xe (Q = 2457.83 ± 0.37 keV). The x-y-z reconstruction provided by the TPC, allows to define a fiducial volume used to reject the events that occur close to the LXe boundary layer and thus to reduce the contamination induced by the container. The x-y-z reconstruction is also used to keep single-site events (SS) and reject multi-site events (MS, which are typically due to γ multiple scattering). In 2014 EXO-200 reached a half-life sensitivity of 1.9·10 ^{25} years thanks to an exposure of 100 kg·year and provided a half-life lower limit (at 90% C.L.) for $0\nu\beta\beta$ decay of ^{136}Xe of $1.1{\cdot}10^{25}$ years.

For sure the large mass requirement is reached by the KamLAND-Zen experiment [38]. Its detector consists of 13 tons of Xe-loaded liquid scintillator (Xe-LS), for a Xe-content of ∼320 kg, contained in a 3.08-m-diameter spherical inner balloon located at the center of the preexisting KamLAND detector. The inner balloon is surrounded by 1 kton of liquid scintillator (LS) acting as active shield. The scintillation photons are viewed by 1,879 photomultiplier tubes (PMTs) mounted on the inner surface of the containment vessel. The isotopic abundances in the enriched xenon were measured to be ∼90% ^{136}Xe, and ∼8% ^{134}Xe. By combining results from two data acquisition phases, respectively before and after a ^{110m}Ag purification campaign, they obtained a lower limit for the $0\nu\beta\beta$ decay half-life of $1.07{\cdot}10^{26}$ years at 90% C.L. corresponding to $m_{lightest} < (180 - 480)$ meV and $\langle m_{\beta\beta}\rangle < (61 - 165)$ meV (both are 90% C.L.). Uncertainties on $m_{lightest}$ and $\langle m_{\beta\beta}\rangle$ are due to nuclear matrix elements spread obtained by considering different nuclear models.

The event topology reconstruction was performed by NEMO-3 experiment in Laboratoire Souterrain de Modane, France. $\beta\beta$ events were emitted by thin source foils surrounded by trackers (Geiger cells) and calorimeters (plastic scintillators coupled with low radioactivity PMT's). The trackers allow a reconstruction of the decay vertex, with a resolution of $0.5{\times}0.5{\times}8\ mm^3$, while the calorimeters provide an energy resolution of $\simeq 6\%/\sqrt{E/MeV}$ (1σ). Moreover the detector is placed into a 25 G magnetic field in order to improve the particle identification. The source foils contain seven $0\nu\beta\beta$ candidates: the most relevant are ^{100}Mo ($\simeq$ 7 kg) and ^{82}Se ($\simeq$ 1 kg) in addition to smaller quantities of ^{130}Te, ^{116}Cd, ^{150}Nd, ^{96}Zr and ^{48}Ca. The detector took data from 2003 to 2011 and provided the following half-life lower limits (90% C.L.): $2{\cdot}10^{22}$ years for ^{100}Mo [39], $2.2{\cdot}10^{23}$ years for ^{82}Se [40], $2.0{\cdot}10^{22}$ years for ^{48}Ca [41], $1.0{\cdot}10^{23}$ years for ^{116}Cd [42] and $2.0{\cdot}10^{22}$ years for ^{150}Nd [43]. The same strategy for event topology reconstruction will be adopted in the

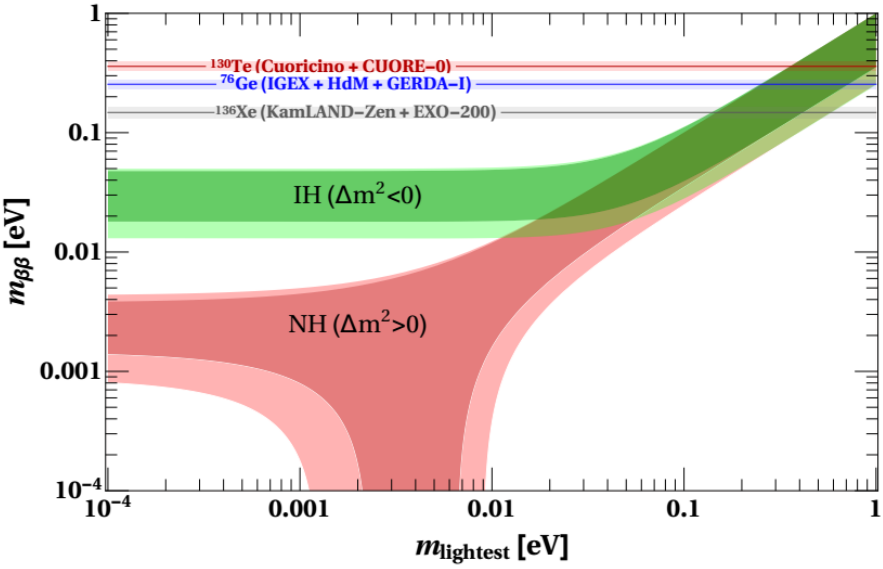

Figure 1.2: *Constraints on effective double beta decay neutrino mass $m_{\beta\beta}$ as a function of the lightest neutrino mass. For inverted (IH, green) and normal (NH, red) hierarchy. The central dark bands are derived from the best-fit neutrino oscillation parameters while the lighter bands include their uncertainties (3σ). The horizontal bands show the current upper limits (90% C.L) for different isotopes: (red) ^{130}Te from CUORE-0 and Cuoricino [1], (blue) ^{76}Ge from Gerda, IGEX and HDM [2], (grey) ^{136}Xe from EXO-200 [3] and KamLAND-Zen [4]. Picture from [5].*

next-generation experiment SuperNEMO [44].

Last the CUORE-0 experiment [11], that will be described in section 3.5, provided the most stringent limit on ^{130}Te $0\nu\beta\beta$ decay rate. The half-life lower limit for ^{130}Te is $T^{0\nu}_{1/2} > 2.7 \cdot 10^{24}$ years (90% C.L.) that can be combined with the predecessor Cuoricino to obtain $T^{0\nu}_{1/2} > 4.0 \cdot 10^{24}$ years (90% C.L.) [45].

Figure 1.2 summarizes the current status of $0\nu\beta\beta$ search in terms of upper limits of the $0\nu\beta\beta$ decay effective neutrino mass $\langle m_{\beta\beta} \rangle$. The relationship between $\langle m_{\beta\beta} \rangle$ and the lightest neutrino mass $m_{lightest}$ is established by equation 1.11, by assuming normal or inverted hierarchy.

1.2 The Dark Matter problem

The history of Dark Matter (DM) begins in 1930 when the first data implying non luminous matter was collected. The dutch astronomer J. Oort, while studying the Doppler shift in stars spectra within the galactic disk, concluded that the measured velocities could not be explained with the gravitational mass of visible stars only. Soon after, in 1933, the Swiss astronomer F. Zwicky came to the same conclusion by observing the Coma galaxy clusters [46]. Other independent studies, such as the gravitational lensing or the cosmic microwave background, confirmed this hypothesis later. From 1930 up to now, a lot of effort has been put into the DM field, and some upper limits and estimation have been evaluated, but our knowledge of DM has not changed very much since the first observations. The most precise measurement of the CMB [47], combined with the results from the simulations of the formation of the large scale structures, such as galaxy and galaxy clusters, indicates that baryonic matter only contributes to 4.9% of the total mass-energy of the Universe, while DM represents 26.8%. The remaining 68.3% is called dark energy, a mysterious force thought to be responsible for accelerating the expansion of the Universe. Apart from this, we still ignore the nature of DM: we don't know what it is made of, if it is a particle (or a set of particles) beyond the Standard Model or, even, if it is due to a gravitational theory different from the one we know. For this reason DM remains one of the most important and challenging mystery of particle physics and cosmology.

1.2.1 Dark Matter evidences

The earliest evidence for DM at the galactic scale comes from the observation of the angular velocity of stars, or gas, as a function of the distance from the galaxy center. The velocity of a star is typically obtained by the shift of the 21 cm wavelength line of hydrogen, due to the Doppler effect. By comparing the gravitational attraction, given by Newton's law, to the centripetal force required to have a circular and stable orbit, we easily obtain the relation between the speed of a body and its distance from the center of the galaxy

$$v(r) \propto \sqrt{\frac{M(r)}{r}} \tag{1.15}$$

where $M(r)$ is the mass contained is a sphere, concentric to the galaxy, of radius r. Thus, where r is big enough to consider $M(r)$ independent from r, we have $v(r) \propto r^{-1/2}$. Several studies performed on spiral galaxies proved that the velocity outside the visible mass is approximately constant up to the largest values of r where it can be measured. This behavior can

be explained by assuming the presence of a dark galactic halo with a mass density $\rho(r) \propto 1/r^2$. At some point this mass density has to drop down faster than $1/r^2$ in order to keep the total mass finite, but we don't know where it happens. An important assumption that we do is that the Dark Matter halo is spherical, differently from the barionic matter which collapses to form a disk (to give an indication, the Milky Way has a radius of $\sim 10Kpc$ and height $\sim 0.5kpc$). This is a direct consequence of the fact that barionic matter strongly self-interacts with itself and has an efficient (on the Universe time scale) way to dissipate its energy, so during the collapse it flattens itself, still conserving the angular momentum. On the contrary, the DM halo cannot dissipate its energy at the same rate and remains in a spherical shape for a longer time.

It has been shown [48] that, for some galaxies, such a high angular velocity would allow stars to escape the galactic gravitational field if DM did not exist. In general this kind of considerations lead to a composition of the Universe in which $\Omega_{DM} \gtrsim 0.1$ where $\Omega_x \equiv \rho_x/\rho_{crit}$ is the mass density ratio and ρ_{crit} is the critical mass density that characterizes a flat Universe, as it seems to be.

When we move to larger scales we observe similar phenomena in galaxy clusters. In this case the measurements concern the peculiar velocities of the galaxies inside the cluster, that can be used to estimate the potential energy thanks to the virial theorem. Also in this case the gravitational potential cannot be explained by the visible mass only, but the obtained value $\Omega_{DM} \simeq 0.2$ is larger than in the previous case.

Another technique to estimate the gravitational field of a galaxy cluster is the weak gravitational lensing. Gravitational lensing consists in measuring the changes in the light path - or equivalently, from general theory of relativity, the space-time structure distortion - produced by the presence of matter. Massive objects can, in fact, modify the space-time around them to the point that an observer can see curved or multiple images of the source of light.

More quantitatively, the deflection angle α of a photon passing by a point mass M with impact parameter b is

$$\alpha = \frac{4G_N M}{c^2 b} \tag{1.16}$$

where G_N is the gravitational constant and c is the speed of light in vacuum. The practical effect is that the observer perceives the source in an apparent position which is shifted with respect to its real position. The lensing effect can be used to estimate the mass distribution between the observer and the

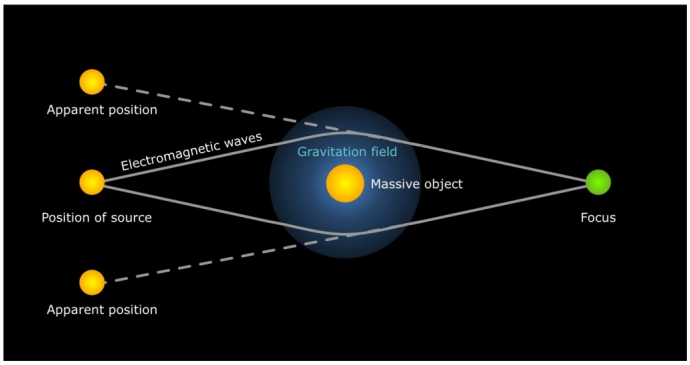

Figure 1.3: *The mass changes the space-time structure and this causes the light to curve its path in its proximity. In some cases the observer can perceive several images of the same source of light. This effect is used to reconstruct the mass distribution between the observer and the source.*

light source and, when used to evaluate the mass of a cluster, it leads, again, to a gravitational potential stronger that the one expected by considering the visible mass only.

One of the most spectacular applications of the gravitational lensing technique is provided by the so-called "Bullet cluster" 1E0657-56 [49][50]. It is a galaxy cluster, shown in figure 1.4, which is arising from the collision of two sub-clusters. Interstellar plasma gas, which represents the dominant part of the cluster baryonic mass, can be tracked by observing its X-ray emission (the pink spots in figure). According to its self-interacting nature, the plasma clouds, after the sub-cluster crossing, appears slowed down with respect to the galaxies that, instead, can be considered collisionless and proceed forward. In parallel, gravitational lensing is used to reconstruct the mass distribution. In this case the dominant mass fraction (the blue spots in figure) is found in correspondence of the galaxy sub-clusters, and not in the plasma gas. This fact is interpreted as the presence of a collisionless DM halo that proceeds (almost) without interaction, as well as the galaxies; on the contrary the self-interacting plasma, which is slowed down by the collision, has a negligible gravitational effect even if it is the most relevant baryonic mass.

The cited techniques can give indications about the DM density in delimited regions such as galaxies or galaxy clusters and cannot be used to estimate the total DM amount in the Universe. Observations at the biggest scale come from studies on the so-called Cosmic Microwave Background (CMB). Even if its existence had been previously predicted, the microwave background was accidentally discovered in 1965, by A. Penzias and R. Wilson [51], who received the Nobel Prize 13 years later. The CMB is an electromagnetic radiation that follows the black-body spectrum corresponding to a temperature

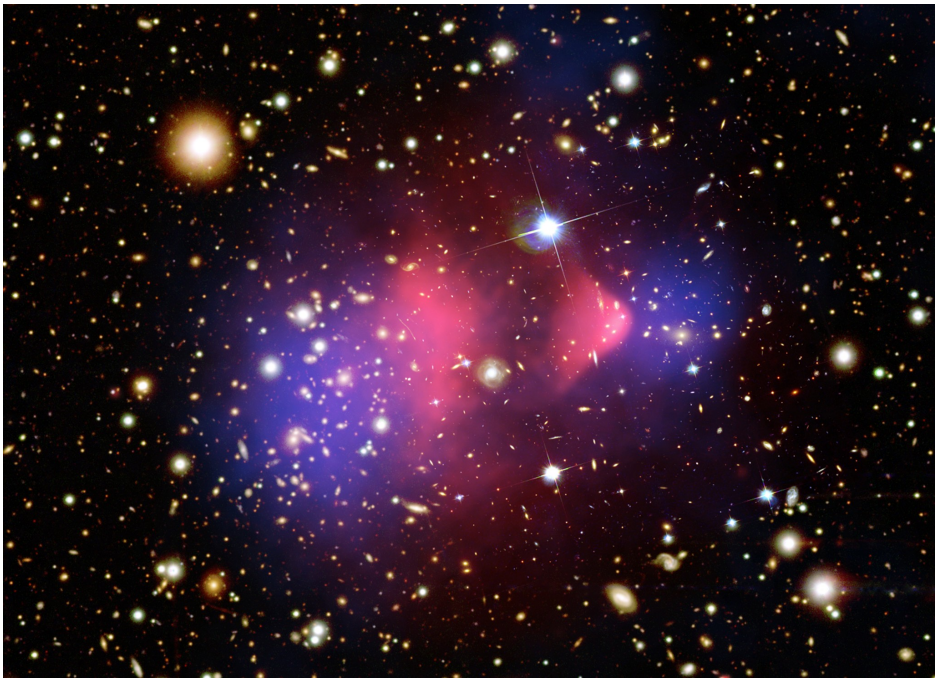

Figure 1.4: *The Bullet cluster 1E0657-56. The pink halos show the plasma clouds distribution according to their X-ray emission; the blue halos represents the mass distribution obtained by means of the gravitational lensing effect. If the crossing sub-clusters were made of baryonic matter only, the mass distribution should practically correspond to the plasma gas. Whereas most of the sub-clusters mass seems to have proceed, without relevant interactions, as well as the involved galaxies.*

of T = 2.726 K and it is isotropic up to a part over 10^5. By subtracting the constant component of its intensity, the remaining fluctuation (visible in figure 1.5) can be used for testing cosmological models and for setting stringent constraints on them, because its anisotropies bring information related to the formation of the first structures of the Universe. In particular it can be used to extract physical information such as baryonic and matter density. From the last years the CMB is measured for this purpose, with increasing precision, by different experiments, like WMAP or Planck. In particular the Planck experiment, an Europen Space Agency mission launched in 2009, has recently published the results obtained from data of 2015 [6]. For a base cosmological model, the fit performed with this new data, in combination with CMB lensing measurements, gave these parameters (68% confidence levels)

$$\Omega_b h^2 = 0.02226 \pm 0.00023 \qquad \Omega_{nbm} h^2 = 0.1186 \pm 0.0020 \tag{1.17}$$

where h is the Hubble constant in units of 100 $km/(s\ Mpc)$ and Ω_{nbm} is the density ratio of non-baryonic matter. This means that DM density, whatever it is, is about five times the barionic "ordinary" matter density. From the same analysis the updated value of the Hubble constant $h = 67.8 \pm 0.9 km/(s\ Mpc)$ is obtained. It must be noticed that, even if the non-baryonic mass represents most of the total amount of Dark Matter, a small fraction of barionic matter could contribute to the described gravitational discrepancies.

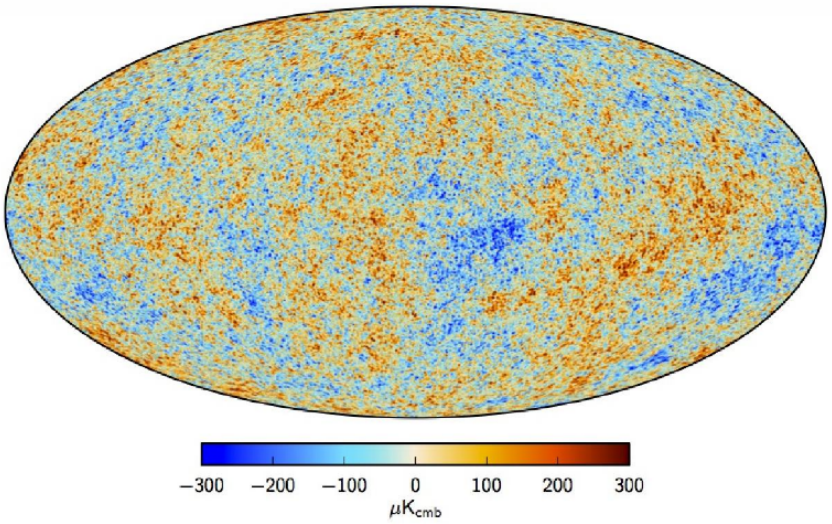

Figure 1.5: *CMB intensity map, after the subtraction of the constant component, at 5' resolution derived from the joint baseline analysis of Planck, WMAP, and 408 MHz observations [6].*

The local DM density is a relevant parameter, because, as explained in chapter 2, its value is particularly important for the interpretation of data of a large class of experiments. Combining observations of our galaxy with data from other galaxies, such as the rotation curves, we obtain an estimation of such value (68% C.L.) [52]

$$\rho_{DM}^{local} = (0.39 \pm 0.03) GeV/cm^3 \tag{1.18}$$

1.2.2 Dark Matter candidates

Before to enumerate the particles that could compose the Dark Matter, it is necessary to make a clarification. The observed gravitational effects could have, in principle, an origin different from the presence of a halo of neutral particles. In particular two different approaches have been proposed. The first one attempts to explain the discrepancy between the measured gravity and the estimated amount of matter by assuming the presence of non-luminous celestial bodies inside the observed galaxies. These bodies, generically called MACHOs (MAssive Compact Halo Objects), are massive formations such as brown dwarfs, neutron stars, black holes and, more in general, the objects for which the ratio between the emitted light and the mass is significantly small. The gravitational microlensing technique, adopted to estimate the gravitational contribution of MACHOs, by MACHO, EROS and OGLE collaborations, show that the barionic component of DM is only few parts per cent of the total halo mass [53]. Even if a part of the observed gravitational effects is probably due to non-luminous bodies, the presence of a large fraction of non-barionic matter is still required.

A second approach tries to justify the attractive force by modifying the gravitation theory. The Modified Newtonian Dynamics (MOND) theories, originally introduced by Mordehai Milgrom during the 80's [54], apply corrections to the dynamic laws such as

$$\overrightarrow{F} = m\mu(a/a_0)\overrightarrow{a} \tag{1.19}$$

where $a = |\overrightarrow{a}|$ and a_0 is a reference acceleration. In Newton dynamics it is $\mu(a/a_0) = 1$ for every value of a, while in some MOND theories we have $\mu(a/a_0) \simeq 1$ when $a \gg a_0$ and $\mu(a/a_0) \propto a$ when $a \ll a_0$. Even if these theories are well capable to reproduce the observations at galactic scale [55], they seem inappropriate to describe the phenomenology at larger scales, such as the structure formation or the Bullet cluster.

Taking into account all the observations explained in previous section, the studies of the CMB anisotropies, and analysis of structure formation

in the Universe, indicate that the hypothesis of a non-interacting particles gas, surrounding galaxies and galaxy clusters, remains the most convincing. This unknown particle or, in principle, set of particles must satisfy some conditions.

- DM must be electrically neutral and, more in general, it must interact very weakly with the electromagnetic radiation, otherwise we would be able to detect them by observing its radiation;
- It must be stable, at least, at the cosmological time scale;
- It must match the expected relic density.

In addition to this, simulations of structures formation suggest that DM particles must be mainly "cold". In this context, cold means that they were non-relativistic at the beginning of the of galaxies formation. The reason is that, since the structures (gas clouds earlier, galaxies and galaxy cluster later) are originated from interstellar gas density fluctuations, relativistic particles compensate for these fluctuations and obstacle the gravitational collapse process. Of course, results from such simulations present also some inconsistencies [56]. The most relevant are *Missing Satellites Problem* where too many satellite galaxies around the Milky Way are predicted; *Cusp/Core Controversy* where the predicted DM density profile at the center of some dwarf galaxies presents a peak higher than the "observed" one; and *Too Big to Fail Problem* in which the dwarf galaxies are larger than the observed ones. At least the first and the second discrepancies could be solved by introducing a component of "warm" DM, because its free-streaming length, longer than the one of cold Dark Matter, has the effect of to wash out structure formation on that scale.

If we look at the Standard Model of particle physics we see that the natural candidate for DM are neutrinos. They are indeed neutral, weakly interacting, stable and the oscillation phenomenon reasonably proved that they are massive. Unfortunately, as for MACHOs, neutrinos can contribute to the fraction of non-luminous mass of the Universe but they do not exclude the presence of other DM particles for two reasons. The small mass qualify them as "hot" DM and their relic density, which results to be $\Omega_\nu h^2 \leq 0.0062$ (95% C.L.) from CMB studies, is too small. This leads to the necessity of new physics beyond the SM to include new candidates. The list of candidates beyond the SM includes sterile neutrinos, axions, supersymmetry particles and Kaluza-Klein bosons. A detailed review on DM candidates can be found in [57] and in the references there contained.

Among these hypotheses, sterile neutrinos are probably the most easy-to-include into the Standard Model. We know, from the Large Electron-Positron collider measurement of the decay rate of the Z^0 boson, that only three neutrinos couple to the Z^0 boson. In the meanwhile we cannot exclude the existence of a fourth neutrino as long as it doesn't participate to weak interactions. For this reason such hypothetical neutrino is called sterile neutrino. It can be introduced by a minimal extension of the SM, by including the three right-handed neutrinos as singlets under the SM gauge group. They could be, in principle, more massive than the left-handed ones but the requirement of a long half-life puts an upper limit on their mass. In particular, assuming a sterile neutrino of mass M_S to decay mostly into two neutrinos and one anti-neutrino, its decay time is proportional $1/M_S^5$. Being the age of the Universe $\sim 10^{15} sec.$, its mass should be of the order of keV.

The existence of axions was originally postulated in '70s to solve the strong CP problem in quantum chromodynamics (QCD). They are pseudo Nambu-Goldstone bosons associated with the spontaneous breaking of a new global U(1) symmetry called "Peccei-Quinn" symmetry. A coherent oscillation of the axion field could produce physical axion quanta of mass of the order of 10^{-4} eV. For such small masses, the expected relic density shoud be ~ 1, and axions could contribute to the DM halo. Such axions would be produced in the early Universe with zero momentum and act as cold DM. Moreover, the small mass doesn't imply the necessity for axions to be "hot" (relativistic) DM because the weak coupling to the other SM particles excludes the thermal equilibrium.

A more exotic explanation can be found within the hypothetical Supersymmetry theories (SUSY). As well established in the SM every particle has its anti-particle, with same mass, same spin, but all opposite quantum numbers. In SUSY models a second symmetry is postulated, for which every particle has a second partner called the supersymmetric partner (or simply superpartner). This new symmetry is called R-parity and it leads to the new quantum number R, defined as:

$$R \equiv (-1)^{3B+L+2s} \tag{1.20}$$

where B is the barionic number, L is the leptonic number and s is the spin. It can take two values: $R = 1$ for standard particles and $R = -1$ for supersymmetryc particles. The important feature of this hypothesis is that the spin of a supersymmetryc particle is half unit different from the one of the standard partner, so that the partner of a fermion is a boson and vice versa. Thanks to this property, SUSY models are able to fix the so called hierarchical problem of SM, which is the fact that there is no apparent rea-

son for a so big difference between the particle masses. Some models assume the R-parity to be exact and thus cannot be violated; under this hypothesis the lightest supersymmetryc particle (LSP) becomes stable and thus a good DM candidate. Since the R-parity conserves the electric charge, the LSP must be the partner of a neutral particle to be a good DM candidate. The partner of a neutral boson is called neutralino and can be a bino ($\widetilde{B}$, partner of B), a wino ($\widetilde{W}$,partner of W) or an higgsino ($\widetilde{H}$, partner of H). These superpartners can be mixed into four Majorana fermionic mass eigenstates, the lightest of which is called χ. Otherwise the LSP could be a boson: the superpartner of the neutrino, called sneutrino. The main problem of these theories is that, even in their minimal version, they depend on a large number of unknown parameters, such as the superparticle masses and their mixing angles. No superpartner has been presently observed, but this fact cannot be used to exclude the hypothesis because it can be explained by tuning the free parameters. We can always imagine that our particle accelerators have not the energy required to produce the LSP, simply because we cannot predict its mass.

The last particle candidate comes from extra-dimensional theories. In 1921 T. Kaluza proposed the idea of to unify the electromagnetism with gravity by introducing a space-time with more than four dimensions, in which the metric tensor includes the gauge fields. In this new picture, the 4-dimensional everyday space-time becomes a structure called brane, enclosed in a $(3+\delta+1)$-dimensional space-time that is named bulk. According to these models, we cannot perceive the extra dimensions because they are compactified on circles of some radius R. This condition leads to the constraint that all the fields propagating in the bulk must have a quantized momentum such that $p^2 \propto 1/R^2$. The result is that a set of Fourier modes emerges for every field in the bulk, these modes are called Kaluza-Klein (KK) states. In the 4-dimensional space-time, the KK states assume the form of physical particles with masses $m_n \propto n/R$, where n is the mode number. In particular the Lightest Kaluza-Klein Particle (LKP) is a possible Dark Matter particle and a calculation from G. Servant and T. Tait [58] tried to predict its mass considering the constraints set by the observed amount of DM. Such calculation suggests a mass in the range between 400 and 1200 GeV.

1.2.3 Weakly Interactive Massive Particles

Even if we don't know which particle represents the DM, we can summarize its expected properties into a generic model called Weakly Interactive Massive Particle (WIMP) and denoted with χ. The name itself highlights the two most relevant characteristics: WIMP must be massive and it must have a

cross section of approximately weak strength, and be therefore neutral. Its mass is expected to fall in the range between 10 GeV and few TeV.

As we will see in the next chapter, a sensible information, from the experimental point of view, is the WIMP velocity distribution in the halo. The average speed can be estimated by using the virial theorem. The mass of the halo is almost fixed by the stellar kinematics: for example, in the Milky Way it is reasonable to assume a mass of $M_{halo} \sim 10^{12} M_{\odot}$ where $M_{\odot} = 2.99 \cdot 10^{30} kg$ is the solar mass unit. This, assuming a local density of $\rho \simeq \ 0.3\ GeV/cm^3$ [1], gives a halo radius of the order of $R_{halo} \sim 100\ kpc$ and thus

$$\langle v \rangle \sim \sqrt{\frac{GM_{halo}}{R_{halo}}} \sim 200 km/s \tag{1.21}$$

A more precise model can be made by assuming that, in the early Universe, the WIMPs were in thermal and chemical equilibrium with SM particle gas after the inflation. This condition can be satisfied when $T \gg m_{\chi}$ where T is the average temperature of the Universe. In this regime WIMPs were continuously produced and destroyed by the annihilation into particle-antiparticle pairs, resulting in a number density proportional to $m_{\chi} \propto T^3$. When the Universe temperature decreased down to $T \sim m_{\chi}$ the equilibrium was broken because SM particles were no more able to replace the annihilated DM pairs; this caused the WIMP numerical density n_{χ} to exponentially decrease as $n_{\chi} \propto e^{-m_{\chi}/T}$. The density was finally fixed when the annihilation rate $\Gamma_{annihilation}$, given by DM particles density times their annihilation cross section and the relative average speed, became smaller than the Hubble constant:

$$\Gamma_{annihilation} = n_{\chi} \langle \sigma v \rangle \lesssim H \tag{1.22}$$

After this moment, called freeze-out, DM is no longer in chemical equilibrium, but it remains in thermal equilibrium with the surrounding plasma of SM particles thanks to elastic interactions. Following the evolution of the inelastic scattering process with time, by using the Boltzmann equation, it is possible to obtain an estimation of DM density today

$$\Omega_{\chi} h^2 \simeq const. \cdot \frac{T_0^3}{M_{Pl}^3 \langle \sigma_A v \rangle} \simeq \frac{0.1\ pb \cdot c}{\langle \sigma_A v \rangle} \tag{1.23}$$

where T_0 is the current CMB temperature, M_{Pl} is the Planck mass, c is the speed of light, σ_A is the annihilation DM cross section, v is the relative speed of WIMPs and $\langle ... \rangle$ indicates the operation of averaging over the thermal

[1] This value, even if it is different from the one reported in formula 1.18, represents a standard value adopted in many analysis.

velocity distribution. Note that the value 0.1 *pb* falls into the typical range of weak interaction cross sections; this correspondence between the weak interaction and the observed relic density is known as the "WIMP miracle" and is considered one of the strongest indication in support of the WIMP model.

Chapter 2

Dark Matter detection

From now on, for the reasons explained in the previous chapter, we will focus our attention on WIMP particles. In this chapter the main experimental methodologies for the investigation on the WIMP model will be presented, with a more detailed explanation of the *annual modulation* signature. Finally an overview on the experimental status, regarding the direct detection, will be given.

2.1 Experimental techniques

According to astrophysical observations, the most convincing hypothesis is that the Dark Matter problem is solved by the presence of a galactic halo made of, at least partially, an unknown particle with mass between few GeV and few TeV. To confirm this hypothesis, the observation of the WIMP particle, and the study of its properties, is fundamental.

The three main experimental approaches are schematically represented in figure 2.1. The figure, that shows the interaction between four particles, can be read in three ways. The first is from left to right: in this case two WIMPs annihilate to produce a SM pair. This approach is called *indirect detection* and is followed by several probes and ground telescopes that look for p-$\overline{p}$, e^+-e^-, ν's or γ's anomalies in cosmic radiation. The second is from right to left: in this case we have the production of a χ-$\overline{\chi}$ pair through the annihilation of two Standard Model particles. This approach is followed by the particle colliders. The last is from top to bottom: in this case we have the scattering between χ and a SM particle. This approach, called *direct detection*, is used in this work and is the one followed by the underground, low-background, counting experiments.

The χ production through accelerators is mainly sought at Large Hadron Collider (LHC) at CERN for obvious reasons of energetic limits. In general

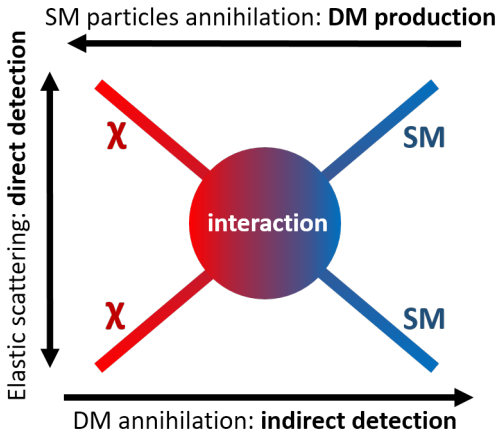

Figure 2.1: *The three detection experimental approaches. If the time evolution is read from left to right we have the annihilation of two DM particles and the production of two SM particles (indirect detection), from right to left we have the annihilation of two SM particles and the production of two DM particle (DM production with accelerators) and finally from top to bottom we have the elastic scattering (direct detection).*

we can say that it is possible to investigate for new physics by looking for particles with mass smaller than half of the energy evaluated in the laboratory reference frame. The LHC, with a center of mass energy of ∼14 TeV, is currently the most promising facility. In particular the two large general-purpose experiments ATLAS and CMS have been designed to be sensitive to the broadest possible range of signatures of new physics. In practice, since DM is expected to be electrically neutral and cosmologically stable and, especially, weakly interacting, its typical signature in colliders is missing energy. A set of supersymmetric models have been tested by these two experiments especially for R-parity conserving supersymmetry, because such models contain the stable LSP. Dark Matter production will be not discussed here, a detailed review on this argument, as well as for the other explained techniques, can be found in [57].

2.1.1 Indirect detection

Indirect detection technique is based on the assumption that WIMPs, present in the galactic halo, can annihilate or decay into Standard Model particles that can be detected. It must be noticed that this technique is somehow complementary to the DM production because it is able to scan higher energies. For example the Fermi Large Area Telescope (Fermi-LAT), which is a high-energy gamma probe launched into a near-Earth orbit in 2008 with an

upper energy threshold of 500 GeV, can be sensitive to $m_\chi \lesssim 2TeV$. Similarly the High Energy Stereoscopic System (H.E.S.S.), a very high energy gamma telescopes array in Namibia, is sensitive to masses of the order of 20 TeV [59] (for comparison, the energy in the laboratory reference frame of LHC is $\sim 14\ TeV$).

Since DM can be slowed down or trapped by gravitation by massive bodies, a greater χ density is expected in regions such as Sun, Earth or the galaxy center. Following this idea, the enhancement of the density leads to higher annihilation rate and to bigger flux of the produced particles. For this reason DM density profile is an important input in such kind of analysis; the distribution obtained by simulations are well approximated by a two parameter function, called Navarro-Frenk-White profile [60]:

$$\rho_{NFW}(r) = \frac{\rho_0}{\left(\frac{r}{r_s}\right)\left[1+\left(\frac{r}{r_s}\right)\right]^2} \tag{2.1}$$

where r is the distance from the center of the galaxy, r_s is a scale radius and ρ_0 is a normalization constant. More recent simulations suggest that, especially in the innermost region of the halo, the profile should be described by the Einasto function [61]:

$$\rho_E(r) = \rho_0\ exp\left\{ -\frac{2}{a}\left[\left(\frac{r}{r_s}\right)^a - 1\right]\right\} \tag{2.2}$$

where the same notation of equation 2.1 has been used, and $a = 0.17$ is a dimensionless effective value.

Even if almost all particles can be annihilation products, two of them are considered "golden channels". The first one is represented by GeV neutrinos coming from Sun or Earth center. For example muon neutrinos can pass through the Sun, where they are produced, interact with the Earth matter, and produce high energy muons that can be detected by neutrino telescopes such as SuperKamiokande, IceCube or ANTARES - or MACRO and AMANDA in the past. Up to now, only the limits from the measurement of solar neutrino flux evaluated by IceCube [62], AMANDA [63] and SuperKamiokande [64] result competitive with direct WIMP search limits.

The second promising probe is represented by monoenergetic γ's from space. Nowadays, we have two excesses in the gamma-ray band which could be attributed to dark matter annihilation, one from the center of our galaxy and one from the dwarf galaxy Reticulum II [65]. They can be explained by the same dark matter particle with mass $m_\chi \sim 30\ GeV$. At the same time, results from Fermi-LAT collaboration still exclude most of the region, in the

annihilation cross-section vs. mass plane that can accommodate the excesses [66].

2.1.2 Direct detection

Assuming a density of 0.3 GeV/cm^3, a value commonly adopted in DM analysis, the WIMP flux on the Earth is of the order of $10^5(GeV/m_\chi)cm^{-2}s^{-1}$. Even if the DM particles interact with weak-scale cross-sections, this flux is large enough to produce a detectable signal in a large detector. Direct search is based on the detection of such DM particles that pass through a detector and interact with it. Specifically, direct search aims to measure the event rate and the energy deposited by DM particles on target nuclei. Moreover, some R&D projects aim to reconstruct the direction of the incoming WIMP. Because of the small cross-section, DM represents a tiny contribution to the expected events; for this reason all the experiments based on this technique are characterized by the usage of ultrapure materials, active or passive shielding - also placing the detector in underground laboratories - and are often able to perform particle discrimination. This technique is sensitive to some parameters, such as the local DM density and its velocity distribution, that require some external input from astrophysics. However, for a given halo model it is relatively easy to derive the experimental signatures. In the next sections it will shown how to evaluate the event rate, the energy distribution of events and their time dependence. This information will be used in the analysis presented in this work.

2.2 Direct detection signature

In order to ensure the feasibility, and to evaluate the sensitivity of a direct detection experiment, the event rate must be estimated because, when compared to the expected background, it gives an indication of the signal-to-noise ratio. To be more general, we introduce the differential event rate: it is defined as the number of WIMP events per unit of time and detector sensitive mass. It is given by:

$$\frac{dR}{dE_R} = \frac{\rho_0}{m_N m_\chi} \int_{v_{min}}^{\infty} v f(v) \frac{d\sigma_{\chi N}}{dE_R}(v, E_R) dv \tag{2.3}$$

where ρ_0 is the local WIMP density (an example of input required from astrophysical measurements), $d\sigma_{\chi N}/dE_R(v, E_R)$ is the differential cross-section for the WIMP–nucleus scattering and $f(v)$ is the WIMP speed distribution, normalized to 1 and expressed in the detector frame. The integral starts from v_{min} which is the minimum velocity that produces a recoil of energy

E_R. The WIMP-nucleon scattering is assumed elastic and, given that, according to the halo model, the relative speed is of order of 100 km/s, it occurs in the non-relativistic limit. Being a classical calculation, the recoil energy is easily expressed as a function of the scattering angle θ^* in the center of mass reference frame:

$$E_R = \frac{\mu_N^2 v^2 (1 - \cos\theta^*)}{m_N} \tag{2.4}$$

where $\mu_N = m_\chi m_N/(m_\chi + m_N)$ is the WIMP–nucleus reduced mass. The integral bound v_{min} in 2.3 represents the minimum velocity able to cause an energy deposition of E_R. The maximum deposited energy, for a fixed velocity, is obtained for $\theta^* = \pi$, so we can evaluate the lower bound as

$$v_{min} = \sqrt{\frac{m_N E_R}{2\mu_N^2}} \tag{2.5}$$

The upper bound of the integral is, in principle, infinite but the WIMP velocity distribution $f(v)$ introduces a limit which is the local escape speed from the Milky Way. The total event rate, per unit of mass and time, is obtained by integrating the differential rate over the energies that can be detected, and thus starting from the detector energy threshold E_T:

$$R = \int_{E_T}^{\infty} \frac{dR}{dE_R} dE_R \tag{2.6}$$

The particle physics describing the interaction is included in the WIMP-nucleon cross-section factor and its precise calculation requires the knowledge of the interaction mechanism between the DM candidate with quarks and gluons, as well as a precise description of the recoil nucleons in terms of its elementary components. While the second part can be described with approximate models with large uncertainties, the first one requires strong assumption on the DM candidate. In this context, a more general description can be given. The cross-section can be separated in two contributions: the spin-independent one, which comes from scalar and vector couplings to the quarks and does not depend on the nucleus spin, and the spin-dependent one which comes from the axial-vector couplings. The differential cross-section can be thus expressed by the sum of two contributions:

$$\frac{d\sigma_{\chi N}}{dE_R} = \left(\frac{d\sigma_{\chi N}}{dE_R}\right)_{SI} + \left(\frac{d\sigma_{\chi N}}{dE_R}\right)_{SD} \tag{2.7}$$

The weights of the two components are given by the nucleus wavefunctions, and thus depend on the composition of the detector sensitive mass.

2.2.1 Spin-dependent contribution

The spin-dependent (SD) contribution to WIMP-nucleus cross-section arises from the WIMP axial coupling to the quarks of the nucleon. Independently from the WIMP being a fermion (both Dirac and Majorana) or a spin-1 boson (such as the LKP candidate), the interaction is proportional to the factor $\overline{q}\gamma_\mu\gamma_5 q$ where γ_μ and γ_5 are the Dirac matrices combined to describe the pseudo-vector behavior. In both cases, for a nucleus of N nucleons, the matrix element can be written as:

$$\langle N \mid \overline{q}\gamma_\mu\gamma_5 q \mid N\rangle = 2\lambda_q^N \langle N \mid J_N \mid N\rangle \tag{2.8}$$

where λ_q^N are the coefficients that relate the quark spin matrix elements (left side of the equation) to the total angular momentum of the nucleons J_N. Such coefficients can be parameterized as

$$\lambda_q^N \simeq \frac{\Delta_q^{(p)}\langle S_p\rangle + \Delta_q^{(n)}\langle S_n\rangle}{J} \tag{2.9}$$

where J indicates the total nucleus angular momentum and $\Delta_q^{n,p}$ contains the matrix element of the axial-vector current for neutrons (n) or protons (p). In this analysis the factors $\langle S_{n,p}\rangle$ cover an important role. They are, indeed, the expectation values of the spin due to the nucleon N content $\langle S_{n,p}\rangle = \langle N|S_{p,n}|N\rangle$ and can be easily calculated according to effective nuclear models.

In particular we know that nucleons of the same type tend to stay in singlet pairs, so that their total spin is almost zero. This has the effect that the nucleus spin is mainly given by the unpaired nucleons, the effect is that in a even-even nucleus (in which there are not unpaired nucleons) the spin-dependent cross-section vanishes. Fortunately most of the nuclei that compose CUORE-0 detectors (^{16}O, ^{18}O, ^{130}Te, ^{128}Te, ^{126}Te) are even-even nuclei, and σ^{SD} contribution can be reasonably neglected. For this reason, in this analysis, the dominant contribution to the cross-section comes from the spin-independent interaction.

The most relevant fraction of non even-even nuclei is represented by ^{125}Te, whose isotopic abundance in natural Tellurium is about 7%.

2.2.2 Spin-independent contribution

The spin-independent (SI) contribution comes from the scalar-scalar $\alpha_q^S\overline{\chi}\chi\overline{q}q$ and the vector-vector $\alpha_q^V\overline{\chi}\gamma_\mu\chi\overline{q}\gamma^\mu q$ couplings and, as usual, depends on the particle physics underlying the WIMP candidate. In general the SI differen-

tial rate can be written as a function of the nuclear form factor $F(E_R)$

$$\left(\frac{d\sigma_{\chi N}}{dE_R}\right)_{SI} = \frac{m_N \sigma_0^{SI} F^2(E_R)}{2\mu_N^2 v^2} \tag{2.10}$$

$F(E_R)$ qualitatively describes the Fourier transform of the nuclear density, and is usually expressed as a function of the momentum transfer q. By definition $F(0) = 1$ so that σ_0 is the cross-section at zero momentum transfer.

The contribution of the scalar coupling to the cross-section can be expressed as:

$$\sigma_0^{SI,S} = \frac{4\mu_N^2}{\pi}[Zf^p + (A-Z)f^n]^2 \tag{2.11}$$

where Z and A are the atomic and the mass number of the nucleus. f^p and f^n are effective coupling constant so defined:

$$f^i = m_i \left(\sum_{q=u,d,s} \frac{\alpha_q^S}{m_q} f_{Tq}^i + \frac{2}{27} f_{TG}^i \sum_{q=c,b,t} \frac{\alpha_q^S}{m_q} \right) , \qquad i = n, p \tag{2.12}$$

where m_q are the quark masses, f_{Tq}^i and f_{TG}^i are the fraction of the nucleon mass due to the quarks and the gluons respectively, with the constrain:

$$f_{TG}^i + \sum_{q=u,d,s} f_{Tq}^i = 1$$

The contribution of the vector coupling, that fortunately is due to the valence quarks only, can be expressed as a function of the number of *up* and *down* quarks, $(A+Z)$ and $(2A-Z)$ respectively.

$$\sigma_0^{SI,V} = \frac{\mu_N}{64\pi} \left(\alpha_u^V (A+Z) + \alpha_d^V (2A-Z)\right)^2 \tag{2.13}$$

In conclusion, for a general WIMP model, that considers both scalar and vector interactions, the SI component of the scattering cross-section is:

$$\left(\frac{d\sigma_{\chi N}}{dE_R}\right)_{SI} = \frac{2m_N}{\pi v^2} \left[[Zf^p + (A-Z)f^n]^2 + \frac{[\alpha_u^V (A+Z) + \alpha_d^V (2A-Z)]^2}{256} \right] F^2(E_R) \tag{2.14}$$

For most WIMP models the coupling to neutrons and protons is very similar, that means $f^p \approx f^n$, so the scalar contribution can be approximated as:

$$\left(\frac{d\sigma_{\chi N}}{dE_R}\right)_{SI} = \frac{2m_N A^2 (f^p)^2}{\pi v^2} F^2(E_R) \tag{2.15}$$

The SI contribution is thus proportional to A^2, while the SD contribution is a function of the angular momentum $(J+1)/J$. This leads to the conclusion

that, for heavy nuclei ($A \geq 20$), even for the WIMP models that include both SI and SD interactions, the spin-dependent component of the cross-section is negligible [67]. For this reason the approximation of spin-independent interaction can be applied to ^{125}Te also.

In this this work only the spin-independent cross-section will be considered.

2.2.3 Dark Matter distribution and flux

Equation 2.3 shows that the velocity distribution $f(v)$ of WIMPs is required to evaluate the event rate because it weights the WIMP cross-section expressed as a function of the relative velocity. This distribution depends on the adopted halo model. Despite the fact that the observations can be explained by several models, a specific one is conventionally used to compare different experiments. In this case DM velocity is isotropic and follows the Maxwellian distribution, i.e. its module follows the Gauss distribution:

$$f(v) = \frac{1}{\sqrt{2\pi}\sigma} exp\left(-\frac{|\ v\ |^2}{2\sigma^2}\right) \tag{2.16}$$

The two requirements (isotropic and Maxwellian distributed velocities) directly lead to a halo density profile $\rho(r) \propto 1/r^2$. In should be noted however that astrophysical observations and numerical simulations show that the halo has, more likely, a different density profile and is not isotropic. On the other hand, up to now, observations and simulations do not indicate a precise model, especially in the central region of the galaxy where we have the biggest uncertainties. We know that the standard halo model represents a simplification, but it is a convincing first approximation and it is universally used as a reference point for the interpretation and the comparison of experimental data. This work doesn't make an exception and the standard halo model will be used.

Looking at this model more in detail we see that the velocity dispersion σ in formula 2.16 is related to the average velocity of WIMP particles: $\sigma = \sqrt{3/2}v_c$ where v_c is the local circular speed i.e. the speed the Solar System rotates around the galaxy center. In the conventional model is $v_c = 220$ km/s and this value is supported by a calculation, obtained from the combination of independent measurements, performed in 1986 by F. J. Kerr and D. Lynden-Bell [68], that gave $v_c = (222 \pm 20)$ km/s. A more recent observation [69] pointed out a consistent value of $v_c = (218 \pm 7)$ km/s. For the conventional value $v_c = 220$ km/s we obtain $\sigma \simeq 270$ km/s. The last ingredient we need is the galaxy escape speed. The halo distribution $\rho_0 \propto 1/r^2$ has an infinite radius, however, if we assume a steady state, it is unreasonable to include

WIMP particles with a velocity bigger that the galaxy escape speed v_{esc}, i.e. the speed such that the particle is no more gravitationally bounded. In the standard halo model the reference value is $v_{esc} = 650$ km/s.

2.2.4 Nuclear recoil spectrum

From the knowledge of the differential rate (equation 2.3), of the cross-section (equation 2.15) and the WIMP velocity distribution (equation 2.16), we can find the expression for the expected nuclear recoil spectrum. Considering only the spin-independent component of the WIMP-nucleus cross-section we obtain:

$$\frac{dR}{dE_R} = \frac{\rho_0}{m_N m_\chi} \int_{v_{min}}^{v_{esc}} v \frac{1}{\sqrt{2\pi}\sigma} exp\left(-\frac{|\ v\ |^2}{2\sigma^2}\right) \frac{2m_N A^2 (f^p)^2}{\pi v^2} F^2(E_R) dv \quad (2.17)$$

In [70] an approximated expression can be found:

$$\frac{dR}{dE_R} \approx \left(\frac{dR}{dE_R}\right)_0 F^2(E_R) exp\left(-\frac{E_R}{E_C}\right) \quad (2.18)$$

where the constant factor $(dR/dE_R)_0$ is simply the maximum rate, obtained at $E_R \to 0$ and E_C is a characteristic energy given by

$$E_c \approx \frac{2\mu_N^2 v_c^2}{m_N} \quad (2.19)$$

The first thing that we notice is that the spectrum has an exponential decaying shape, that implies that, for DM detection it is fundamental to reach an energy threshold as low as possible. From this point of view the bolometric technique, that will be explained in the next chapter, offers notable advantages, especially when associated with a low energy trigger algorithm, such as the Optimum Trigger described in section 4.1. Another consideration is that, looking at the dependency of the spectrum from the target nuclei, we can identify two regimes. For heavy target nuclei (or light WIMP) $m_\chi \ll m_N$ we have $\mu \simeq m_\chi$ and thus $E_c \propto m_\chi^2/m_N$ while for light target nuclei (or heavy WIMP) it is $E_c \propto m_N$. Aside from this, it must be considered that, since the DM mass density is fixed by cosmological observations, the event rate, which is directly proportional to χ numerical density, is inversely proportional to the χ mass. The expected spectra, for some target nuclei, are shown in figure 2.2.

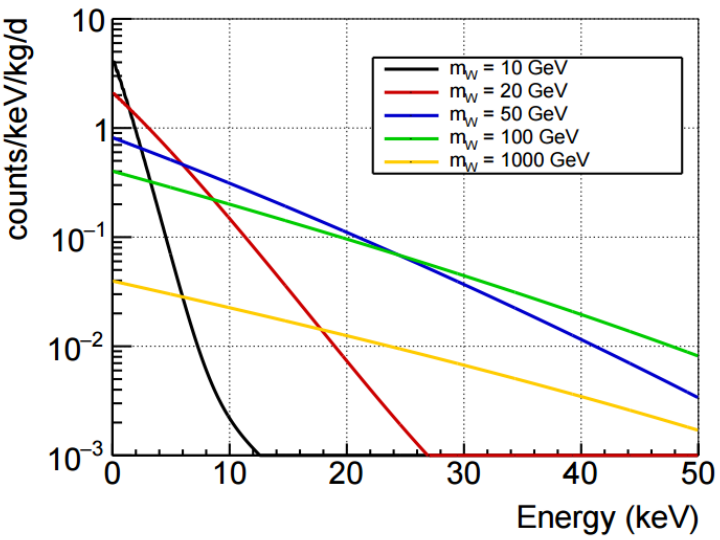

Figure 2.2: *Expected DM event rate in a TeO_2 bolometer for different WIMP masses. Only SI interaction was considered with $\sigma_{\chi N} = 10^{-46} cm^2$ and Standard Halo Model parameters. Picture from [7].*

2.3 Annual modulation

Unfortunately the low energy threshold is not the unique required feature for a DM experiment. Figure 2.2, which is based on the not-so-conservative assumption of a WIMP-nucleon cross-section $\sigma_{\chi N} = 10^{-45}$ cm^2, shows rates of the order of 10^{-5} $cdp/kg/keV$ in the ∼10 keV region. This value is well below the more optimistic background that an experiment can reach without an event rejection strategy; to have a comparison, CUORE-0, which is considered an ultra-low background detector, shows at that energy a background rate of several cpd/keV/kg. For this reason the experiments aiming to a direct DM detection, take advantage of particle identification techniques that offer the opportunity, for example, to discriminate an electron recoil (ER) (mostly due to γ's or β's events) from a nuclear recoil (NR) (due to α's, neutrons and "maybe" WIMPs). A recoiling electron follows a path which is longer, for a given recoil energy, with respect to the one followed by a recoiling nucleus. As consequence, the signal induced by an ER may differ from the one induced by a NR. It is possible to divide the detection signals in three main channels: scintillation, ionization, and heating (or, more precisely, phonon collection). Many experiments have the capability to detect two different signals at the same time (this capability is called *dual channel* detection). By measuring the two energies (from two distinct channels), deposited by the same particle event, it is possible to reject the ER from the

DM search. α particles, which typically come from the material surrounding the sensitive mass[1], can indeed be excluded by introducing a fiducial volume.

Other experiments can obtain a similar background reduction even acquiring a single signal and performing the so-called Pulse Shape Discrimination (PSD). In these cases the mechanism that produces the physical signal slightly depends on the incoming particle so that it is possible to identify the particle by looking at the pulse characteristics. An example is represented by liquid Argon in which the scintillation is given by the combination of two different excitations, with different decay times, and the ratio of the two is radiation-dependent.

CUORE, as well as CUORE-0, has not been designed to provide dual channel detection. Furthermore the shape of the heat signal produced by its crystals is almost independent from the kind of incident particle so no PSD analysis is feasible. Fortunately the WIMP signal is expected to present a signature that can be identified over the background: the annual modulation. In section 2.2.3 the average WIMP velocity has been assumed constant and equal to the local velocity $v_c = 220$ km/s, which is an approximation of the speed of Sun $v_\odot$ in the galaxy rest frame. When we move to Earth we have to consider the velocity of the Earth with respect to the Sun. Earth orbits around the Sun with velocity $v_\oplus = 30$ km/s, on a plane with an inclination of $\theta = 60°$ with respect to the galactic plane. The Earth velocity, in the galaxy rest frame (and thus in the DM halo rest frame) becomes

$$v_E(t) = v_\odot + v_\oplus \cos\theta \cos[\omega(t - t_0)] \simeq v_c + v_\oplus \cos\theta \cos[\omega(t - t_0)] \quad (2.20)$$

where $\omega = 2\pi/year$, and t_0 corresponds to the 2^{nd} June (see figure 2.3).

The speed variation causes a flux variation, and thus an event rate variation, over the year. To evaluate the rate variation, being $v_\oplus \cos\theta \ll v_\odot$, a first-order Taylor approximation can be used:

$$\frac{dR}{dE}(v_E(t)) = \frac{dR}{dE}(v_c) + \frac{d}{dv}\left(\frac{dR}{dE}\right)_{v=v_c} v_\oplus \cos\theta \cos[\omega(t - t_0)] \quad (2.21)$$

This means that the number of events detected in a certain energy range (the i-th energy interval) has a time dependence $S_i(t) = S_{0i} + S_{mi} \cos[\omega(t - t_0)]$ in which S_{0i} is the average value (when $\cos[\omega(t - t_0)] = 0$) and S_{mi} is the modulation amplitude which depends on the energy. The expected modulation amplitudes are visible in figure 2.4. Note that, for some values of m_χ and E, the modulation amplitude can be negative.

The annual modulation is a powerful signature because it presents three

[1] Unless the α-contaminant is inside the detector bulk.

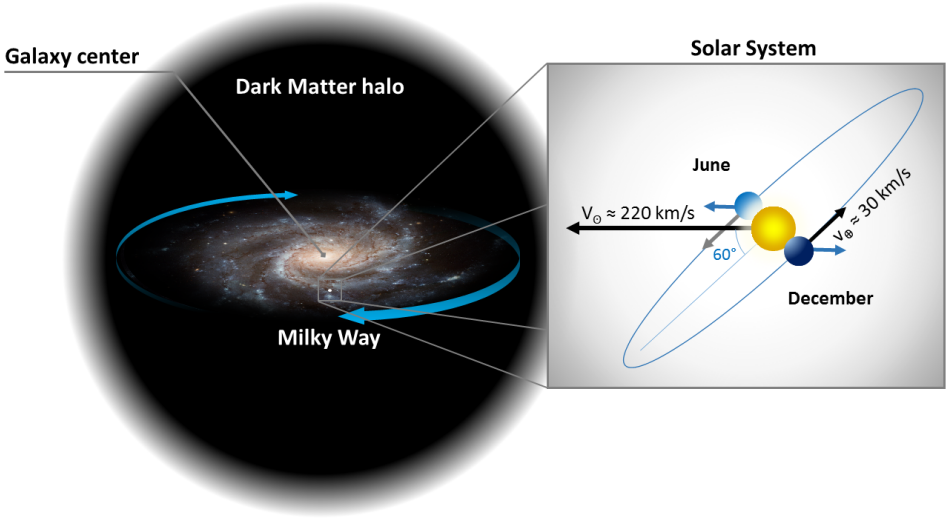

Figure 2.3: *The average velocity of the "WIMP wind" is given by the velocity of Earth in the galaxy rest frame. Such velocity is obtained as the sum of the velocity of Sun in the galaxy frame and the revolution speed of Earth. In this calculation the angle between the galactic plane and the Earth orbit plane must be taken into account.*

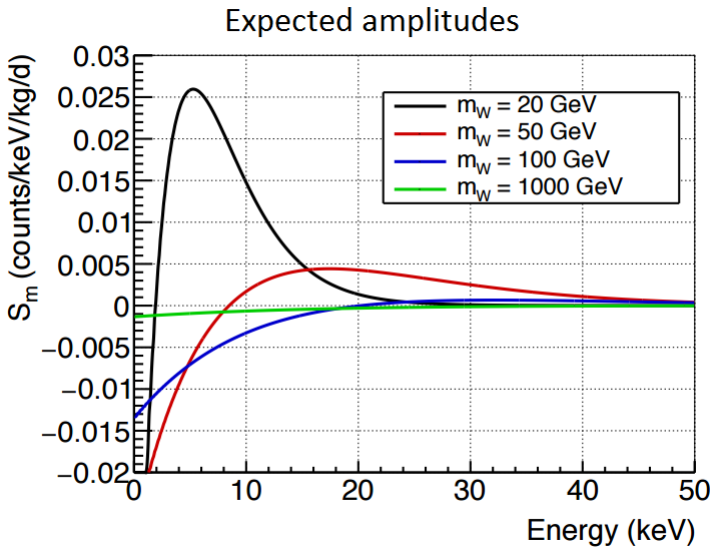

Figure 2.4: *Expected modulation amplitude for different values of m_χ and assuming a TeO_2 detector. The following values have been used in the simulation: DM local density $\rho_0 = 0.3\ GeV/cm^3$, galaxy escape speed $v_{esc} = 650\ km/s$, average speed $v_c = 220\ km/s$, amplitude of the velocity modulation $v_m = 15\ km/s$ and WIMP-nucleon cross-section $\sigma_{\chi N} = 10^{-5} pb$.*

features at the same time: (i) the event rate follows a sinusoidal profile over the year, (ii) the phase must be compatible with $t_0 = 2^{th}$ June and (iii) the modulation amplitude is visible only in the low energy region of the spectrum. This implies that annual modulation signature (i) is detectable even in presence of a background, unless the background introduces a modulation itself, or its statistic fluctuations overtake the signal amplitude. The phase constraint (ii) permits to reject other phenomena with annual periodicity, such as the muon flux. Finally, thanks to the energy dependency (iii) it is possible to perform a fit over the entire low energy spectrum for specific value of m_χ.

Similarly the capacity to reconstruct the direction of the nuclear recoil would be a powerful tool to look for the daily forward/backward asymmetry associated to the rotation of the Earth. Reconstruction of the recoil momentum could be obtained by using gaseous or anisotropic response detectors and represents the goal of several R&D projects [71][72][73].

2.4 Experiments and Status

In the last decades DM search experienced a strong effort on all the three experimental approaches (direct and indirect detection and DM production with particle accelerators). In this context, however, we will focus on direct detection results obtained by looking at the annual modulation signature. It is important to stress that the comparison of results from different experiments depends on the adopted WIMP-nucleon interaction model because, in principle, we don't know how the cross-section depends on the target material. The easiest way to do that is to assume, as explained in section 2.2, that the interaction is spin-independent and cannot distinguish between neutrons and protons (isospin-invariant). In this case a direct comparison can be made simply normalizing the cross-section by the square of the mass number of the target nucleus. This approach is typically adopted when comparing different experiments in an exclusion plot (as in figure 2.6), but we should not forget that apparently contrasting results can be explained within a different, more complex, interaction model.

A more direct comparison is possible between experiments that use the same detection technology, such as germanium detectors. CoGeNT (Coherent Germanium Neutrino Technology) [74] is one of the experiments that gave a weak indication of modulation. It is placed at the Soudan Underground Laboratory and uses a 440 g high-purity point-contact germanium crystal (pPCGe) operated at the temperature of liquid nitrogen. A positive point-contact diode is a germanium crystal, of cylindrical shape, in which the

positive contact is placed in the center of one of the base of the crystal, while the negative contact is distributed on the opposite base as well as the lateral surface. The advantage of this kind of detectors is that they can reach the very low energy threshold of ∼0.5 keV. CoGeNT collaboration produced a dataset of 1129 live-days, from December 2009 to April 2014. As stated in [75], where an independent analysis of those data is described, DM signal hypothesis must be preferred over the background-only hypothesis; nevertheless its statistical significance is less that 1σ.

The same detector, in this case a crystal of 994 g, is used by the CDEX (China Dark Matter Experiment) [76] collaboration, in Sichuan. In this case the first analysis, with the limited exposure of 53.9 kg·days, did not produce any positive signal for a WIMP mass in the region 6-20 GeV.

A key role is covered by the most discussed experiment DAMA/LIBRA [77] which has produced an uncorroborated claim of DM discovery. Placed at the Gran Sasso National Laboratory, it is composed by 25 high-purity NaI(Tl) scintillating crystals of 9.7 kg mass each. Since the detectors are calibrated with γ-sources - which induce electron recoils -, results are given in terms of "electron equivalent energies" (keVee). For NaI detectors the quenching factor between nuclear and electron recoil is ∼1/4 so the interval 2-6 keVee roughly corresponds to a real deposited energy, on the nuclei, of 8-24 keV. With an exposure of 1.04 tonne·years, accumulated over a period of seven years, DAMA collaboration extracts a modulation signal at 7.5 σ C.L. that, considering the former experiment DAMA/NaI with a total exposure of 1.33 tonne·years over a period of 14 years, becomes 9.3 σ significant (figure 2.5).

In their analysis only single-hit events are considered (because the probability that a WIMP hits more than one single crystal is practically zero) with energy within the interval 2-6 keVee. DAMA data could be explained within the standard halo model in two ways: a WIMP of mass $m_\chi \simeq 50\ GeV$ and $\sigma_{\chi N} \simeq 7 \cdot 10^{-6} pb$ or a WIMP of mass $m_\chi \sim 6 - 10\ GeV$ and $\sigma_{\chi N} \simeq 7 \cdot 10^{-3} pb$. On the other hand, the analysis adopted to obtain those results presents some inconsistencies (discussed in [31]). The first regards the background induced by β's and γ's: it seems to have the uncommon feature to decrease near the detector energy threshold, while it is expected to increase at low energies (for example this happens in the case of electronic noise). The second is that the modulation amplitude decreases over time. If we look at the three independent datasets from original DAMA (1995 to 2001), DAMA/LIBRA phase I (2003 to 2007) and DAMA/LIBRA phase II (2007 to 2009) we obtain three different (and not compatible) values of the amplitude: respectively 20.0±3.2, 10.7 ± 1.9 and 8.5 ± 2.2 (in units of $10^{-3} cpd/kg/keVee$). However the fact remains that no alternative convincing explanation has been presented so

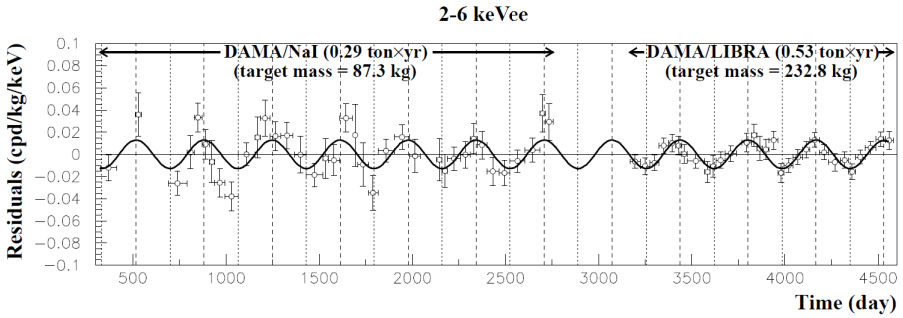

Figure 2.5: *Picture from [8]. Model-independent residual rate of the single-hit scintillation events, measured by the new DAMA/LIBRA experiment in the 2–6 keVee energy intervals as a function of the time. Analogue results from the former DAMA/NaI experiment are also shown for a total exposure of 0.82 tonne·years. Vertical bars represent the error on the estimation of the rate, horizontal bars represent the time bin width. The superimposed curve represents the ideal, according to the standard halo model, cosinusoidal functions with period $T = 1$ yr, phase $t_0 = 152.5$ day and the amplitude obtained by the fit over the whole data.*

far. For example in reference [78] DAMA collaboration shows that even an ad hoc combination of modulating background sources (neutrons, neutrinos and muons) could not explain the observed modulation.

The debate on DAMA results leads, in the last years, to the rise of a lot of new DAMA-like projects, some of which are expected to reach DAMA sensitivity in the next years. One of these projects, SABRE [79], plans to produce two almost identical experiments. The first detector will be placed at Gran Sasso National Laboratories like DAMA, the second one in the south hemisphere (in a gold mine in Australia); in this way it will be possible to test if the modulation signal is due to seasonal effects (in this case a phase shift should be seen).

In any case, the DAMA result is excluded by experiments which use different target materials. Indeed, results from Germanium and Xenon detectors exclude both the $m_\chi - \sigma_{\chi n}$ regions highlighted by DAMA even assuming different cross-sections for protons and neutrons (this scenario is called "isospin violating" WIMPs) [80].

In relation to Xenon detectors, the latest results are from XMASS experiment in Kamioka mine, Japan. XMASS detector is a sphere with a radius of 40 cm, filled with liquid Xenon and immersed in a water tank used as veto. The collaboration recently published a paper [81] that reports the analysis with an exposure of 359.2 live days times 832 kg in which no signal has been found. The obtained exclusion upper limit of the WIMP-nucleon

cross-section $4.3 \cdot 10^{-41} cm^2$ at 8 GeV excludes almost all the DAMA/LIBRA allowed region for light WIMP (m_χ between 6 and 16 GeV).

In general Xenon detector demonstrated to provide the better sensitivity for heavy WIMPs (around 100 GeV) because of the Xe high atomic numbers. The best limits from Xe detectors come from XENON and LUX. XENON-100 [82], with a fiducial mass of 34 kg, gave the impressive upper limit of $2 \cdot 10^{-45}\ cm^2$ at $m_\chi = 55\ GeV$ with a 225 days-long run. It was then surpassed by LUX [83], a 370 kg double phase Xenon detector in SURF laboratories (U.S.A.). After a run of 85 days, with 118 kg of fiducial mass, LUX lowered the upper limit to $7.6 \cdot 10^{-46} cm^2$.

As already explained some detectors provide a dual channel readout in order to enhance the background rejection. This is the case of CRESST-II [84] which uses $CaWO_4$ scintillating crystals operated at cryogenic temperature so that, when the energy deposition happens, both photons and phonons can be detected. For a dataset with exposure of 730 kg·days collected with eight detectors, sixty-seven events were found. Background events are ascribed to four sources: leakage from the e/γ-band, leakage from the α-particle band, neutrons and ^{206}Pb recoils from ^{210}Po decay. According to a maximum likelihood analysis, these sources alone cannot justify the data; the discrepancy can be explained by the scattering of light WIMPs (m_χ in the range 10-25 GeV) with a statistical significance bigger than 4σ. In the last years CRESST collaboration improved the energy threshold providing the best upper limit for light WIMP (down to 0.5 GeV) [85]. Interestingly this last analysis seems to partially exclude their positive hint.

A similar approach is adopted by the Cryogenic Dark Matter Search (CDMS) [86] collaboration which uses semiconductor detectors, both Si and Ge, at the temperature of 40 mK. In this case the dual channel readout is composed by phonon and ionization signals. Silicon is a relatively light nucleus so, even if it is a disfavored target because of the A^2 dependency of the WIMP-nucleus cross-section, it results more sensitive for detection of light WIMPs (∼10 GeV) due to the scattering kinematics. In 2013 they reported the final analysis of data from Si detectors for a total exposure of 140.2 kg·days in which three WIMP-candidate events have been found. A similar result can be interpreted as the detection of WIMPs of $m_\chi = 8.6\ GeV$ and $\sigma_{\chi N} = 1.9 \cdot 10^{-41} cm^2$, corresponding to the maximum of the likelihood profile. At the same time a first analysis of SuperCDMS [87], a CDMS upgrade with improved background rejection, provided, with an exposure of 577 kg·days, the upper limit on the SI WIMP-nucleon cross-section of $1.2 \cdot 10^{-42}\ cm^2$ at $m_\chi = 8\ GeV$. Such result, in the low mass region (4 to 15 GeV), excludes positive hints from CoGeNT, CRESST and CMDS itself.

In conclusion the scenario is still confused; for low mass WIMP some favored regions, in the $m_\chi - \sigma_{\chi N}$ parameters space, have been found. Nevertheless, most of them show low statistical significance or have been retracted after detectors or analysis improvements. Only results from DAMA annual modulation analysis have a very high statistical significance (9.3 σ considering both DAMA/LIBRA and the former DAMA/NaI). On the other hand, several experiments, adopting different target material, exclude the DAMA result. This tension could be solved by adopting WIMP models different from the one usually adopted to compare experimental results, but a more direct confirmation of DAMA favored region is still required.

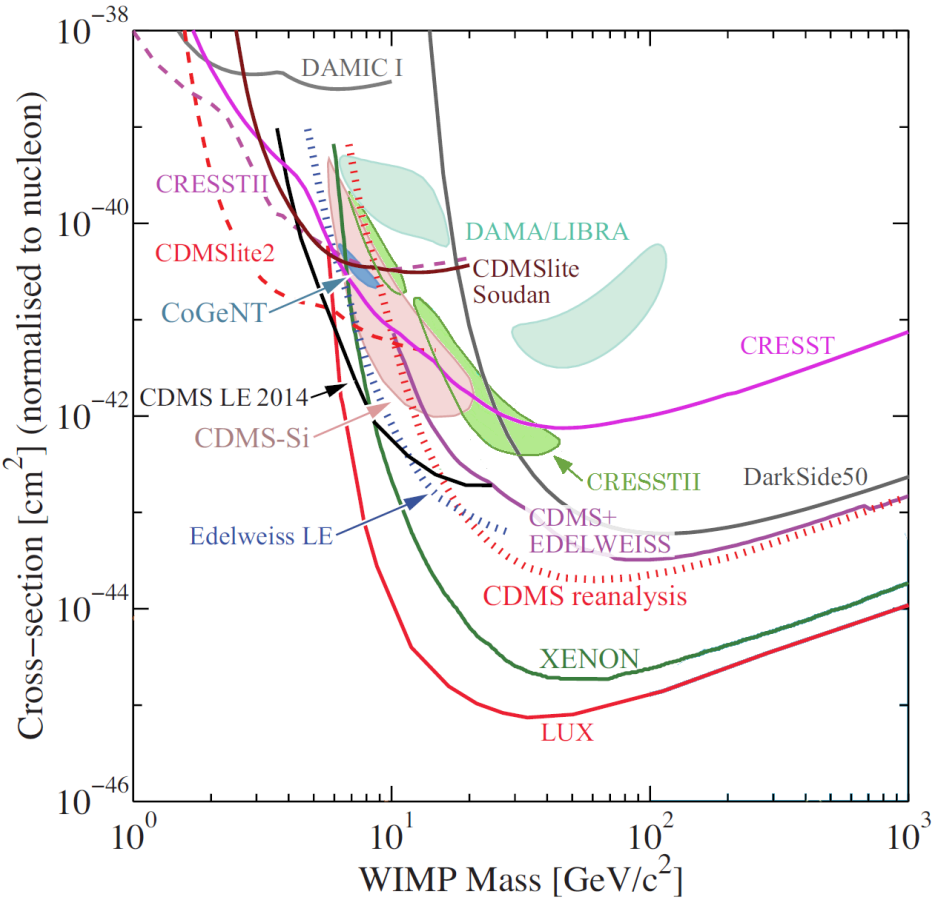

Figure 2.6: *Results from different experiments in terms of spin-independent WIMP-nucleon cross-section, normalized to a single nucleon of target material, for different WIMP masses. DAMA, CoGeNT, CRESST-II and CDMS Silicon data (CDMS-Si) shaded regions show possible WIMP interpretation for positive signals. The solid curves represent upper limits while dotted curves are projected sensitivity. This picture has been taken from [9] where a general review on Dark Matter search can be found.*

Chapter 3

CUORE project

After decades of research and development, in which the collaboration realized several prototypes, the CUORE experiment is finally ready to start data acquisition. In this chapter the CUORE experiment will be described.

CUORE aims to reveal the neutrinoless double decay, if exists, of ^{130}Te. As described in section 1.1.4, th experiment sensitivity depends on several factors such as the number of potential decaying nuclei, the background index, the energy resolution and the experiment live time. CUORE represents an ambitious project that matches these requirements in a challenging way. Particle detection is obtained by using the bolometric technique in which the particle is revealed, and its energy is measured, by monitoring the temperature of the volume in which the energy deposition takes place. Such sensitive volume is represented in CUORE by 988 crystals of TeO_2, each acting as an independent detector. This technique requires that the sensitive mass is maintained at ultra-low temperature, so every crystal-detector is inserted into an uncommonly large dilution cryogen-free cryostat.

In this chapter the working principle of a bolometric detector will be shown, followed by a general description of the CUORE experiment and its subsystems.

The largest part of my PhD work consisted of development and validation of the CUORE Data Acquisition System (DAQ). A description of the DAQ is given in section 3.3. I also gave a contribution to the on-site activities during the cryostat commissioning. The main steps of the cryostat commissioning phase are illustrated in section 3.4. Finally the CUORE-0 experiment is presented in section 3.5.

3.1 CUORE detection technique

The idea of using bolometers to search for rare events was originally proposed by E. Fiorini - a member of the CUORE collaboration - and T. O. Niinikoski in 1984 [88]. This approach, even if it presents technological challenges, ensures a good energy resolution and presents the advantage that the source of the searched decay is embedded in the detector itself. At the same time, this technique has never been adopted on such a large scale experiment: the array of 988 CUORE crystals constitutes a mass of $\simeq$ 740 kg. This is the reason why, before CUORE, the collaboration realized two prototypes. Cuoricino [89] took data from 2003 to 2008, it demonstrated the feasibility of to run an array of 62 TeO_2 crystals as a particle detector and it offered to possibility of to investigate the background sources. Afterwards CUORE-0, which took data from 2013 to 2015, served as test bench for the assembly techniques designed to obtain a background index in the ROI below a prefixed value of 0.01 counts/year/keV/kg.

3.1.1 Bolometric technique

Before proceeding I clarify the use of the word bolometer. In the context of CUORE, the collaboration refers to the detectors as bolometers, while calorimeters would be a more appropriate. Indeed, bolometer is used to denote a device that measures the power of a radiation, thus an energy per unit of time, while a calorimeter is used to measure the energy deposition due to a particle or a particle jet. The confusion probably comes from the fact that CUORE crystals, even if, technically speaking, they are calorimeters, are operated at cryogenic temperature, and this is a typical characteristic of a bolometer.

A bolometric detector is based on three main components. The absorber is the sensitive volume in which the energy deposition takes place, such energy is converted in heat, and increases the absorber temperature. The thermistor is the sensor thermally coupled to the absorber so that it can be used to measure the absorber temperature. Finally a thermal link to a thermal bath restores the original bolometer temperature.

Behind this simple mechanism a complex sequence of processes takes place. The particle which is crossing the absorber - be it a β for double-beta decay, a recoiling nucleus in case of WIMP detection, an electron scattered by a photon, etc... - loses its energy mainly by ionizing the material. Such energy, thanks to the recombination of the electron-hole pairs is converted to phonons which propagate over the absorber. In this phase the produced phonons are called *ballistic* because they evolve like free particles. Because of

scattering with crystal impurities, all the ballistic phonons are then converted into thermal phonons and the thermal equilibrium is then reached. Under the reasonable assumption of neglecting radiative effects, all the energy of the incident particle is converted to phonons, and the temperature variation can be used for the energy measurement.

For a small energy deposition the thermal capacity of the absorber can be considered constant, and the temperature variation is simply $\Delta T = E/C(T)$ where E is the deposited energy and C is the thermal capacity. For a fixed energy deposition, the bigger is the temperature rise the higher is the detector sensitivity, so a small thermal capacity is preferable. The specific heat, as a function of the temperature, is given by two contributions: the first, c_l, is due to the lattice excitation and is proportional to T^3; the second, c_e, is due to the free electrons excitation and is proportional to T.

$$c(T) = c_l(T) + c_e(T) = \frac{12\pi^4 N_A k_B}{5}\left(\frac{T}{\Theta_D}\right)^3 + \frac{Z N_A k_B \pi^2}{\Theta_D}\frac{T}{\Theta_F} \tag{3.1}$$

where N_A and k_B are the Avogadro and the Boltzman constants, Θ_D and Θ_F are the Debay and Fermi temperatures, which depend on the material, Z is the number of conduction electrons per atom. Given that $c_e \propto T$, at low temperatures it is the dominant component but it vanishes when considering an insulator (Z=0 in TeO_2). So, in order to obtain a reasonably small thermal capacity, the absorber must be an insulator, of small mass, operated at low temperature. To give an indication, CUORE crystals have, at $T = 10\ mK$, $C \simeq 2\ nJ/K$ so an energy deposition of 1 MeV produces a temperature rise of $\sim 100\ \mu K$ that can be detected by the thermistor [11].

The thermistor, which is glued on the crystal, goes to the same temperature thanks to the conductance with the absorber. In this context the sensors can be of two types: semiconductors or transition edge sensors (TES). TES are very sensitive but their tight dynamic range makes them disadvantageous in all the application in which a precise control of the temperature cannot be achieved. CUORE is a tonne-scale cryostat with several thermal noise sources so Germanium neutron transmutation doped semiconductors (Ge-NTD) are used. Their logarithmic sensitivity, defined as:

$$\eta = \left|\frac{d\log R(T)}{d\log T}\right| \rightarrow \frac{dR}{R} = \eta\frac{dT}{T} \tag{3.2}$$

is about 10.

NTD are small Germanium doped crystals in which the doping has been obtained through the neutron bombardment of a pure crystal in order to obtain a dopant density as homogeneous as possible. At high temperature,

when the average thermal energy is grater than the energy gap between the valence and the conductance bands of the crystal, the NTD behaves as a conductor. This regime is called *intrinsic* and is independent from the doping. The doping effect is visible at lower temperature when the thermal energy is not sufficient to bring electrons in the conduction band, but the impurities introduce other allowed bands, with smaller energy gaps of the order of 1-10 meV. This mechanism is called *extrinsic* conductivity and can be used to extend the conductive behavior down to few K. Below 1 K the probability of an electron to have enough energy to jump in the conduction band is so small that the conduction is only possible if the electron tunnels from an impurity site to another. The tunnel probability is inversely proportional to the difference of coulombian wall and the electron energy so a phonon can excite an electron and make the tunnel effect more probable. This interaction between the phonon and the tunneling electron is called "hopping" conduction and leads to the following relation between resistance and temperature

$$R(T) = R_0 \exp\left(\frac{T}{T_0}\right)^{\gamma} \tag{3.3}$$

where R_0, T_0 and γ depend on the doping level and have to be experimentally determined. For the CUORE sensors, typical values are $\gamma = 1/2$, $R_0 \simeq 1\Omega$ and $T_0 \simeq 4\ K$, so that the resistance at 10 mK (the working temperature of CUORE bolometers) is of the order of 100 MΩ.

In general the thermistor signal depends on the number of phonons into the absorber. Considering the Poisson statistics, fluctuations on the phonon number leads to the energy resolution $\sigma = \sqrt{k_B C T^2}$. This term, that at 10 mK is of the order of 10 eV, at room temperature would be order of magnitudes larger than the sensitivity required for the detector.

The third fundamental element is the (weak) thermal conductance to the thermal bath. In CUORE the thermal bath is represented by the coolest part of the cryostat.

3.1.2 Bolometer response

A model for the bolometer response can be derived by considering these elements only: thermal bath, absorber, sensor and their conductance (see figure 3.1 (a)). The sensor temperature time evolution, and thus the signal produced, can be derived by this two equations:

$$\frac{dT_a}{dt} = \frac{G_{as}(T_s - T_a) + G_{ab}(T_b - T_a) + P(t)}{C_a} \tag{3.4}$$

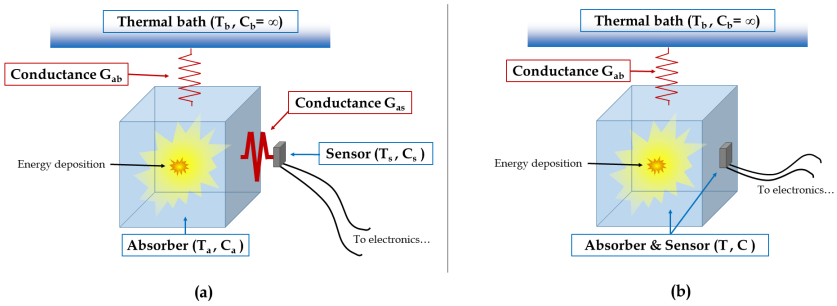

Figure 3.1: *Schematic representation of a bolometer: (a) shows the three main elements of a bolometer and the thermal conductances described in equations 3.4 and 3.5, (b) represents the simplification described in equation 3.6 in which the absorber and the sensor are considered the same object in thermal equilibrium ($G_{as} \to \infty$ so that $T_s = T_a$).*

$$\frac{dT_s}{dt} = \frac{G_{as}(T_a - T_s)}{C_s} \tag{3.5}$$

The first describes the energy balance for the absorber as a function of its thermal capacity C_a, the conductance to the thermal bath and to the sensor, G_{ab} and G_{as}, the temperatures of the absorber T_a, the sensor T_s, the bath T_b and the power deposition due to the crossing particle $P(t)$. The second is the analogue balance for the sensor. If $G_{as} \gg G_{ab}$ then we can simplify the system considering the absorber and the sensor as a unique object (see figure 3.1 (b)), which means $G_{as} \to \infty$ so that $T_a = T_s = T$, obtaining

$$\frac{dT}{dt} = \frac{dT_a}{dt} = \frac{dT_s}{dt} = \frac{G_{ab}(T_b - T_a) + P(t)}{C} \tag{3.6}$$

where $C = C_a + C_s$. In we consider $P(t)$ as an instant energy deposition E we have an instant rise time followed by an exponential decay

$$T(t) = T_0 + \frac{E}{C(T)} e^{-t/\tau} \tag{3.7}$$

where T_0 is the temperature of the bolometer before the particle event, also called baseline temperature, and $\tau = C/G_{ab}$.

The here explained model of bolometric detector actually misses a fourth fundamental element included in CUORE detectors: the Joule heater. Given the nonlinarity of the NTD resistance as function of temperature and the temperature dependence of the thermal capacity, the sensor response depends on the temperature of the thermal bath. This means that two particle events, that cause the same energy deposition, produce two pulses of different am-

plitudes if the bolometer is not operating at constant temperature; this effect potentially harms any reasonable energy reconstruction. To reconstruct the temperature dependence of the pulse amplitude, a kind of "thermal calibration" is performed. During the data acquisition a constant amount of energy is periodically deposited on every bolometer thanks to a small resistor, the Joule heater or simply heater, glued directly on the crystal. The detector response is registered, as it happens for a particle event, and flagged as "pulser event"; at the same time the baseline just before and after the pulse is saved in the pulse window and used as a reference for the crystal temperature. At the end of a run, pulser events are analyzed to find the empirical relation between the bolometer response and the detector temperature, similarly to what happens for the energy calibration. This procedure will be discussed in section 4.2.

3.2 CUORE experiment

CUORE aims to reach the half-life sensitivity of $0\nu\beta\beta$ decay of ^{130}Te of $T^{0\nu}_{1/2} = 9.5 \cdot 10^{25}$ years (at 90% C.L.) in five years of data taking, in order to approach the inverted hierarchy region (see figure 1.2). As expressed in formula 1.13, the sensitivity to $0\nu\beta\beta$ decay is given by fours main factors: (i) large mass of candidate nuclei, (ii) long live time, (iii) good detector energy resolution and (iv) low background in the region of interest (ROI). Large mass requirement is matched by using an array of TeO_2 crystal, whose total ^{130}Te content is 206 kg (i.e. $\sim 10^{27}$ atoms of ^{130}Te). Good energy resolution is provided, in principle, by the bolometric technique: CUORE goal is to reach a FWHM resolution in the $Q_{\beta\beta} = 2527.5$ keV region of 5 keV, operating at $\sim$10 mK. Finally, the background index, in the ROI, is expected to be < 0.01 counts/keV/Kg/year.

The CUORE experiment is placed in the hall A of Laboratori Nazionali del Gran Sasso (Italy), at a depth of about 3500 meters of water equivalent, in a dedicated three-floor hut (see figure 3.2). The hut includes the clean room at the first floor - where the detectors have been prepared, the cryostat has been commissioned and will remain during the data acquisition - and the control room that hosts the electronics and the Data Acquisition System. The ground floor hosts the "external shielding": a $\sim$80 tons lead shield that can be raised up, through the clean room floor, up to the cryostat height.

3.2.1 Detectors array

CUORE is composed by 988 independent bolometric detectors, each one made of a 5×5×5 cm^3 TeO_2 crystal of 750 grams, a Ge-NTD sensor and

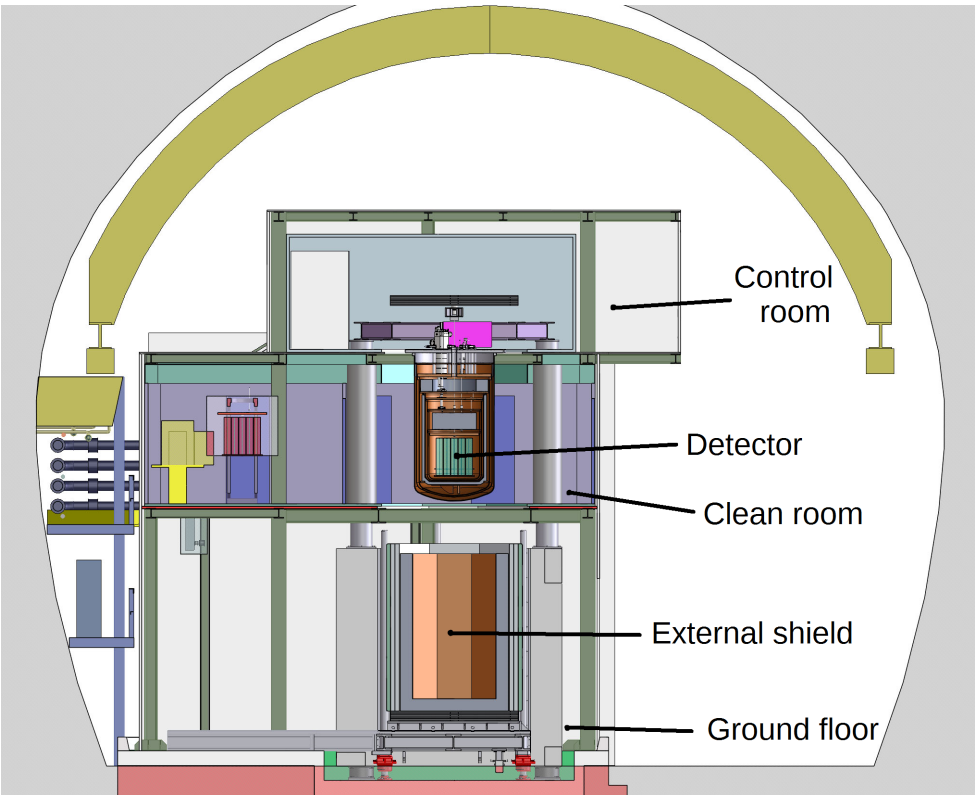

Figure 3.2: *Section of hall A with a schematic of the CUORE hut.*

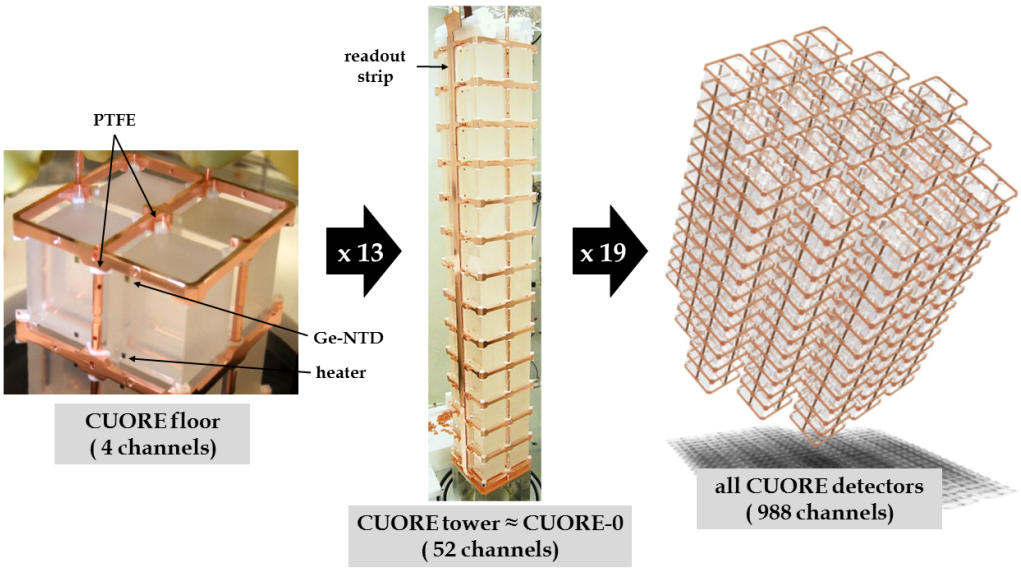

Figure 3.3: *CUORE detectors array. From left to right: every TeO_2 crystal is equipped with a Joule heater, a Ge-NTD thermistor, and is fixed to the copper frame by Polytetrafluoroethylene (PTFE) elements. Four crystals form a CUORE floor. 13 floors are grouped to form a CUORE tower of 52 crystals, on two opposite sides of every tower the read out strips are fixed. The 26 heaters and 26 thermistors are connects through 25 μm diameter gold wires to the read out strips. 19 towers form the CUORE detectors array.*

a Joule heater (whose purpose has been briefly explained in section 3.1.1), both glued on a side of the crystal. The crystals are arranged, by means of a supporting structure, in four-crystal floors, side by side; 13 floors form a tower (for a total of 52 detectors) and the 19 towers that compose all the CUORE sensitive volume, are grouped to form a cylindrical volume (see figure 3.3). Signals from NTDs and heaters go through copper traces placed on strips of Polyethylene Naphthalate (PEN) that are vertically fixed along two sides of each tower. The copper traces lower extremity are then connected to the corresponding pin, of an NTD or heater, using 25 μm diameter gold wires. The upper extremities are connected, through to the so-called *junction boxes*, to the wires that communicate to the cryostat outside.

The structure used to hold the crystals must satisfy some fundamental requirements: (i) the thermal conductivity must be low enough to be negligible during the signal rise time (in order to satisfy the approximation $G_{as} \gg G_{ab}$ previously described); (ii) the same thermal conductivity must be high enough to guarantee the absorber re-cooling, after the particle event, in a reasonably short time; (iii) the connection between the structure and the

Component	^{232}Th (g/g)	^{238}U (g/g)
TeO_2 crystals	$2.1{\cdot}10^{-13}$	$5.3{\cdot}10^{-14}$
Copper	$5.0{\cdot}10^{-13}$	$5.3{\cdot}10^{-12}$
NTD sensors	$1.0{\cdot}10^{-9}$	$1.0{\cdot}10^{-9}$
Bonding gold wires	$1.0{\cdot}10^{-8}$	$1.0{\cdot}10^{-9}$
Joule heaters	$8{\cdot}10^{-11}$	$1.7{\cdot}10^{-10}$
PTFE elements	$1.5{\cdot}10^{-12}$	$1.8{\cdot}10^{-12}$
PEN cables	$4.4{\cdot}10^{-10}$	$1.1{\cdot}10^{-10}$
Glue	$2.2{\cdot}10^{-10}$	$8.2{\cdot}10^{-10}$

Table 3.1: *Radioactive contaminations for all the detector components, espressed as 90% C.L. upper limits. Values from [11].*

crystals must avoid power dissipation by friction; (iv) the thermal expansion for all the components must be considered and (v) only radio-pure material can be used. The main holding structure is made of ultra-pure copper to accommodate requirement (v). Table 3.1 shows ^{232}Th and ^{238}U contents measured for all the array materials.

The contact between the copper and the bolometer is made by small elements of Polytetrafluoroethylene (PTFE), designed so that every crystal angle is touched. PTFE elements account for thermal expansion, thermal conductivity and do not produce excessive energy dissipation by friction. The low radioactivity requirement heavily affected the tower assembly procedure designed to avoid detector contamination. (see ref. [90] for a detailed description of the tower assembly procedure). It has been tested with CUORE-0, before to be adopted for the realization of the large scale experiment, CUORE-0 had the same structure but was composed by only one tower. The tower commissioning process can be schematized in three main activities, all fulfilled in a clean room: sensor attachment (gluing), tower assembly and wire bonding.

An NTD and heater are glued to the crystal by nine and five spots, respectively, of Araldit rapid epoxy, 0.4 to 0.7 mm wide and 50 μm thick. Since the size of the spots affects the thermal conductivity between the absorber and the sensor, and thus the pulse shape, the gluing phase has been automatized by using a robot to make the procedure as reproducible as possible. Every crystal has been loaded inside the glove box illustrated in figure 3.4, in order to maintain the detector components under nitrogen atmosphere, where a "cartesian robot" was used to place the precise amount of glue on thermistor and heater. Then the crystal was placed on these two elements by a robotic arm, successively removed from the glove box and placed into vacuum-sealed boxes. Tower assembly was performed in a custom workstation designed to accommodate different removable task-specific glove boxes

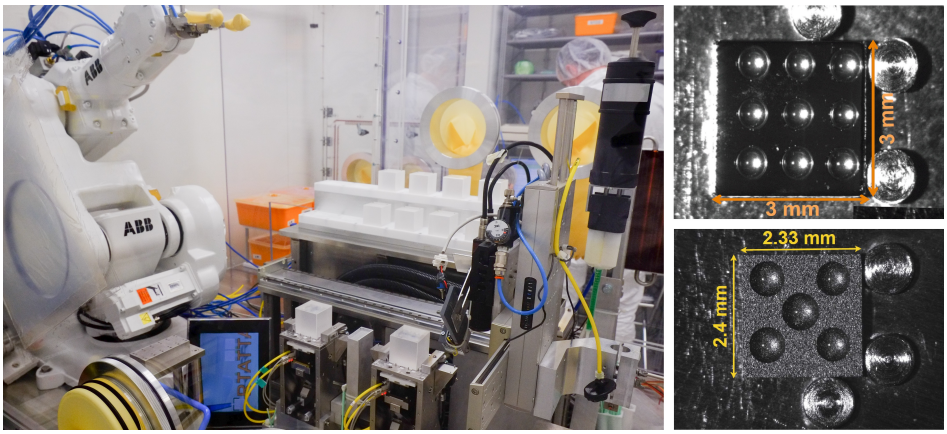

Figure 3.4: *LEFT: The glove box where NTD sensors and heaters are glued to TeO_2 crystals. The two robots are also visible in the picture: on the left side it is the robotic arm used to move the crystal, on the right side it is the cartesian robot used to deposit the glue. RIGHT: Size of Ge-NTD (top) and heaters (bottom) chips, the glue spots can be see on both chips.*

(figure 3.5). It basically consisted in the bottom-up, floor by floor, construction of the tower copper structure, inserting crystals and PTFE elements. When a tower was ready, the PEN strips were fixed on two opposite sides and the electrical connections between the chips and the readout traces were made. Two 25-μm-diameter gold wires were bonded per each connection for redundancy (figure 3.6). Once a tower was completed, it was stored in nitrogen-fluxed cylinder-shape containers to await for the installation inside the cryostat (figure 3.7).

3.2.2 CUORE cryostat

CUORE crystals, as well as CUORE-0 crystals, must be operated in the temperature range 6 to 10 mK, this requires a custom made cryostat equipped with a $^3He/^4He$ dilution unit with a cooling power of the order of 3 mW at 120 mK. The peculiarity of CUORE cryostat [91], apart from the extraordinary size, is that it doesn't use cryogenics liquids but Pulse Tubes (PT) to reach the first cooling down to 4 K, this increases the experiment duty cycle because, differently from a cryogen refrigerator, does not require liquid Helium refill. Moreover a liquid Helium refrigerator includes the 1-K pot, where gaseous Helium is pumped out from liquid Helium, which is needed for the condensation of the incoming Helium mixture. and CUORE-0 experience taught that 1 K pot is a source of vibrational noise.

The entire cryostat (shown in figure 3.8) is suspended on a structure

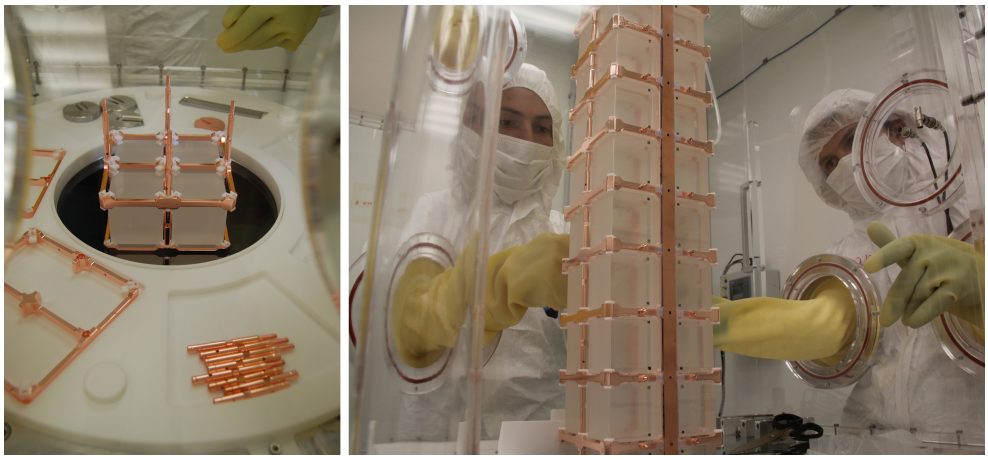

Figure 3.5: *The tower assembly procedure.*

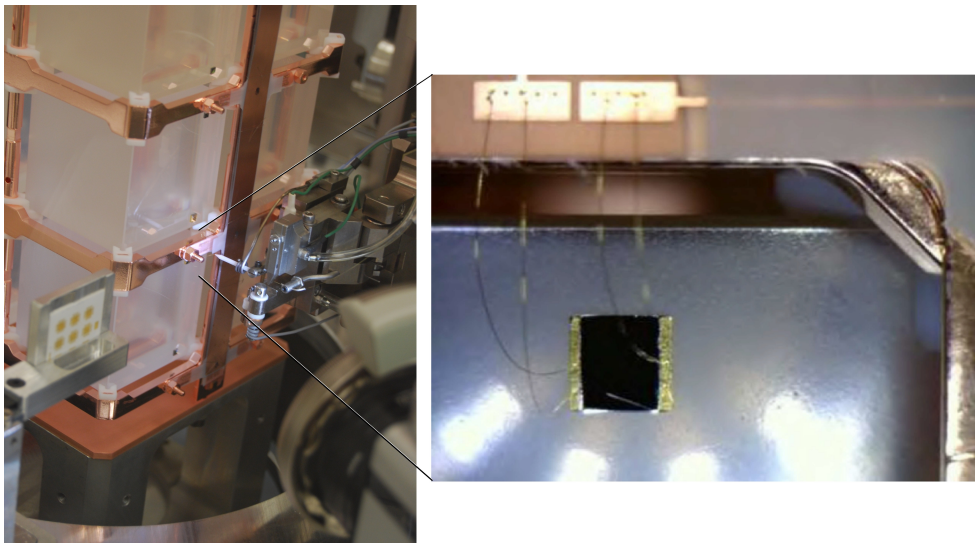

Figure 3.6: *The bonding procedure. The right picture shows a Joule heater bonded with four gold wires for redundancy.*

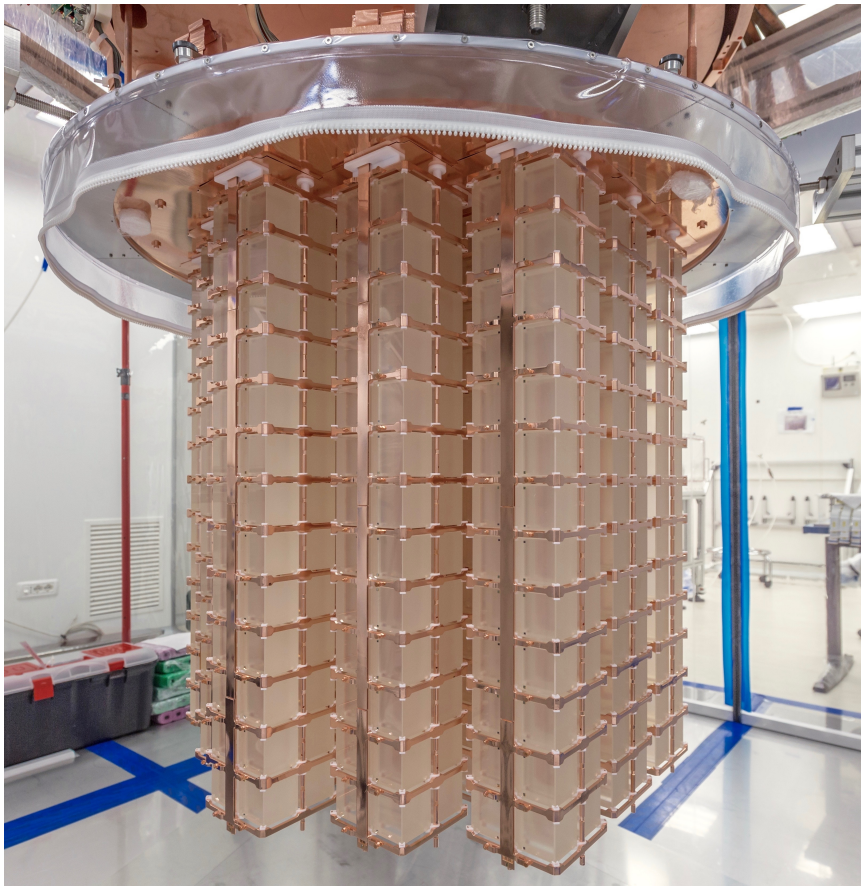

Figure 3.7: *All the 19 CUORE towers at the end of the tower installation phase.*

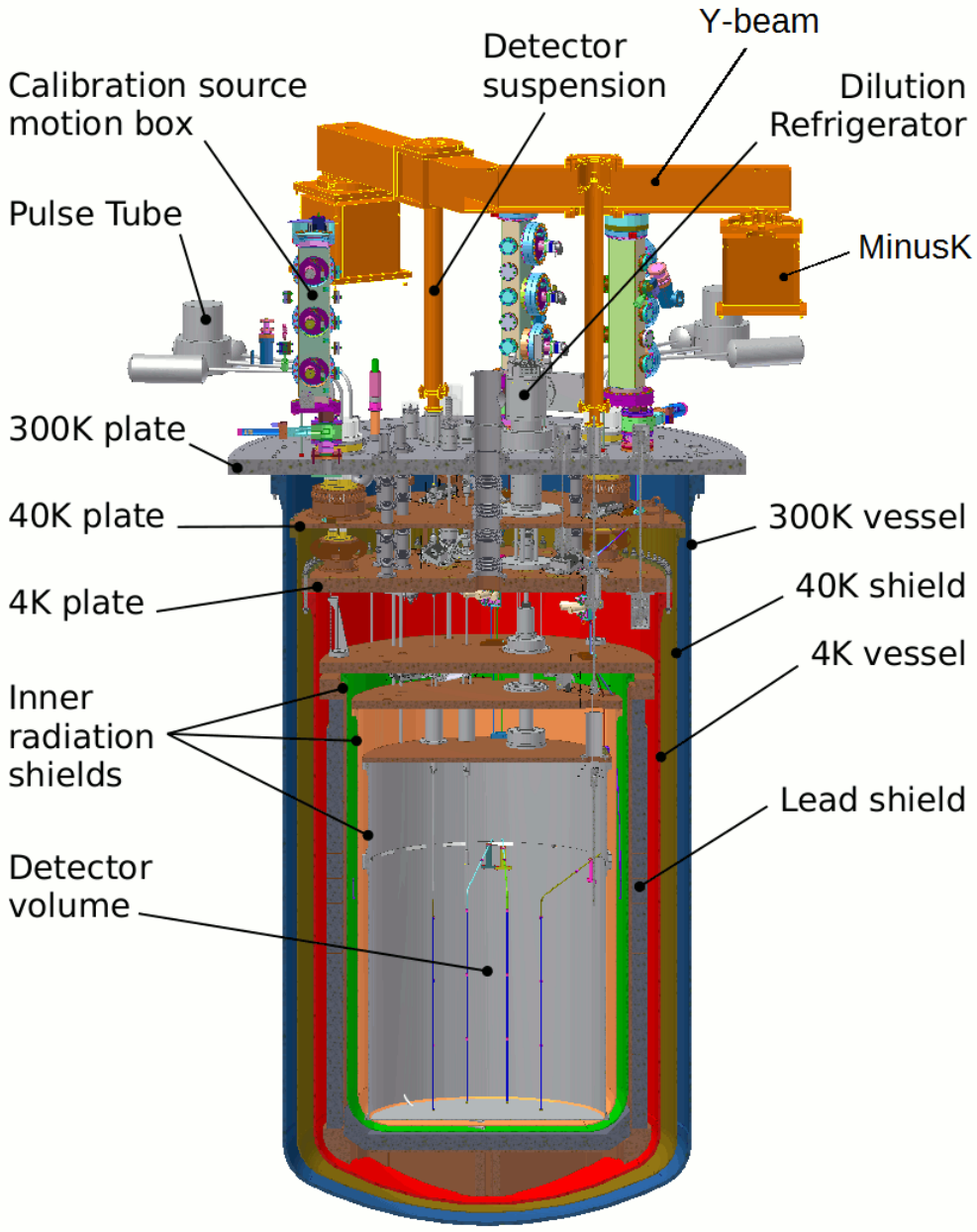

Figure 3.8: *The CUORE cryostat. To give an indication about the scale, the biggest vessel (300 K) is roughly 3 meters high. Image from [10].*

called Main Support Plate (MSP), at the level of the second floor of the hut, thanks to three stainless steel cables. Such suspension helps to limit the injection of mechanical vibration directly to the cryostat, for the same reason the detector array is not rigidly coupled to the cryostat but is independently suspended to the rigid structure (Y-Beam), connected to the MSP by using three damping suspensions called MinusK®.

The cryostat can be divided in two, vacuum tight, volumes: the innermost is called Inner Vacuum Chamber (IVC) and is completely[1] surrounded by the external volume called Outer Vacuum Chamber (OVC). More precisely the cryostat can be divided into six volumes corresponding to different thermal stages. Every stage corresponds to a copper vessel and a surrounding plate. Their names comes from the nominal temperature they reach during the operations, from outside they are: 300 K, 40 K, 4 K, 600 mK, 50 mK and 10 mK.

The 300 K vessel delimits the OVC and its plate is fixed to the MSP. Its top part, the 300 K plate, hosts several elements such as the ports for readout and thermometry cabling, the Detector Calibration System motion boxes (see section 3.2.4) and the turbomolecular pumps.

At the 4 K plate the cold fingers of the five pulse tubes are fixed, and the 4 K vessel delimits the IVC volume. The mixing chamber of the dilution unit is fixed on the 10 mK plate and is the coolest part of the cryostat. The Tower Support Plate (TSP), where the detector towers are hanging, is placed inside the 10 mK vessel but is independently suspended, thanks to the Detector Suspension, to the Y-Beam to take advantage of the MinusK® damping suspensions.

Inside the 10 mK vessel, above the Tower Support Plate, the top lead shield is placed; it consists of a cylinder 24 cm high. In order to provide an analogue shielding in all the directions, 6 cm thick lateral and bottom lead shields are also present. In particular these last two are made with roman lead that has been found in a roman ship which sunk about 2000 years ago. This gave any radioactive isotope of lead many half-lives to decay away. Radioactivity measurements of ^{210}Pb activity in roman lead gave a value lower than 0.004 Bq/kg [92]. Furthermore, the external shield of modern lead (150 $\pm$ 20 Bq/kg) will be raised up, from the ground floor of the hut, around the cryostat during the operations. Including the internal lead, the cryostat will cool a mass of $\simeq$1.5 tonnes down to 10 mK, with a mass of $\simeq$10 tonnes operating below 1 K.

[1] Except for some ports that connect the IVC with the outside used, for example for the cabling connection.

3.2.3 Cool down procedure

The cooling procedure, successfully tested during the last three years, is carried out in three steps. The first one is performed by the so called Fast Cooling System (FCS). It consists in flushing gaseous Helium cooled down to about 40 K, thanks to three Gifford-McMahon (GM) cryocoolers, inside the IVC. This technique permits to cool down a mass of about 15 tonnes and is able to bring the apparatus to the temperature of 50 K in about two weeks. When the temperature of 100 K is reached, five Pulse Tubes (PT) are used to cool down the system to 4 K. Four of them are enough for cryostat operation, they provide a nominal cooling power of 1.5 W at 4.2 K each, so maintenance operations of a PT are possible without warming up. Four pulse tubes are able to cool the cryostat from 100 K to few K in about two days. Finally the base temperature of 10 mK is reached via a customized Dilution Refrigerator (DR), produced by Leiden Cryogenics in Netherlands, with a nominal cooling power of 5 μW at 12 mK. The DR works with $^3He/^4He$ mixture that continuously flows through two condensing lines, with different impedances, thermalized with PT's, and reaches the mixing chamber placed on the 10 mK plate. The condensing lines, they are two for redundancy, are termalized with two PTs in order to have the precooling, at 4 K, of the incoming mixture.

3.2.4 Detector Calibration System

CUORE detectors will be regularly calibrated, roughly once a month, by means of Thorium sources. ^{232}Th is used because of the large number of γ-peaks produced by its daughter nuclei, including the 2615 keV line produced by ^{208}Tl, wich is very close to the $0\nu\beta\beta$ region of interest. The shielding inside the cryostat and the homogeneous exposure of all the channels imply that the calibration sources need to be placed directly between the towers and just outside the 50 mK vessel. This means that the sources must be cooled at the detectors base temperature before the deployment and be removed from the innermost part of the cryostat after the calibration run. Detector Calibration System [93] accomplishes this task providing the hardware required to move and thermalize the sources. In particular, the $\gamma-$sources are flexible Kevlar strings to which 34 or 33, depending on the string, copper capsules are fixed. Each capsule contains a 5 mm-long thoriated tungsten wire and is coated in PTFE. During background data taking, the strings are rolled up inside the vacuum-tight motion boxes, placed on the top of the 300 K plate, outside the internal lead shield. At the beginning of a calibration run they are unrolled down to the detector height through dedicated guide tubes, PTFE capsule

coating is used to reduce the friction with the tubes. Just below the 4K plate, four thermalizer stages are are used to cool down the strings during the displacement. Source activity and their distribution are tuned to produce a counting rate, after pile-up rejection, from 35 to 50 mHz on every crystal; this rate is high enough to collect sufficient statistics in three days, as in CUORE-0.

3.2.5 Electronics

CUORE readout electronics is composed by two fundamental components: Front End boards (FE) and Bessel filters. FE boards are placed over the MSP, to make the signal path, from the Fischer Boxes to the boards, as short as possible. They have two functions: provide the bias current required to measure the NTDs resistance, and amplify the signal.

Each thermistor is polarized as shown in figure 3.9 (left), the load resistance R_l can be set to 10 GΩ or 60 GΩ, so $R_l \gg R_{bol}$ ($R_{bol} \sim 100M\Omega$) and the bias current I_{bol} is almost independent of the sensor resistance. Under this approximation the signal $V_{bol}(T) = I_{bol}R_{bol}(T)$ is proportional to the thermistor resistance only. Nevertheless the power dissipated by Joule effect $P = I_{bol}^2 R_{bol}(T)$ increases the sensor temperature, and thus decreases R_{bol}, this effect is called electrothermal feedback. The equilibrium is reached when the same power is transmitted to the thermal bath through the thermal conductance G_{ab} (see figure 3.1): $T_{bol} = T_b + P/G_{ab}$. In fig 3.9 (right) the load curve shows the dependence between I_{bol} and V_{bol}: for small currents the temperature variation of the sensor is negligible and the I-V curve is almost linear; for greater values of I_{bol} the electrothermal feedback increases the slope of the curve up to the inversion point, where V_{bol} decreases even increasing the current. The working point is the configuration, defined by the bias current, used to operate the bolometer. The optimal working point is the one that maximize the signal to noise ratio, but the corresponding bias depends on the detector condition and the characteristics of the sensor. In practice it must be empirically determined by scanning the values of V_{bias}, and this operation must be repeated when the cryostat conditions change.

Given the typical parameters of the CUORE bolometers, with thermal capacity $C \sim 2{\cdot}10^{-9} J/K$, an energy deposition of MeV causes a temperature rise of the order of 100 μK and a voltage variation of $\Delta V/V = \eta{\cdot}\Delta T/T \approx 0.1$ (where η is the logarithmic sensitivity defined in equation 3.2) which means 100 μV for $V_{bol} = 1$ mV [11].

Every FE board independently handles up to 6 channels, by providing a stable bias voltage, summing an adjustable offset to V_{bol} to maintain the output at the end of the readout chain within the digitizers dynamic range,

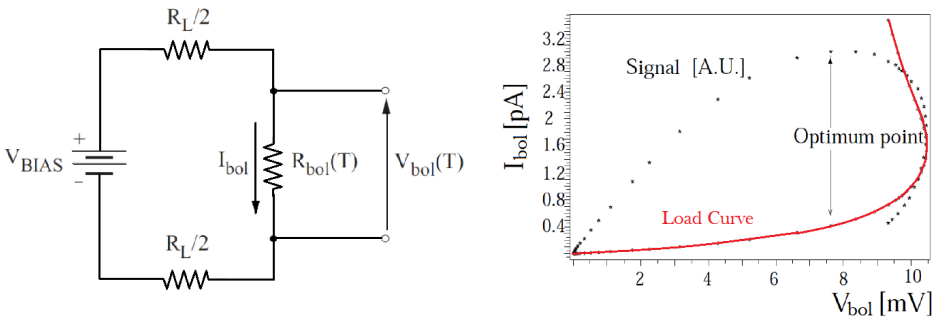

Figure 3.9: *Left: schematic of the circuit used to polarize the NTD sensor. Right: typical I-V curve of a Ge-NTD sensor, showing the electrothermal feedback.*

and amplifying the resulting value. The FE parameters like gain, bias, offset and load resistance are remotely programmable, so that a channel dependent optimization can be accomplished. The gain, obtained by the combination of a preamplifier and a Programmable Gain Amplifier (PGA), can be set in the range 20 - 10^4. Signals are read in direct current mode (DC) because the amplitude of the thermal pulses depends also on the detector temperature so the baseline value (i.e. the value read just before the signal) is used as temperature reference for the particle energy reconstruction. The thermistor signal is not referenced to ground but is acquired in differential mode, because in this way the common mode noise is automatically suppressed.

Signals coming from the FE, are then filtered by custom made, anti aliasing, low-pass filters. The filtering boards take advantage of a six-pole Bessel filter, providing an attenuation of 120 dB/decade, with a cutoff frequency that can be remotely set to 15, 35, 100 or 120 Hz. Every filter board handles 12 channels. Given the characteristic time of the physical processes involved in the signal production, e.g. the rise time of the signal is tens of ms, a sampling frequency of about 100 Hz is enough to reconstruct the signal shape. Typical values of the sampling frequency are 125 Hz and 1 kHz, according to the filter cutoff to avoid the aliasing effect. After the filtering, the signals are digitized by commercial modules and the samples are processed online by the triggering algorithm.

CUORE electronics includes the Pulser boards, used to send electric pulses to the Joule heaters. A run by run characterization of the thermistor response is required because of the dependence of the bolometer response on the temperature (see section 3.1.1). Dedicated boards, simply called Pulsers, are used to send a precise amount of energy on the Joule heaters and simulate a particle-induced energy deposition. Each Pulser board can send a square

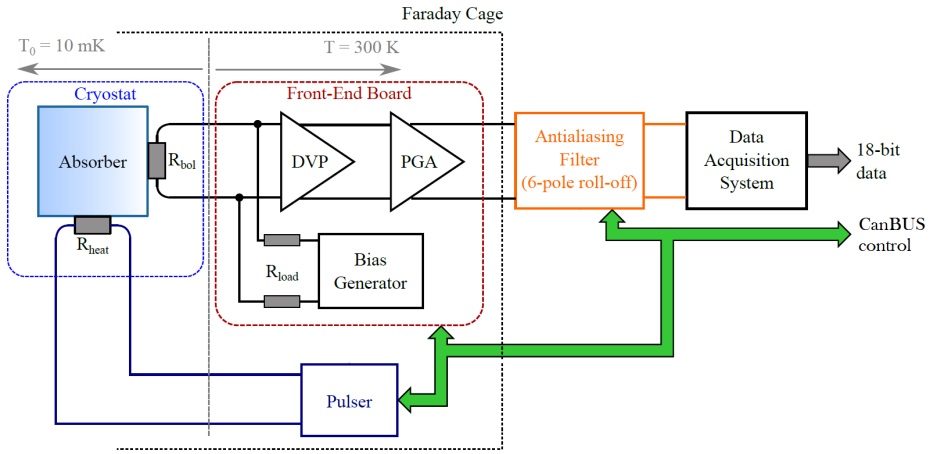

Figure 3.10: *Schematic of the readout chain. The thermal sensors are polarized by the Front End boards (bias generator) and the voltage across the NTD is amplified (DVP and PGA), filtered and digitized. In addition to this, the pulser boards provide the signal for the Joule heaters. All the custom made boards (FE, filters and pulsers) can be remotely configured thanks to the CAN bus communication (described in section 3.3.2). Image taken from [11] (the original image was used to show the CUORE-0 electronics, but has been modified to reflect the CUORE system).*

signal, of adjustable amplitude and duration, into four separate channels, by means of a set of relays; every channel is connected to a detector column so a Pulser board accounts for a detector tower. The energy of the pulses is not fixed but can assume a set of values to scan the thermistor response at different energies.

FE boards, Bessel filters and the Pulser boards are fed by 5 GENESYS^{TM} 750W/1500W Programmable DC power supplies produced by TDK-Lambda [94]. The bias current is provided by two 2231A-30-3 Triple-channel DC power supply produced by Keithley [95]. Lambda power supplies are not directly connected to the boards but the power pass trough the direct-current-to-direct-current filters (DcDc) whose purpose is to reduce the noise coming from the power grid. DcDc, as well as FE and Bessel, are custom boards developed in Milano Bicocca University. Figure 3.10 shows the scheme of the electronics system.

3.3 Data Acquisition System

The CUORE Data Acquisition System has been developed in the last years in Genoa and represents a large part of my PhD work. The main structure

has been inherited from an existing system developed during the CUORICINO experiment and adopted for CUORE-0 data acquisition. Nevertheless it required major upgrades in order to accommodate an order of magnitude increase in the number of channels to be handled. In this section, after an overview of the system and the general requirements to be satisfied, a description of the single parts will be given, highlighting the differences with respect to the CUORE-0 DAQ.

The fundamental purposes of the acquisition system are the following: (i) to digitize ∼1000 analog signals, (ii) to send and acquire the pulses used for the bolometer offline stabilization (introduced in section 3.1.1), (iii) to perform a first triggering algorithm, (iv) to manage the electronics configuration, (v) to keep track of the runs and their sensible information.

The CUORE DAQ hardware is basically composed of the digitizing modules, purchased by National Instruments, whose data are collected by six computers called *Data Readers*, a computer used for the event construction, called *Event Builder*, and the network infrastructures for the communication between the computers and with the electronics. All the computers use the operating system Scientific Linux; a Linux distribution developed at CERN and Fermilab for scientific purpose [96].

The acquisition software, called `Apollo`, is written in the C++ language with some scripts written in `bash`, `python` or specific language such as `psql`. It is mainly custom code with the exception of the National Instruments drivers and the ROOT package. `Apollo` is a collection of several processes, running independently on the computers, that perform specific tasks: reading the samples acquired by the digitizer boards; applying the trigger algorithm and writing the samples to disk for offline analysis. Aside from this, it includes graphic interfaces and ancillary processes used, for example, to manage the electronics boards and the pulser boards.

A `PostgreSQL` database, accessible by all the `Apollo` processes, is used to store information about the runs, the geometrical distribution of the detectors, the readout chain mapping for every analog channel, the configuration of the electronics, the triggers and event building parameters.

3.3.1 DAQ boards

The digitization of NTD signals is done by an array of National Instruments modules (PXI-6284) [97]. Every digitizer module uses a 18-bit Analog-to-Digital Converter (ADC) and has 16 differential inputs and 48 digital I/O. Modules are placed into six different National Instruments chassis (PXI-1044) of 14 slots each [98]. The first slot of every chassis is occupied by the controller module (PCI-PXI-8336 [99]) that reads digitized data from the other

modules, thanks to the chassis PXI bus, and sends the samples to a computer called *Data Reader*, using a dedicated optical link. Every Data Reader computer runs an independent process, called `DataReader`, whose purpose is to read the samples from the controller it is connected to, to copy them into a shared memory accessible by other `Apollo` processes, and write them to disk. The six chassis connected to six Data Readers, contain, in total, 64 digitizer modules so they can acquire, in differential mode, up to 1024 channels. The analog signals features justify the choice of a 18-bit resolution. Indeed, considering a dynamic range of 21 V, the single-bit resolution results about 40 μV, well below the noise produced by other sources: in CUORE-0 the typical baseline RMS was of the order of 1 mV. In [100] has been shown that 1 kHz is the achievable sampling rate avoiding cross-talk affects between the channels acquired by the same module.

As opposed to the case of CUORE-0, for which a single National Instruments chassis was enough to acquire all the channels, the necessity of acquiring simultaneously six digitizer chassis leads to some complications. The most relevant is to ensure the synchronous data acquisition among the chassis. The beginning of the acquisition of a single chassis can be done by sending a specific signal from the Data Reader computer to the controller module, by means of the optical link. One can imagine a system in which a master computer sends a signal to the remaining five slave computers, for example by using a network protocol such as TCP/IP, to trigger them to start the acquisition on the corresponding chassis. However, this solution cannot be adopted because every Reader would suffer a different delay, depending on the status of that machine, leading to an unpredictable time misalignment and thus an asynchronous acquisition. The adopted solution was to implement a communication between the chassis, so that a master chassis receives the trigger from its Data Reader and sends a signal directly to the slave chassis. The communication takes advantage of the digital I/O ports of the digitizing modules, that can be used to connect the digitizer of a certain chassis to the digitizer of an other.

Here is how this procedure practically works: all the `Apollo` processes, independently from the hosting computer, are managed by a single process, the `DaqServer`, that can run on a separate host and send network commands. When the `DaqServer` receives the request to start a new run, it puts the `DataReader` processes, hosted by the slave computers, in "waiting" status. This means that the `DataReader` is ready to acquire data but its NI chassis will start the digitization when receiving the input on a specific digital channel. After that, the `DaqServer` sends to the master `DataReader` the command to start the acquisition of its NI chassis. This chassis, starting

the digitization, sends a signal on the digital output channel which is connected to the digital input of the slave chassis. In this way the data from slave chassis are synchronous, while the ones from the master chassis have an anticipation smaller than 1 ms (i.e. the minimum sampling period used in CUORE-0).

Every chassis has a 10 MHz internal clock that can be shared among the digitizer boards. To avoid the time misalignment during data taking, all the digitizer boards in the DAQ must share the same clock signal, so the chassis clock can not be used. In this case some BNC coaxial cables are used to share the clock of a master chassis, among the other chassis, by using dedicated BNC connectors on the chassis back panels. The synchronicity has been validated by acquiring a square waveform with two digitizers, placed in different chassis, and using the digitized waveform to estimate the relative delay. Figure 3.11 shows that the signals are aligned when the clock is shared, while the disconnection of the BCN cable causes a time misalignment of the order of 1 ppm, compatible with the producer specification of 25 ppm.

Every NI chassis is associated with a crate of patch boards used connect the cables coming from Bessel filters with the cables going to DAQ digitizers. The NI chassis are mounted in two cabinets, in the CUORE control room, that are linked by the cables used for the digital communication (e.g. the inter-chassis signal used to start data acquisition) and the BNC cables used to share the clock signal. A third cabinet, linked to the first two by the optical links used for the samples transmission, contains the Data Readers and the Event Builder, with the network switch used for the communication between the DAQ computers and to the external network.

3.3.2 Slow Control

As explained in section 3.2.5 the CUORE readout chain is made of two main active devices: the Front Ends and the Bessel Filters. The parameters of both devices can be configured to address the acquisition requirements that can vary channel by channel or run by run. For example the temperature of the thermal bath can change among the runs, causing a variation in the working point of the thermistors. In this case the data acquisition can be optimized by changing the values of the bias and consequently the gain of the FE amplifiers, or changing the value of the load resistances (series with the NTD in the bias circuit). Or else, a run can be focused on detector noise characterization then the cutoff frequency of the filters can be increased or the filter can be disabled. To guarantee the adaptability of the acquisition chain, not requiring a direct intervention on the hardware, every device is equipped with a microcontroller able to communicate on Controller Area Network bus

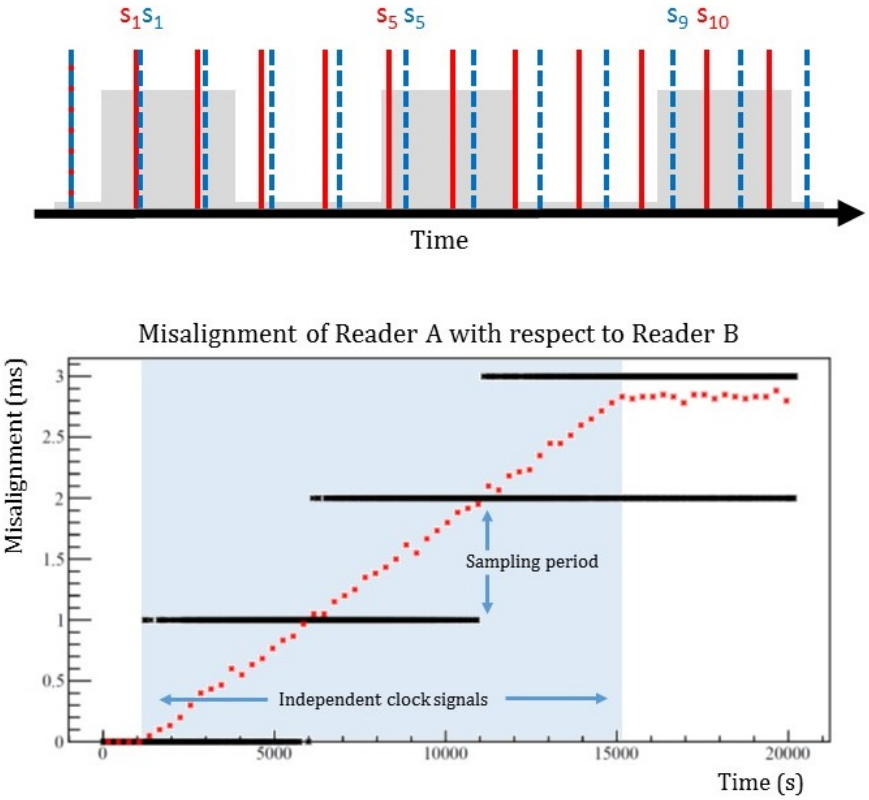

Figure 3.11: *Top: The same square waveform (shaded gray) is digitized by two ADCs driven by different clocks, placed in different NI chassis. The vertical lines (solid red for a ADC, dotted blue for the other) represent the time at which the waveform is sampled. By comparing the sample id corresponding to the transition from the low to the high state (in this example: 1, 5 and 9 with respect to 1, 5 and 10), it is possible to monitor the misalignment over time. Bottom: The black dots represent the measured misalignment between two chassis as a function of time. The sampling frequency is 1 kHz, so the difference between the samples id is always a multiple of 1 ms, while the square waveform period is 1 s. The red dots represent the average of the misalignment values over 300 s. At the beginning of the run BNC cable is connected and the misalignment is zero, so the delay due to the inter-chassis communication is negligible, it grows when the BNC used to share the clock signal is disconnected (blue shaded region), and remains constant when the common clock is restored.*

(CAN bus). CAN bus is a message-based communication standard used to connects a variable number a devices, in which every device can send and receive messages not simultaneously.

The CAN bus communication is also used to configure the Pulser boards and DcDc filters. `PulserController`, in particular, is the process that periodically communicates the pulse parameters to the boards, and successively the trigger signal that causes the Pulsers to fire. The same trigger is sent to the acquisition system, once again by using the digital lines of the NI digitizers, that in this case are acquired and grouped to form an 16-bit channel similar to the analog ones. In this way the event caused by the pulse can be tagged during the event building phase. Aside from this, Keithley and Lambda power supplies are remotely controlled, by serial communication protocol.

`SlowServer` is the process that remotely handles the electronics devices, it runs on the computer physically connected to the devices and it can accept requests by other `Apollo` processes. It masks the device-specific communication protocols with a unique network communication protocol that can be used by other processes, even when they are not hosted by the same machine, to interact with the electronics. In this way the whole system maintains high modularity, avoiding potential conflicts between the `Apollo` processes.

A similar system has been implemented for CUORE-0 DAQ but both the electronics boards and the communication protocol have been changed (in that case the I^2C protocol was used) so the software has been updated. Moreover the new `SlowServer` allows the parallelization of the commands, speeding up the electronics configuration procedure. This is a fundamental requirement if we consider that a single command can take few seconds to be accomplished and that, therefore, the configuration of the whole system could take several hours.

3.3.3 Online trigger and event building

During the data acquisition the six `EventReader` processes copy the digitized waveforms from the digitizer boards to shared memory buffers, one per each acquired channel, on the hosting Data Reader computers. The shared memory acts as a circular buffer that can be read by other processes. At that moment the samples stream can be processed by the trigger finder. Given the low sampling frequency and the low trigger rate, a software trigger is implemented. This has the advantages that more than one trigger algorithm per channel, associated to different trigger flags, can be defined and that, even the same algorithm can be used with different, channel dependent, parameters. In CUORE a trigger can be of two types, called noise and event.

The noise trigger is a simple trigger that randomly fires with given probability per unit of time. It is used to acquire time windows that, apart from accidental coincidence, do not contain events, used for the detector noise characterization. The purpose of a run by run noise characterization will be explained it section 4.1. In addition to the firing probability, a specific noise trigger has an associated post-trigger dead time.

The event trigger is basically a derivative trigger. The absolute value of the baseline depends on cryostat and electronics conditions, so a physical pulse can not be identified by a baseline absolute value but thanks to the fast temperature raising it causes. The event trigger requires that the difference of two samples, which is proportional to the derivative, at a given distance (average) exceeds a given value (threshold) for a certain number of samplings (debounce). The parameters of this simple algorithm can be optimized channel by channel, depending on the acquisition conditions and the detector noise.

Although noise triggers can reasonably have the same parameters for all the channels, derivative triggers must be configured channel by channel. In CUORE-0 they were set by hand, every time the electronics configuration changed; in CUORE the procedure of trigger optimization is automated and based on the noise characterization of every channel.

When trigger conditions are satisfied, a trigger flag is set on the corresponding sample. In parallel with the trigger finding, but delayed, the `EventBuilder` process reads the buffer and saves on disk the portion of signal that contains the trigger. Such portion, called event window, can have variable length but it is typically 5 seconds long, and starts a second in advance of the trigger flag; indeed four seconds are usually enough to fully contain the decaying tail of the pulse, while the first second of baseline will be used to reconstruct the bolometer base temperature. The `EventBuilder` is the process that actually reads the shared memories and writes the event windows into files in ROOT format (Raw Data files). The event building procedure requires computing resources that could affect the Data Reader performances, so a dedicated machine, the Event Builder precisely, is used. To make the samples available for the event building, the individual shared memory buffers on the Data Readers are mirrored on the Event Builder, by the processes `MirrorClient` (on the Builder side) and `MirrorServer` (on the Readers side).

Fortunately, the low sampling frequency, and thus the small volume of data accumulated over time, allows to save also the entire waveform, for all the channels. In this way an offline trigger can be used, even reprocessing all

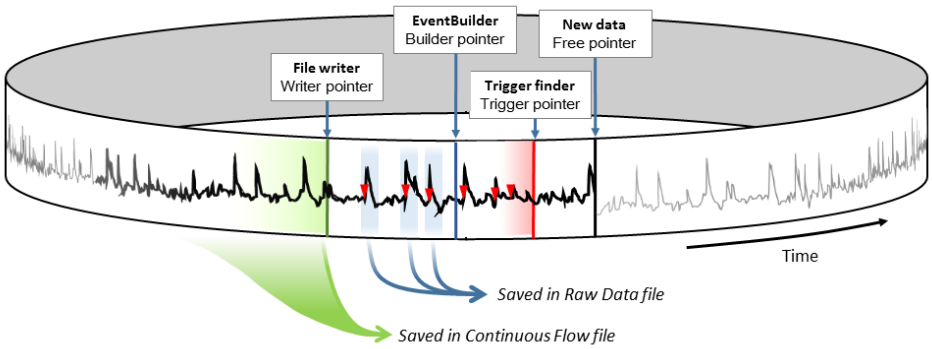

Figure 3.12: *Schematic representation of a circular buffer. Four pointers are used to keep track of the status of data into the buffer. In temporal order samples are: written in the buffer by the* `DataReader` *(free pointer), processed by the trigger algorithms (trigger pointer), mirrored by the* `MirrorServer` *to be accessible by the* `EventBuilder` *and saved in Raw Data file (builder pointer), written in Continuous Flow file by the* `DataReader` *(writer pointer). Samples behind the writer pointer can be overwritten in the buffer.*

the experimental data[2]. When a bunch of samples, on the shared memory, has been analyzed by the `EvenBuilder`, they are written to a file called Continuous Flow file.

Summarizing (see figure 3.12), the samples in the buffers pass four steps, with four associated pointers: samples are written in the buffer by the `DataReader` (free pointer), then they are processed by the trigger algorithms (trigger pointer), mirrored by the `MirrorServer` to be accessible by the `EventBuilder` and saved in Raw Data file (builder pointer), then they are written in Continuous Flow file (writer pointer) and overwritten in the buffer. The steps must be executed in this order, so a delay of one of the processes, causes the delay of the following ones.

A CUORE-0 Continuous Flow file was a text file, compressed in gz format, containing all the samples of all the channels of a single run. During a run, longer than few hours, a Continuous Flow file was closed and a new one was opened, in this cases data from a single run were split into several, chronologically ordered, partial files. In CUORE the Continuous Flow format has been changed.

A gz file, in fact, is a simple text file in which the samples are consecutively written. This strategy avoids to randomly access to samples of a given time interval, but they can be read only in sequence. This feature limits considerably the efficiency of the offline processing. The adopted solution

[2]This is the case of the analysis presented in this work.

was to change the former Continuous Flow format into a customized ROOT file, called Raw Data Continuous Flow (RDCF), because the ROOT format ensures an high speed for random access, even compressing the data (by a factor $\sim$2).

The fast access to the RDCF file allows not to save the 5-seconds-long waveforms into the Raw Data, but only the trigger timestamp. During the analysis the Raw Data files are used to retrieve the main event info and, when required, the trigger timestamp can be used to get the waveform from the RDCF file. Preliminary tests showed that the RDCF access time, for a given event window, is about two times longer than Raw Data access time (when the Raw Data contains the waveform), so it doesn't affect the offline analysis speed in a significant way.

Moreover, tests on CUORE DAQ highlighted that, in some configurations, the `EventBuilder` cannot process the data at the same speed they are produced, causing the saturation of the buffers. The slowdown of the `EventBuilder` speed was mainly due to the writing of the event windows in the Raw Data file. Avoiding the waveforms writing in the Raw Data file, this problem is solved and the `EventBuilder` speed increases.

3.3.4 Database

A `PostgreSQL` database is used to store all the apparatus information, useful for the data acquisition and data analysis, and to keep track of the measurements. The information are the geometrical distribution of the bolometers, the mapping of the readout chain (i.e. which FE board, Bessel board, digitizer is used for a given bolometer), the electronics configuration of all channels for all runs. The detector configuration, used in a specific run, is called Settings Basket (SB) and includes the list of acquired channels, the mapping, the enabled triggers and their parameters, the event building and pulser settings. The Settings Baskets must be defined by the user, saved into the database and specified at the beginning of every run. In CUORE-0 the SB management was done by means of a graphic interface but it results inadequate to manage 1000 channels, so a new easily-scalable tool has been developed. The new tool permits to use a spreadsheet as interface for the database: it dumps the information for a given SB to a spreadsheet that can be edited to produce a new SB and save it into the database.

3.4 Cryostat commissioning

After some preliminary tests of Dilution Refrigerator and Pulse Tubes, in the beginning of 2014, the cryostat was assembled in its final configuration and

four test runs were performed. The cryostat test phase lasted three years, its goal was to check the cryostat performance. Every run consisted in the integration of new parts in the apparatus followed by a cool down test and required several months. To give an indication, the cryostat dimensions imply the slowdown of the standard procedures such as the vessels handling - the weight of the vessels is of the order of 100 kg - that requires a dedicated hoist system, or the pumping that requires two days to reach the value of 10^{-3} mbar. Moreover, in order to minimize the propagation of thermal radiations, a coverage is required for every vessel, plate and, more generally, the objects that directly face a warmer part of the cryostat. For this purpose Super Insulation has been used, it consists of several layers of reflective aluminum spaced by Mylar.

The goal of the first run was to characterize the dilution refrigerator and reach the base temperature below 10 mK. After an improvement of the thermal radiation shielding, obtained by the careful usage of Super Insulation, the base temperature of 5.9 mK was obtained on the 10 mK stage. The temperature measurements, in the mK range, were done with different thermometers: a Cerium Magnesium Nitrate (CMN) magnetic thermometer, a noise thermometer which uses the relation between the temperature and the Johnson noise of a resistor, and a fixed point thermometer which is made of different superconductive materials whose transitions can be used as absolute temperature references. During the cool down, the dilution unit was able to bring the innermost part of the cryostat, corresponding to a thermal load of 440 kg, from 3.8 K to 10 mK in twelve hours. During this run a temperature oscillation, with a period of approximately 4 hours, was observed. It was visible only at low temperature, below 100 mK, and its amplitude was between 5 and 30 mK, depending on the cryostat configuration. Among the hypotheses, a possible explanation concerned mechanical vibrations induced by the PTs. The pulse tube cooling power is obtained by the cyclic compression and expansion of gaseous Helium. A rotating motor is used to periodically open the valve that connects the Helium compressor to the PT cold finger. The rotating motors, close to the 300 K plate, and the compressors placed on the ground floor of the hut, produce a significant vibration which was transmitted to the 300 K, and then to the inner vessels. An other unexpected behavior was found in the suspensions designed to support the internal lead shield (Lead Suspension or LS). They connect the lead shield, at 4 K, to the 300 K and need to be thermalized at the intermediate stages, to not transmit thermal power from 300 K to 4 K. The successive tests have shown that such thermalizations require a load (of the order of tens of kg, at least) to be effective.

The main goals of the Test Run 2 were to acquire the first signals from real bolometers, to have a first characterization of the detectors noise, measure the impact of the wiring on the thermalization and test the γ calibration sources displacement procedure. The CUORE wiring consists of 2600, 0.1 mm thick, wires which bring thermistor and heater signals from detectors to Front End electronics. They are connected to the Fischer Boxes on one side, and to the so called Junction Boxes on the other side. Fischer Boxes are placed on the 300 K plate and present the fischer connectors used, on the external side, to plug the cables going to the Front End. Junction Boxes, placed on 10 mk plate, are connected to the PEN strips coming from the towers. Such a large temperature gradient (from 300 K to 10 mK) causes potentially significant heat injection directly on the 10 mK stage. For this reason, every time the wires pass through a plate, they are connected to a thermalization that avoid the thermal power to be transmitted to the colder stage. In particular, because the wiring is entirely contained in the IVC - the Fischer Boxes do not communicate with the OVC - the thermalizations are placed at the 4 K, 600 mK and 50 mK stages. In this phase the wiring has been placed, checked for continuity, and it did not show appreciable impact on the temperature of the 10 mK stage. The bolometer functionality has been tested by means of a Mini-Tower of 8 crystals. As opposed to the CUORE detector towers, the Mini-Tower was suspended from the 10 mK plate, and not to the TSP; therefore larger noise, induced by the cryostat vibrations, was expected. Nevertheless, it gave the opportunity to check several important aspects of the commissioning. In this phase a base temperature of 7.3 mK was reached A leak on the dilution unit, fortunately with no ^3He loss, was found in December of 2014. This caused the interruption of the Test Run 2, and gave the opportunity to upgrade the problematic impedance valves of the condensing lines.

According to the initial plan, Run 3 should have been the last run but a delay in the production of the roman lead shields convinced the collaboration to proceed with the test by using the top lead only. The top lead shield was added to the system (see figure 3.13, left), and the Mini-Tower was moved from the 10 mK plate to the TSP. This run highlighted the necessity of minor improvements on some subsystems. Moreover it provided new data about the temperature instability issue (i.e. the four hour long temperature oscillations) and definitely proved that they are due to mechanical inputs coming from the PTs. This effect has been reduced by taking some precautions. The cardanic joints connecting the vessels were reinforced and three pneumatic pistons were added (successively replaced by metal stoppers): the pistons, connected to the MSP, horizontally push the 300 K plate to suppress the later oscillation

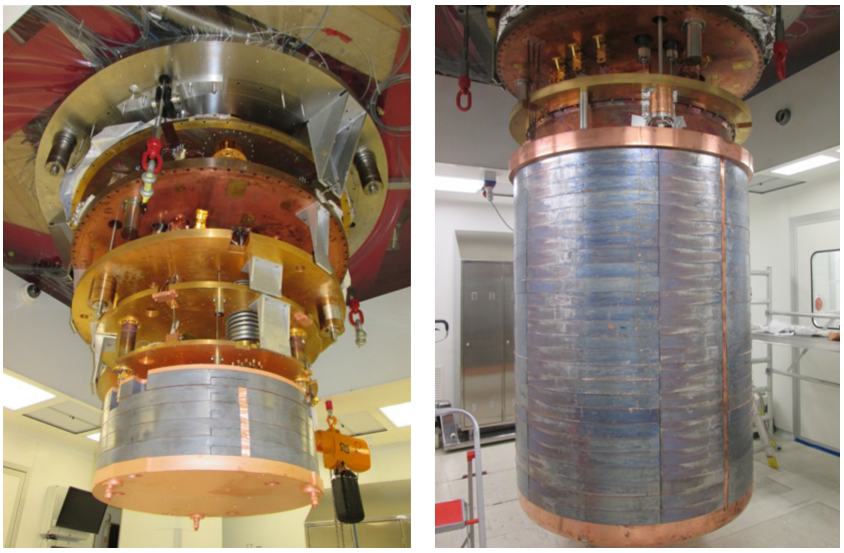

Figure 3.13: *Lead top shield (left) and roman lead lateral shield hanging from the 600 mK plate (right).*

of the cryostat. On the PT side, the phases of their five motors are remotely driven, so that their interference produces a smaller strain, in addition to this the flex lines connecting the motors and the 300 K plate are now longer than before.

A final run, the Test Run 4, was done to check lead shielding cool down. The lateral and bottom shields were added (figure 3.13, right), so the thermal load in the 4 K stage reached the impressive mass of ∼14 tonnes. Despite the large cryostat mass, the Fast Cooling System and PTs took sixteen days to cool the cryostat down to 4 K , and the base temperature of (6.3 ± 0.2) mK was reached 3.14. The run lasted, in stable conditions, about two months. In order to measure detectors energy resolution, two Thorium calibration sources were used (as described in section 3.2.4). First data from the Mini-Tower showed a very poor energy resolution. The reason was again the mechanical vibrations, damped by cleaning the MSP and the Y-beam of all the contacts with other vibration sources, such as electronic cables or flex lines. After several improvements, two (out of eight) Mini-Tower channels shown an energy resolution very close to the CUORE goal of 5 keV (FWHM) at 2527 keV when using the Optimum Filter amplitude described in section 4.1.1(see figure 3.15). The external lead shielding (∼80 tonnes) was also raised up from the ground floor to the cryostat level.

Test Run 4 officially concluded the cryostat commissioning phase. After that moment, March 2016, the installation of the other subsystems - Faraday cage, electronics, DAQ - was done, followed by the complex phase of the

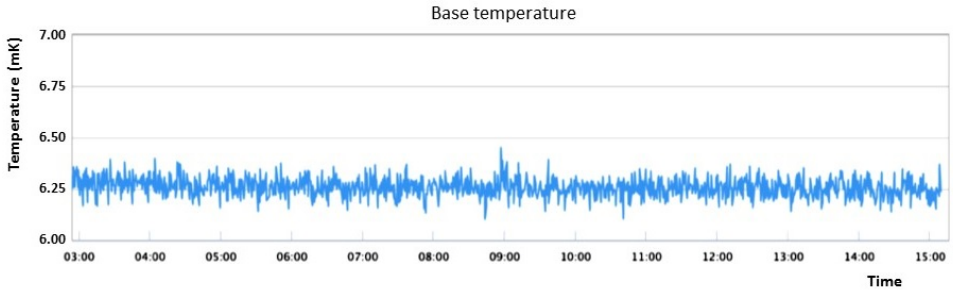

Figure 3.14: *MC plate temperature as a function of time, the mean value is 6.3±0.2 mK. The thermal stability is obtained thanks to the feedback provided by a proportional–integral–derivative controller (PID). PID is used to stabilize mixing chamber temperature, and thus the 10 mK stage temperature, by injecting power in the system by means of a Joule heater placed on the mixing chamber itself.*

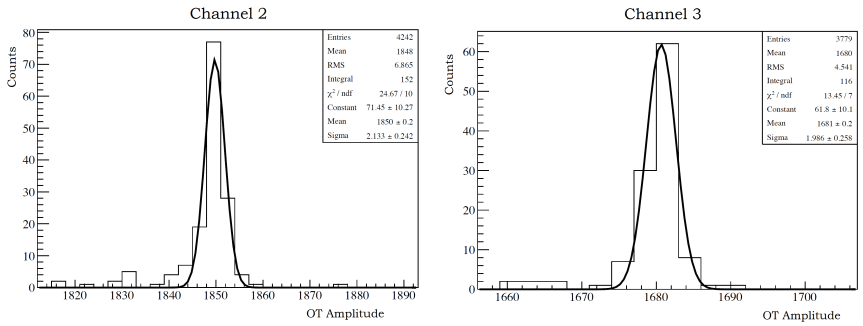

Figure 3.15: *Two Mini-Tower bolometers shown, during Test Run 4, an energy resolution of $\sigma_E/E \simeq 0.12\%$. This value corresponds to ∼7 keV resolution (FWHM) at 2527 keV which is very close to the CUORE target value of 5 keV.*

detector installation. At the time of writing, detector installation has been successfully completed and the cryostat is ready for the first science run.

3.5 CUORE-0

CUORE-0 experiment took data in Laboratori Nazionali del Gran Sasso National from March 2013 to March 2015. Its detector array is a CUORE-like tower (52 TeO_2 bolometers): support structure, crystals and detector assembly procedures were exactly the same as the ones described for CUORE. This is because CUORE-0 has been realized with the purpose, aside from the $0\nu\beta\beta$ decay search, to test the performance of the bolometers before the realization of the full scale experiment, especially in terms of energy resolution and background.

The main difference between CUORE and CUORE-0, apart from the size, is the cryostat. CUORE-0 crystat, schematically showed in figure 3.16, used liquid Helium instead of the Pulse Tubes. This means that the Inner Vacuum Chamber was immersed in a liquid Helium bath, called main bath, whose temperature is 4.2 K. The usage of liquid Helium implied two disadvantages: the cryogenic apparatus caused mechanical noise inside the cryostat and reduced the detector duty cycle (it required a He refill every two days).

In order to reduce the transmission of mechanical vibrations caused by the cryogenic apparatus, the tower was suspended to the 50 mK stage by means of a stainless-steal spring. The dilution unit mixing chamber was placed below the spring and it was thermally connected to the tower structure by two $80\times10\times0.05$ mm^3 copper foils. The tower was enclosed into copper cylinder-shape three vessels called, referring to their nominal temperature, 50 mK, 600 mK and 4 K. The 4 K vessel delimited the Inner Vacuum Chamber and it was immersed in a liquid Helium bath (called main bath). The vessel containing the liquid Helium and a last external vessel, at room temperature, delimited the Outer Vacuum Chamber (OVC). All the vessels were made of oxygen-free high-conductivity copper. Super Insulation foils, placed into the OVC, were used to reduce thermal radiation.

Three lead shields were used inside the cryostat: lateral 1.4-cm-thick and top 10-cm-thick shields were made of roman lead (4 mBq/kg [92]) while the bottom 8-cm-thick shield was made of modern lead. Outside the cryostat, two more 10-cm-thick layers of modern lead were used, their measured activity were 16 ± 4 Bq/kg and 150 ± 20 Bq/kg, for the innermost and the outermost layer respectively. Finally, the cryostat was surrounded by an acrylic glass box flushed with nitrogen to reduce radon and by a 10-cm-thick layer of

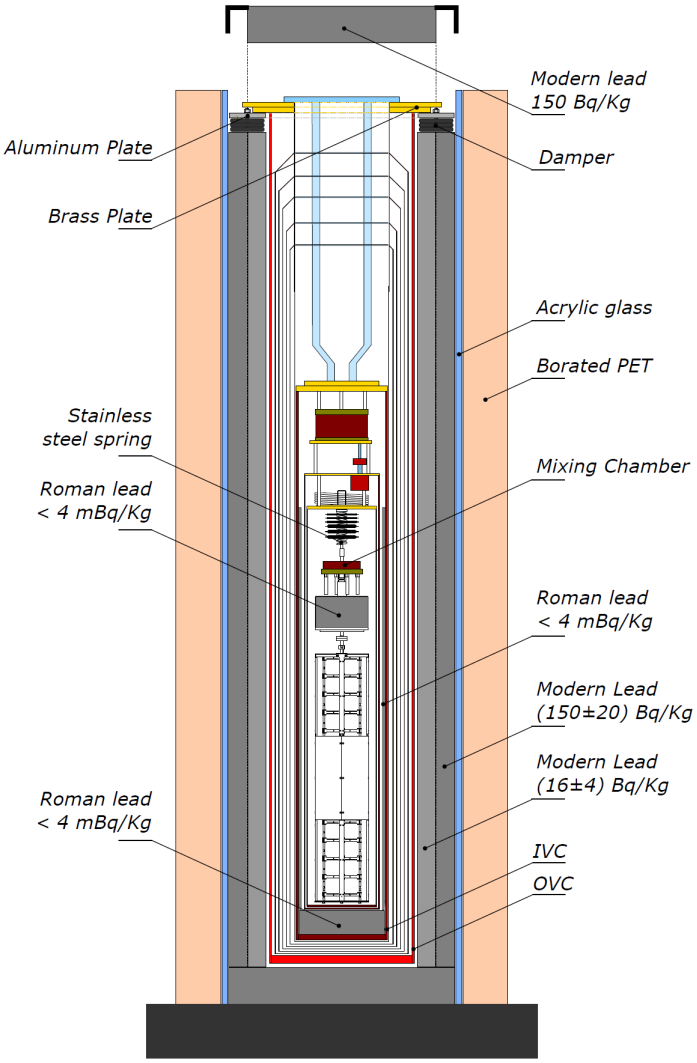

Figure 3.16: *Schematic of the CUORE-0 cryostat. Picture from [11].*

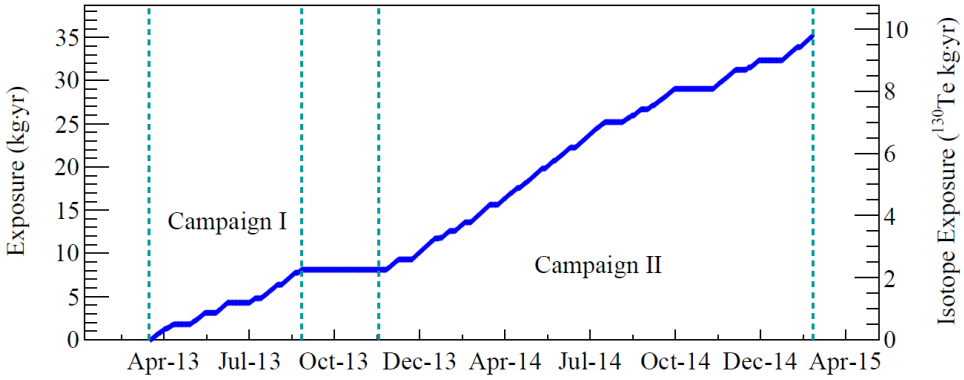

Figure 3.17: *CUORE-0 exposure as a function of time. The two vertical axes assumes different masses: TeO_2 (left) and ^{130}Te only (right). Picture from [11].*

borated polyethylene used as neutron shielding. The whole apparatus was placed into a Faraday cage to reduce electromagnetic noise.

CUORE-0 collected a total exposure of 35.2 kg·y (9.8 kg·y when considering only ^{130}T mass for $0\nu\beta\beta$ decay search) during two data taking campaigns (figure 3.17). CUORE-0 met the CUORE goal in terms of energy resolution. The average FWHM energy resolution, considering all the 51 channels, was measured on the 2615 keV ^{208}Tl line and proved to be 4.9 keV (with standard deviation of 2.9 keV)(5,42), below the 5 keV CUORE target value. The second important parameter, the background rate in the ROI, was measured to be 0.058±0.004(stat.)±0.002(syst.) counts/kg/keV/y [45]. Nevertheless, according to Monte Carlo simulations reported in [1], most of the background in the ROI was due to the external shield activity that is expected to be reduced in CUORE thanks to the better material selection and the self shielding effect of the close-pack detector array. If the CUORE background in the ROI will be dominated by α-particles from surface contamination, as expected according to simulations, then the CUORE-0 data show the background goal of 10^{-2} counts/kg/keV/y can realistically be achieved.

At the time of writing the Cuoricino and CUORE-0 combined limit $T^{0\nu}_{1/2} > 4.0\times10^{24}$ *years* at (90% C.L.) represents the most competitive limit on $0\nu\beta\beta$ decay of ^{130}Te [45].

Chapter 4

Low energy analysis

In this chapter the first level of data processing will be discussed, covering the analysis from digitized samples through to the energy spectrum (and its time information) used for the annual modulation signature search. The first part of the analysis process is very similar to the one adopted in all the standard CUORE-0 analysis, and uses the same analysis software called `Diana`.[1] An exception is represented by the Optimum Trigger, described in the first section, which is integrated in the `Diana` framework but is used in low energy analysis only.

The second part, from section 4.3, has been specifically developed for the DM analysis [14] and required dedicated tools. In the last section data selection cuts will be described and the resulting low energy CUORE-0 spectrum will be shown.

4.1 Low energy trigger

In the CUORE-0 standard analysis (as $0\nu\beta\beta$ or $2\nu\beta\beta$), the simple trigger described in section 3.3.3 is used, in which the signal amplitude is estimated as the maximum of the pulse minus the baseline value.[2] The value of the amplitude returned by this method is affected by a large uncertainty, due to the baseline noise, and cannot be used to trigger events in the region below the 100 keV. For this purpose a different trigger has been developed: it is a simple threshold trigger (i.e. it fires when the baseline exceed a given value) but it is applied on continuous data processed by the optimum filter alogorithm.

[1] `Diana` is a custom software, entirely written in C++ programming language, based on a modular structure.

[2] The baseline value and slope are evaluated, per every pulse, from the pre-trigger interval, typically 1 second long.

4.1.1 Optimum Filter

The Optimum Filter [101] maximizes the signal to noise ratio because it is matched to the signal and the noise spectra. Its transfer function, at a given frequency ω, is directly proportional to the signal-to-noise ratio measured for that ω:

$$H(\omega_k) = h\frac{s^*(\omega_k)}{N(\omega_k)}e^{-j\omega_k i_M} \tag{4.1}$$

where $s(\omega_k)$ is the discrete Fourier transform of the ideal signal s_i, i_M is the position of the maximum of s_i, $N(\omega_k)$ is the noise power spectrum and h is a normalization constant required to leave the signal amplitude unmodified

$$h = 1/\sum_k \frac{|s(\omega_k)|^2}{N(\omega_k)} \tag{4.2}$$

The power spectrum of the noise after the filter is

$$N_f(\omega_k) = h^2\frac{|s(\omega_k)|^2}{N(\omega_k)} \tag{4.3}$$

from which the resolution after the filter can be derived

$$\sigma_f^2 = \sum_k N_f(\omega_k) = h^2\sum_k \frac{|s(\omega_k)|^2}{N(\omega_k)} = h \tag{4.4}$$

The application of the Optimum Filter gives several benefits. The first effect is that the low frequency suppression makes the baseline flat and equal to zero, this is the reason why the presence of a pulse is no more recognized by looking at the derivative but simply at the absolute value of the signal. The second, more important, is that all the signal features, whose shape is different from the one of the expected signal, are suppressed. In this way the amplitude of noise fluctuations and non-physical pulses are reduced.

The OF requires the knowledge of the ideal pulse and the noise power spectrum in order to be defined. These two characteristics are channel and run dependent so, during a CUORE-0 run only the standard (derivative and noise) triggers operate. The average pulse is used as an estimation of the ideal pulse s_i. It is obtained by averaging a large set of pulses; in this way the noise fluctuations that affect the single pulse are automatically suppressed. The noise power spectrum $N(\omega_k)$ is evaluated as the average of the power spectra of the "noise windows" acquired when the noise trigger fires. To have the pure noise spectrum, only the windows that do not contain pulses are considered. When these two pieces of information are available, after a long run, the entire baseline retrieved from the continuous flow files is reprocessed. After

the filtering, the pulse presents a symmetric shape with the same height of the original pulse (figure 4.1, left) while the baseline noise, whose frequencies have low signal-to-noise ratio, is reduced (figure 4.1, right).

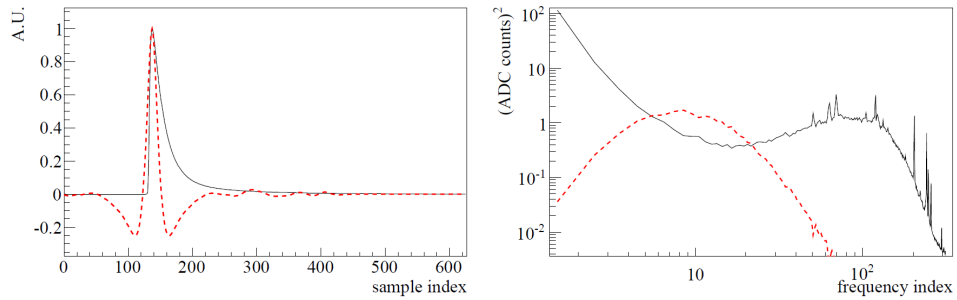

Figure 4.1: *The effects of the Optimum Filter. Left: a pulse before (solid black line) and after (dotted red line) the filtering. Right: the noise power spectrum before (solid black line) and after (dotted red line) the filtering. Figure from [12].*

4.1.2 Optimum Trigger

For computational reasons, the filtering algorithm is implemented in the frequency domain, and applied on windows 10 seconds long, with an overlap, between a window and the preceding one, of 5 seconds. In this way all the continuous data stream is analyzed.

The Optimum Trigger (OT) [12] is a threshold trigger applied to the filtered windows. The threshold is set, channel by channel, to $3\sigma_f$, where σ_f is the resolution after the filtering (equation 4.4). The OT fires when the signal exceeds the threshold and a local maximum is found within a time interval with the same length of the FWHM of the filtered average pulse. The trigger flag is not placed where the sample exceeds the threshold but is moved backward by half of the rise time of the unfiltered pulse. This is because the signal maximum is expected, by the analysis tools, to be after the trigger position. The same length of a FWHM is also used to define a veto region, after the trigger position, where the trigger can not fire again. This is to avoid to trigger twice the same pulse.

The filtered pulse presents symmetric lobes that can exceed the threshold in case of high energy pulses (see figure 4.2). Nevertheless they are not triggered if another pulse, high enough to produce side lobes, is found in the proximity.

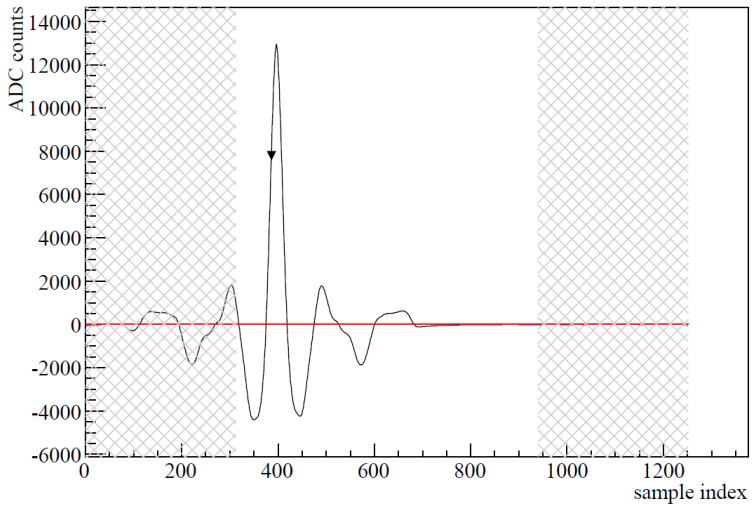

Figure 4.2: *An high energy pulse presents four symmetric lobes that exceed the threshold. The grey regions represents where the trigger cannot fire (because they are outside the window of five seconds) and the red horizontal line represents the threshold. Only the highest pulse is triggered because the others are recognized as side lobes. Figure from [13].*

4.1.3 Trigger efficiency

The efficiency of the standard, derivative, trigger was measured in CUORE-0 by means of heater pulses of few MeV. In fact, it can be evaluated as the number of triggered heater pulses over the number of fired pulses. This estimation resulted satisfactory from the $0\nu\beta\beta$ ROI down to ∼100 keV, but not in the low energy region where the efficiency goes to zero. In this case more heater pulses were produced, from few keV to ∼100 keV, to study the trigger efficiency energy dependence; this operation was performed during dedicated runs called *N-Pulsers*. Every heater pulse was tagged, in data files, by a flag automatically set by the DAQ. If the OT fired within 100 ms after that flag, the pulse was considered detected and the efficiency was evaluated, again, as the fraction of triggered pulses, with the error given by the binomial distribution:

$$\epsilon = \frac{N_{triggered}}{N_{fired}}; \qquad \sigma_\epsilon = \frac{\sqrt{N_{fired}\epsilon(1-\epsilon)}}{N_{fired}} = \sqrt{\frac{\epsilon(1-\epsilon)}{N_{fired}}} \tag{4.5}$$

N-Pulsers runs were systematically done starting from July 2013, roughly one per month. No more than one N-Pulsers run per month is needed because the energy dependence of the efficiency can be derived from the knowledge of the OF resolution σ_f. A way to understand it is to start from considering

an ideal detector with $\sigma_f = 0$: in this case all the events with energy below the threshold are not detected, while all the others are detected. This means that the efficiency is a step function, passing from 0 to 1 at E_{thr} (i.e. the energy of a pulse as high as the threshold). The finite OF resolution acts by shifting the energy of every pulse upward, or downward, with a probability described by a Gauss function with standard deviation equal to σ_f. So the probability that a pulse, with energy E_{real} below E_{thr}, is detected is given by the integral of a normalized Gauss function (describing the probability distribution of the measured energy), with mean E_{real}, from E_{thr} to $+\infty$. Similarly the probability that a pulse with $E_{real} > E_{thr}$ is not detected is given by the integral, of the same function, from $-\infty$ to E_{thr}. In conclusion, the efficiency rises from 0 to 1 as a cumulative error function, centered in E_{thr}, with standard deviation equal to σ_f:

$$\epsilon(E) = \frac{1}{2} erf\left(\frac{E - E_{thr}}{\sqrt{2}\sigma_f}\right) + \frac{1}{2} \tag{4.6}$$

A comparison between the values measured with an N-Pulsers run and the predicted cumulative error function is given in figure 4.3.

With equation 4.6, we set an efficiency threshold such that the trigger efficiency reaches the 99% (in figure 4.3 it is represented by the red vertical line).

4.1.4 Shape indicator

Given the dependence of the OF transfer function $H(\omega_k)$ on the shape of the average pulse, pulses with different shape (such as non-physical events induced by electronic noise, mechanical vibrations etc...) are suppressed in amplitude and, more importantly, their filtered shape differs from the expected one. This feature can be used to define a shape indicator (SI) called χ^2_{OT} based on which non-physical events can be rejected. The SI is not directly used in the trigger algorithm, meaning that non-physical pulses are triggered anyhow, but it is used to define a quality cut during the analysis. In practice the filtered pulse is fit with a cubic spline, which reproduces the filtered average pulse, and the value of the reduced chi square χ^2/ndf is used as SI.

The fit range L is four times the FWHM of the filtered pulse, and the free parameters of the fit are the signal amplitude and the position of the maximum. The amplitude can vary in the range $[A, A/(1-\delta)]$ where A is the amplitude of the pulse (simply the height of the filtered pulse) and $(1-\delta)$ represents the highest amplitude suppression due to digitization and

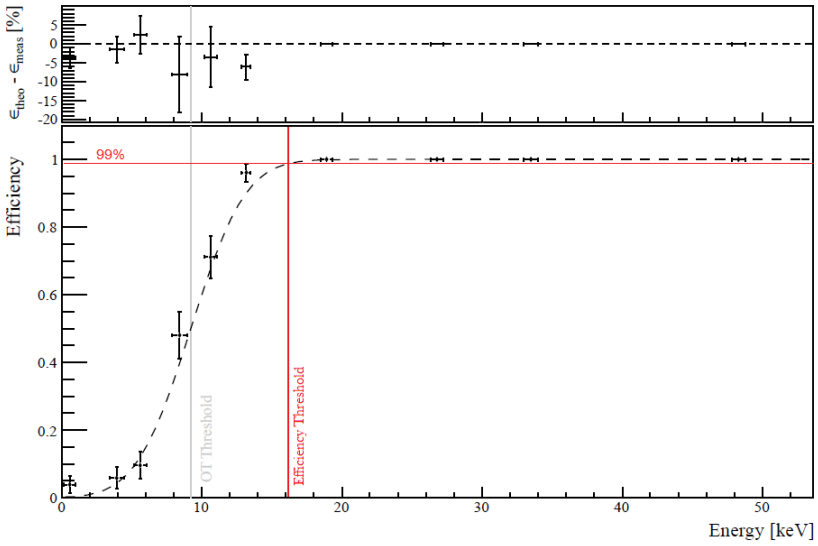

Figure 4.3: *Using heater pulses, the efficiency of the OT was measured as the number of detected events over the number of fired ones. Every data point in the plot represents the efficiency evaluated with pulses of a given energy. The measured values are in good agreement with the error function which is not the result of a fit but is based on a priori information. The vertical grey line indicates the energy corresponding to the trigger threshold, where 50% efficiency is expected, while the red one represents the energy at wich the trigger reaches 99% of efficiency. The upper part of the figure shows the residuals between the data points and the error function. Figure from [13].*

is close to one. The value of δ is estimated from $(A_m - A_{m+1})/A_m$, where A_m (already denoted as A) is the amplitude of the maximum and A_{m+1} is the sample right after the maximum. The second fit parameter, that is the position of the maximum, can vary within two samples; this is the highest shift induced by the digitization.

The shape indicator is computed as:

$$\chi^2_{OT} = \frac{1}{L-2} \sum_{i=0}^{L-1} \frac{(s_i^f - f_i)^2}{\sigma_L^2} \tag{4.7}$$

where s_i^f is the ith sample of the filtered pulse, f_i is the corresponding value of the fit function and σ_L is the amount of noise expected in a window of L samples (a more detailed description can be found in [12]).

It must be noted that, after the filtering, the sample errors are correlated and this affects the probability distribution of χ^2_{OT}. This means that χ^2_{OT} does not follow the χ^2 distribution: the mean value is still 1 but its variance

is not $2/(L\text{-}2)$.

An example of distribution of the SI, as a function of the energy, is given in figure 4.7.

4.2 Stabilization

As stated in section 3.1.1, the amplitude of a pulse depends not only on the deposited energy but also on the temperature of the bolometer. This second dependency, if not considered, would fatally deteriorate the detector energy resolution. To evaluate this second dependency, a kind of precalibration, called stabilization, is required. The pulses, produced by means of the Joule heaters, corresponding to the same energy are grouped. In first approximation, the measured pulse amplitude A is proportional to the deposited energy E and to the bolometer gain $G(V_B)$, where the last depends on the baseline V_B.

$$A(E, V_B) = E \cdot G(V_B) \tag{4.8}$$

It must be noted that we implicitly assume that the gain is independent of the energy released. Therefore, even if the pulses used by this procedure have energies above 100 keV (up to few MeV), the same correction can be applied to physical pulses at lower energies.

The pulse amplitude is stabilized by introducing a correction factor

$$A_{stab}(E) = A(E, V_B) \cdot f(V_B) = E \cdot G(V_B) \cdot f(V_B) \tag{4.9}$$

from which

$$f(V_B) = A_{stab}(E_0)/A(E_0, V_B) = 5000\ mV/A(E_0, V_B) \tag{4.10}$$

where $A_{stab} = 5000\ mV$ is an arbitrary value for a given energy E_0.

Figure 4.4 shows the distribution of the amplitude of a set of pulses (of the same energy) as a function of the baseline value, before the stabilization (left plot). $A(E_0, V_B)$ is extrapolated with a linear fit (represented by the blue line) and used to correct the amplitude of all the pulses. The right plot shows the distribution of the pulse amplitudes after the stabilization

4.3 Calibration check

In CUORE-0 a set of calibration runs was performed roughly once per month; this procedure typically lasted three days. The group of background runs (standard runs with no sources) between two consecutive calibrations is called

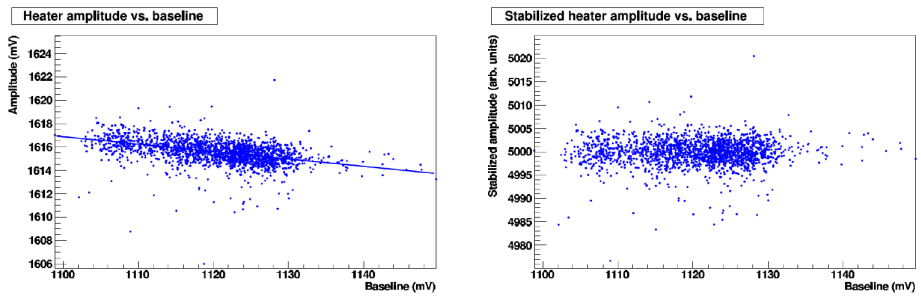

Figure 4.4: *The stabilization procedure is used to remove the dependence of the pulse amplitude on the baseline. Every point in the scatter plots represents a pulse, induced by the heater; all the pulses have the same energy and occurred on the same channel. Before the stabilization (left plot) the amplitude decreases for higher values of the baseline, indeed higher values of the baseline correspond to higher sensor temperature and thus lower NTD sensitivity. After the procedure (right plot) the distribution is almost flat. In this case the reference value is* $A_{stab} = 5000\ mV$.

dataset.

The calibrations were performed by means of two low-activity ^{232}Th sources: two thoriated tungsten wires placed just outside the cryostat, but inside the external lead shielding, during the calibration period. The ^{232}Th sources produce visible γ-peaks from 511 keV to 2615 keV (see figure 4.5). The calibration function $E(\Delta V)$ is a second-order polynomial with zero intercept. Because of the internal shielding, no peaks below 511 keV are visible and a direct calibration in the low energy region can not be obtained. However the atomic de-excitation of Te, which is a enhanced by the exposure to the calibration sources, produces eight lines that, because of the energy resolution, appear as two bumps around 27 keV and 31 keV (see table 4.1). Their intensities are so small that no peaks can be seen in the spectrum from a single channel and a single dataset, but a sum over the datasets is required to increase the statistics. In order to not pollute the sum spectrum with outlier datasets, a dataset selection has been performed by means of the heater pulse events at ∼15 keV. The peaks in the heater pulse amplitude spectrum, from a specific channel-dataset, are fitted with Gaussian functions in order to extract their mean energy ($E_{ch,DS}$) and a standard deviation ($\sigma_{ch,DS}$). Then all the values, from different datasets of the same channel, are grouped and the global mean energy E_{ch} is computed. Finally the datasets for which $|E_{ch,DS} - E_{ch}| > \sigma_{ch,DS} + 1\ keV$ are excluded for that channel. This caused the exclusion of 15 channel-dataset pairs from the analysis presented in this

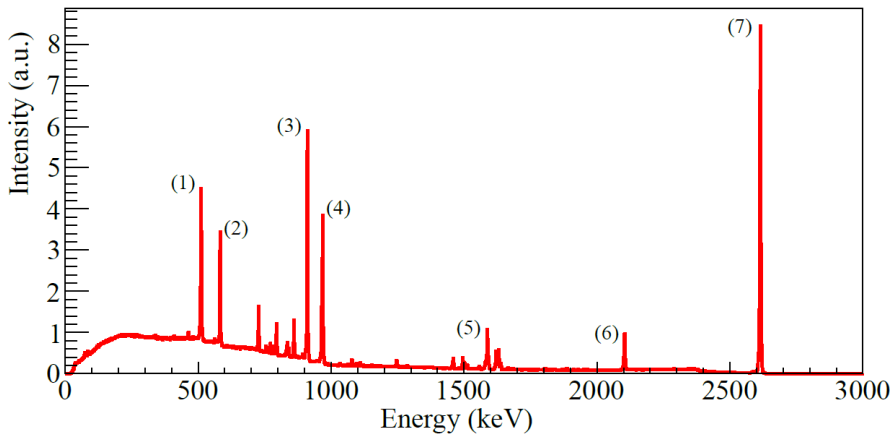

Figure 4.5: *CUORE-0 calibration spectrum. The peaks corresponding to γ-lines from nuclei of ^{232}Th decay chain are tagged: (1) 511 keV (electron-positron annihilation), (2) 583 keV (^{208}Tl), (3) 911 keV (^{228}Ac), (4) 965 keV and 969 keV (^{228}Ac), (5) 1588 keV (^{228}Ac), (6) 2104 keV (^{208}Tl single-escape peak), (7) 2615 keV (^{208}Tl). Figure from [11].*

work.[3] After this cut ∼480 channel-datased pairs remained.

The spectra from the remaining datasets are summed for each channel. At the end the eight Te X-ray-induced peaks were visible in the multiplicity-2-spectra (M2, explained below) of 22 channels only (the 22 "good channels").

What multiplicity means is here explained. When a bolometer registers a pulse, at time t_1, a second pulse is searched, in a different crystal, within $t_1 + \Delta t$ where Δt is a given time length (in this case 100 ms). If a second

[3]They are ds2079, ds2100 and ds2139 for channel 5; ds2124, ds2130 and ds3139 for channel 15; ds2124 for channel 22; ds2079, ds2097 and ds2124 for channel 27; ds2130 for channels 29, 34 and 37; ds2079 and ds2085 for channel 43. Compare with table 4.2

Line	Energy (keV)	Intensity (%)
Kα1	27.472	47.1
Kα2	27.202	25.3
Kα3	26.875	0.00202
Kβ1	30.995	8.19
Kβ2	31.704	2.37
Kβ3	30.944	4.25
Kβ4	31.774	0.363
Kβ5	31.237	0.075

Table 4.1: *The main X-ray emission lines of Tellurium are reported with the corresponding energies and intensities. Data from [16].*

pulse is found, at time $t_2 < t_1 + \Delta t$, a third is searched within $t_2 + \Delta t$ and so on. At the end, the multiplicity is given by the number of channels that register a pulse in "time coincidence" (note that the time distance between two non-consecutive pulses can be greater than Δt).

In this context M2 events are used to select the cases in which the X-ray is emitted by a crystal, that has been excited by an impinging particle, and absorbed by a second crystal. In this way the number of background event is reduced.

The peaks are fitted in both calibration runs and background runs M2 spectra, obtained by summing the spectra from the selected datasets of the 22 good channels (see figure 4.6). The fit function is the sum of a first-order

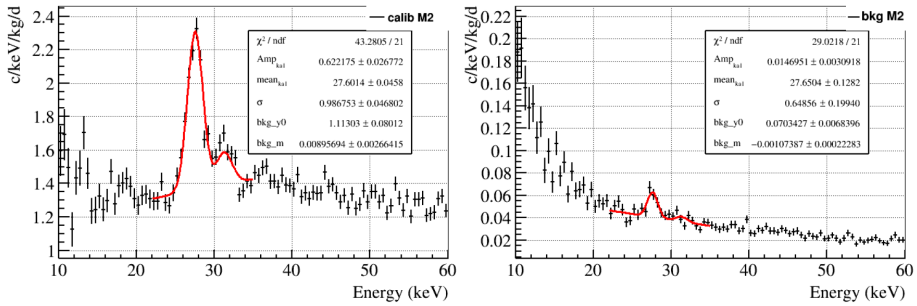

Figure 4.6: *Multiplicity 2 spectra, for the 22 channels that show the 27 keV peak, obtained by summing all calibration runs (left plot) and all background runs (right plot). The fit function is a first-order polynomial summed to two Gauss functions. Picture from [14].*

polynomial, accounting for the background, and 8 Gaussian functions, representing the gamma peaks. The standard deviation is the same for all the Gaussian functions while their means and the amplitudes are not independent, but constrained by the position and the intensity of the Kα1 main line (see table 4.1). The calibration uncertainty, defined as the difference between the energy of the Kα1 line returned by a fit and its nominal energy, was found to be (0.13 ± 0.05) keV for calibration runs and (0.18 ± 0.13) keV from background runs.

This check can not be done for the channels different from the 22 good channels. The spectrum of those bad channels has been compared to the one from the 22 good channels by fitting, with a Landau function, the ∼37 keV bump[4] and by comparing the mean values. The difference of the positions of the two fit function is (0.03±0.06) keV. The reported error also includes

[4]The 37 keV bump is a well visible broad peak that can be seen in all CUORE-0 channels as well as in the CUORE-0 M1 spectrum (figure 4.11).

the systematic effects, such as the fit method, the fit interval and the bin size. Note that the discrepancy of 0.03 keV is well below the calibration uncertainty obtained by the Te X-ray peaks.

It must be noticed that the calibration measurements are performed by using γ-ray peaks, which cause electron recoil (ER), while WIMPs are expected to produce nuclear recoils (NR). In principle the bolometer responses to NR and ER could differ. In other words the quenching factor, defined as the measured energy of NR over the measured energy of ER assuming an equal amount of energy deposited in the bolometer, could be different from one.

The quenching factor for TeO_2 bolometers has been measured [102] by using the daughter nuclei of the alpha decays from ^{224}Ra, ^{220}Rn, ^{216}Po, ^{212}Po, and ^{212}Bi at the energy range between 100 and 170 keV. The authors of that work report a quenching factor relative to electrons of $1.025 \pm 0.01_{stat} \pm 0.02_{sys}$ for recoiling nuclei. A similar study has been repeated in CUORE-0 [103] by using the daughter nuclei of the alpha decay from ^{224}Ra, ^{222}Rn, ^{218}Po and ^{210}Po at the energy between 100 and 112 keV. In this case the quenching factor resulted slightly smaller than 1 (from 0.93 to 0.99 depending on the nucleus) and a difference in the quenching factor of M1 and M2 events has been observed. This last aspect could be due to the fact that M2 events are due to surface interactions, while M1 events are more likely bulk interactions. The largest deviation from unity, measured from the alpha peak of ^{210}Po, was equal to 7%.

4.4 Event selection

In this section the data selection will be presented. The cuts used for data selection can be divided in time based criteria and in single event criteria. Time based criteria are used to exclude entirely a portion of data, for example the so-called *BadIntervals* in which the detectors showed a bad behavior. The event based cuts are necessary because not all the triggered events can be used in the analysis: firstly, as already stated, not all triggered pulses represent particle events, and secondly not all the physical events can be ascribed to WIMP-induced nuclear recoils.

4.4.1 Time based cuts

Not all the data acquired with CUORE-0 have been used in this work because of their non-standard characteristics. In some cases the criteria leads to the exclusion of the data from a specific channel and from a specific run (I'll refer

to it as channel-run pair) or from a specific dataset (channel-dataset pair). The adopted criteria are:

1. Datasets that do not contain N-pulses measurements have been removed. N-pulses measurements, used to check the OT efficiency, started in a systematic way on July 2013 (at the end of the first CUORE-0 campaign), in correspondence with a more stable cryogenic operation of the detector. This criterion selected eleven datasets.[5]

2. Reject the runs that present abnormally high trigger rate. This cut caused the exclusion of the last five runs of ds2109 that probably started too early after the main bath He refill.

3. Reject channel-dataset pairs in which the reconstructed energy of the low-energy heater pulses is too far from the average. This because the heater pulses are used to identify a possible miscalibration. Such procedure has been described in section 4.3.

4. Reject channel-dataset pairs that present less than eleven events in the energy region 35-50 keV. This because the χ^2_{cut} efficiency (see section 4.4.2) is evaluated in that energy interval.

5. Reject channel-run pairs with noisy baseline. In particular the RMS of the baseline samples is evaluated for every channel and run. Its distribution, for a given channel, is analyzed and the runs that present a value above the average + 2σ, are excluded. This cut caused the loss of about 5% of the total number of channel-run pairs.[6]

6. Reject the so-called *BadIntervals*, that are small periods (typically they are few-hours-long) during which the data quality is compromised for whatever reason (seismic events, activities in the experimental hall, cryogenic apparatus issues...).

4.4.2 Event based cuts

Once the time intervals of data to be used have been defined, an event by event selection is performed to reduce non-physical event contamination. In particular the low-energy range (up to tens of keV) is the one that collects the biggest portion of non-physical signals. They are due to tower vibrations, electronic noise, baseline instabilities or particle events that take place

[5] Selected datasets are: ds2079, ds2085, ds2088, ds2091, ds2097, ds2100, ds2103, ds2109, ds2124, ds2130 and ds2139

[6] The rejected statistics is approximately 14% for ds2124, 11% for ds2109, 9.5% for ds2130, 4% for ds2079 and ds2088 and less than 1% for the remaining datasets.

directly in the NTD (that appear as fast signals, spikes). These kinds of pulses can exceed the OT threshold and be triggered, even if their shape is different from the expected one. The selection is performed by taking advantage of the shape indicator χ^2_{OT} described in section 4.1.4. It can be used to quantify the goodness of the shape of every pulse.

In figure 4.7 two χ^2_{OT} -vs-energy scatter plots are shown, corresponding to ds2097 for channel 6 (as example of a good channel, top plot) and ds2085 for channel 13 (as example of noisy channel, bottom plot). In both plots two populations of data are clearly visible: the horizontal band presents smaller values of χ^2_{OT} and is composed by physical events while the oblique one is made of noise events.

Signal events are selected by the application of an energy-independent cut, rejecting all the events for which χ^2_{OT} is greater than a given value χ^2_{cut}. The value of χ^2_{cut} is independently evaluated for every channel-dataset pair and a given efficiency of acceptance of signal events.

The definition of the value of χ^2_{cut} starts from the assumption that, above a certain energy, the two events populations, signal and noise, can be divided by a certain reference value of χ^2_{OT}. The adopted reference value is 10; this means that, looking for example at the scatter plot in figure 4.7 (top), we can assume that in the energy region between 10 keV and 100 keV all the events at $\chi^2_{OT} < 10$ are signals and that all events at $\chi^2_{OT} > 10$ are noise.

At this point a value for the cut signal acceptance (or cut efficiency) is chosen: it is defined as the nominal probability for a physical signal event to pass the cut, while noise events are, in principle, strongly rejected. In this analysis two values will be adopted: 90% and 50% that define the two values $\chi^2_{90\%}$ and $\chi^2_{50\%}$ respectively.

Then a reference energy region where to evaluate the cut is chosen. In doing this the energy dependence of the χ^2_{OT} parameter must be considered. Such dependence has been highlighted by looking at calibration data - where the signal band is more populated with respect to background data - and clearly appeared channel- and dataset-dependent. For example in figure 4.7 the energy-dependent $\chi^2_{90\%}$ ($\chi^2_{50\%}$) is represented by the red (orange) curve and is more pronounced for channel 6 than for channel 13. A more direct channel by channel characterization of the cut energy dependency is not possible because of the low statistics in background runs.

This aspect leads to the decision to use the 35-50 keV interval for the definition of the cut values, which is close to the region of interest (ROI) for DM studies. Indeed, considering that the recoil energy spectrum induced by WIMP is expected to exponentially decay with energy (see figures 2.2 and 2.4), the ROI can be limited to 0-35 keV without a significant sensitivity loss.

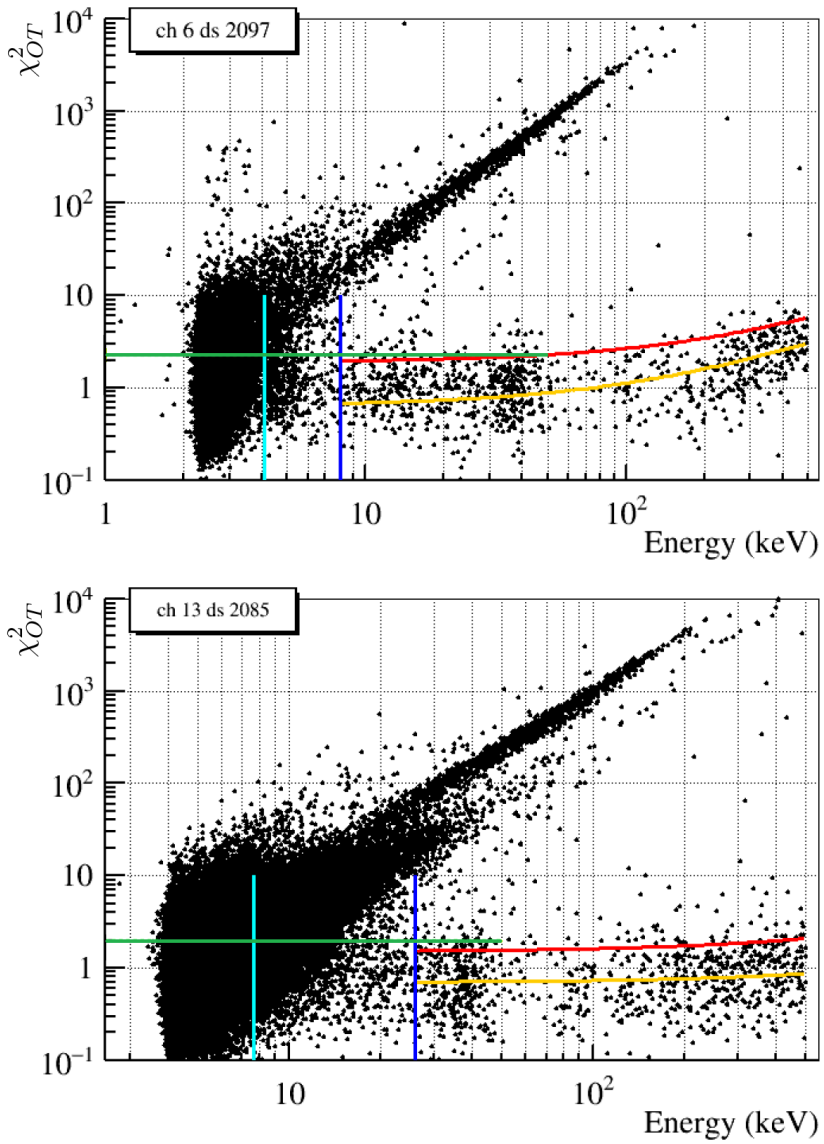

Figure 4.7: *Two examples of χ^2_{OT} distribution as a function of energy. Physical events are distributed in a horizontal band around χ^2_{OT} =1 (i.e. the expected mean value). Non-physical events form an oblique band. The red (orange) line corresponds to $\chi^2_{90\%}$ ($\chi^2_{50\%}$) calculated on calibration runs. The green dotted line represents the energy-independent $\chi^2_{90\%}$ calculated on background runs in the 35-50 keV region. Cyan and Blue lines are the trigger and analysis thresholds respectively. Figure from [14].*

At the beginning the region between 80 and 180 keV was used in place of the 35-50 keV region. The noise acceptance in the ROI was estimated by comparing the two spectra obtained by $\chi^2_{90\%}$ and $\chi^2_{50\%}$. In practice the two spectra were corrected by the corresponding efficiencies (dividing the bin content by 0.9 and 0.5 respectively) and their difference was computed. This procedure is based on the fact that the noise contamination in the ROI, if any, would affect the spectrum obtained with $\chi^2_{90\%}$ more than the one obtained with $\chi^2_{50\%}$, because the second cut has a stronger noise rejection capability. In other words, at low energies where the noise contributes, the number of noise events in the band $\chi^2_{50\%} < \chi^2_{OT} < \chi^2_{90\%}$ is higher than in the band $0 < \chi^2_{OT} < \chi^2_{50\%}$, then the 90% acceptance spectrum is expected to be higher than the other one. Figure 4.8 shows the difference between the two efficiency-corrected spectra: it confirms that the two spectra are compatible in the 80-180 keV region, as expected since it is the region where the cut values are defined. More in general the difference between the two spectra shows a trend that can be ascribed to the energy dependence of the cut efficiency and is a good reason to use the 35-50 keV region which is just above the ROI. The noise leakage is visible below the minimum, around 40 keV, where the 90% acceptance spectrum overestimates the signal events. Another good reason for having changed the interval from where to extract the cut values is that the uncertainty of the acceptance of χ^2_{cut} decreases as the number of signal events increases, and the 35-50 keV presents more signal events than 80-180 keV interval. The uncertainty on the χ^2_{OT} cut signal acceptance has been evaluated, for every channel-dataset pair, with the Agresti-Coull method [104]. The channel-dataset pairs that present a very low statistics ($N < 11$) in 35-50 keV interval are rejected (see section 4.4.1).

4.4.3 Analysis threshold

The comparison between the spectra obtained with the different cuts $\chi^2_{50\%}$ and $\chi^2_{90\%}$ (figure 4.8) shows that non-physical events contribute to the rate even above the efficiency threshold (the efficiency threshold is the energy at which the OT reaches the 99% efficiency; events below this threshold are never considered). Even if this does not demonstrate a noise leakage in the more conservative spectrum ($\chi^2_{OT} < \chi^2_{50\%}$), a new channel-dataset pair-dependent threshold, higher than the efficiency threshold, has been introduced in order to exclude the energy region where the noise is still present.

The procedure to find the new threshold, called analysis threshold, is illustrated in figure 4.9. It is based on the direct comparison of the χ^2_{OT} distribution (from 0 to 10) obtained for an energy-slice in the ROI, the *sample distribution*, with the same distribution in the reference region 35-50 keV,

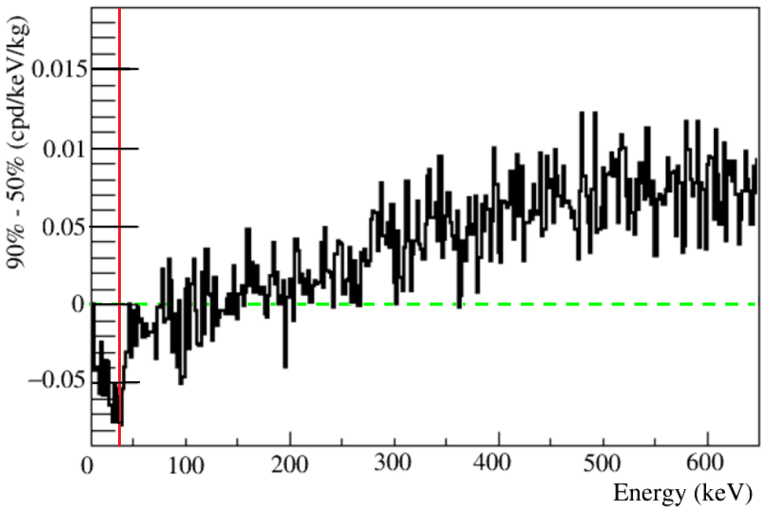

Figure 4.8: *Difference between the spectra calculated by applying* $\chi^2_{90\%}$ *and* $\chi^2_{50\%}$*. In this case the cut values have been defined in the region 80-180 keV, where the difference here shown is effectively compatible with zero. Below and above such energy interval the two spectra are not compatible. The positive trend that affects all the energies is due to the energy dependence of the cut efficiencies. The opposite behaviour below 40 keV is probably due to the noise leakage in the specrum obtained by applying the* $\chi^2_{90\%}$ *cut. Figure from [14].*

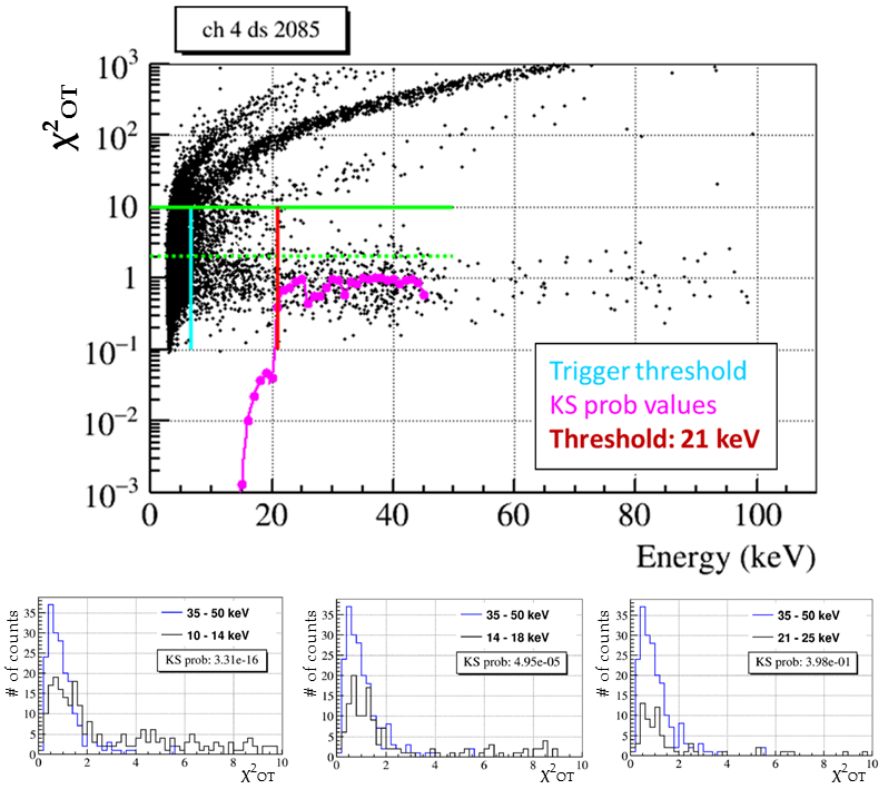

Figure 4.9: *Calculation of the analysis threshold for channel 4 and dataset 2085. The green solid line highlights the bound χ^2_{OT} =10; events above that value are totally ignored. The green dotted line represents the $\chi^2_{90\%}$ value. Starting from the trigger threshold (cyan vertical line), the χ^2_{OT} distribution in 4 keV wide energy slices is compared with the same distribution in the 35-50 keV region. Kolmogorov-Smirnov probabilities are represented by the pink dots. The 21-25 keV slice (bottom right panel) is the lowest one that gives a probability larger than 0.1: the analysis threshold is therefore set to 21 keV. Figure from [14].*

the *reference distribution*. Some examples of distributions are shown is figure 4.9 (bottom plots) where the *sample distribution* is represented by the black histograms and the *reference distribution* is represented by the blue histograms.

Assuming that the noise in the reference region is negligible below χ^2_{OT} = 10 (I will come back on this point), the *reference distribution* is a good estimation of the signal continuous distribution. On the contrary, moving to lower energies, the noise band encroaches upon the $\chi^2_{OT} < 10$ region and contaminates the *sample distribution*. The analysis threshold is defined as the lowest energy at which the χ^2_{OT} distribution, from 0 to 10, is "similar" to the one shown in the reference region. The "similarity" of the two distributions is measured by means of the two-samples Kolmogorov-Smirnov test. In the two-samples Kolmogorov-Smirnov test (KS test) the null hypothesis states that all the data come from the same continuous distribution (in this case it is the distribution of the signal band estimated with the *reference distribution*) while the alternative hypothesis is that the data come from two different continuous distribution. Quantitatively the p-value of the Kolmogorov-Smirnov variable is used: it is the probability of observing a test statistic more extreme than the observed value under the null hypothesis. p=1 corresponds therefore to the null hypothesis while p=0 corresponds to the extreme case in which the two distributions are completely different.

Per every channel-dataset pair the following procedure is used:

1. All the events in the 35-50 keV region, with $\chi^2_{OT} < 10$, are selected and their χ^2_{OT} distribution is used as reference sample, under the assumption that the noise contribution is negligible.

2. An analogue distribution is produced by considering the events, with $\chi^2_{OT} < 10$, in an energy slice 4 keV wide, below the 35-50 keV region.

3. The KS test is used to estimate the p-value.

4. If the KS probability is grater than 0.1 (i.e. the two distribution are similar), steps 2. and 3. are repeated by shifting the energy-slice by one keV to lower energies. If the KS probability is smaller than 0.1 the *sample distribution* is considered contaminated by noise events and the analysis threshold is set to the lowest bound of the considered slice + 1 keV.

The method is not adequate when there is noise in the reference region. These cases are rejected by excluding the channel-datasets pair in which we found $\chi^2_{90\%} > 6$. This cut rejects 42 channel-dataset pairs, most of them

corresponding to four noisy channels.[7] The values of the analysis threshold, for all channel-dataset pairs, are reported in table 4.2.

In the upper plot of figure 4.10 the total background spectrum (all channels and datasets) is shown, both for 90% (blue) and 50% (black) cut efficiency, after considering the analysis thresholds. The difference between the two spectra is plotted in the lower panel in blue. All the values are compatible with zero within one sigma, while the same difference, not considering the analysis thresholds but only the efficiency thresholds, is superimposed in red and shows significant deviations from zero. The discrepancy of the two spectra, when not considering the analysis threshold, is a clear indication that there is a noise leakage in the region between the trigger and the analysis threshold. This hypothesis is in good agreement with the fact that the 90% efficiency spectrum shows a rate higher than one shown by the 50% efficiency spectrum. Moreover such difference decreases as the energy increases, as expected.

4.4.4 Anticoincidence cut

Finally the anticoincidence cut is applied in order to reduce background, by rejecting the events in which a simultaneous energy deposition takes place in more than one crystal, because they are not likely produced by DM. According to the convention introduced in section 4.3, the selected events are called multiplicity 1 (M1) events. In the evaluation of the multiplicity of a certain event, only the pulses above the analysis threshold are considered, in order to be insensitive to the noise rate that could artificially increase the multiplicity because of the random coincidence.

The signal acceptance of the anticoincidence, due to random coincidences, has been evaluated by means of the 2615 keV Tl peak and resulted to be 0.992 [105].

4.4.5 Background spectrum

The left plot of figure 4.11 shows three CUORE-0 low energy spectra obtained by applying different coincidence cut and all the other cuts: all the multiplicities in black, M1 in red and M2 in blue. The right plot shows the exposure, according to the analysis thresholds, as a function of energy. The most peculiar feature of the spectra are the "bumps" at 30 and 40 keV, absent in M2 spectrum but clearly visible in M1 spectrum. The source of such events is still not clear, they could come from the ^{210}Pb β-decay that produces an

[7] Those channels are 22, 27, 35 and 52

channel	2079	2085	2088	2091	2097	2100	2103	2109	2124	2130	2139
2	-	15	15	32	13	12	13	12	13	13	-
3	14	12	11	14	13	21	10	25	10	14	20
4	23	21	24	19	19	21	10	23	20	11	8
5	-	30	-	32	32	-	33	32	31	33	-
6	10	10	8	11	8	16	19	11	9	15	-
7	11	11	12	13	13	17	14	13	12	24	15
8	-	24	23	23	23	28	24	24	24	24	-
9	17	23	24	17	18	12	20	18	21	21	26
11	27	22	25	24	30	31	28	27	22	25	23
12	-	17	16	23	18	18	16	16	13	24	-
13	27	26	29	31	30	27	28	32	-	30	30
14	18	14	18	17	31	15	20	15	16	16	14
15	25	28	-	28	30	29	32	30	-	-	-
16	20	22	23	22	19	22	20	24	26	26	-
17	13	21	18	11	11	16	15	12	23	15	9
18	11	27	9	9	10	18	13	12	9	10	-
19	11	10	10	9	9	12	11	10	10	11	9
20	-	26	26	26	29	30	29	30	26	11	-
21	13	11	13	12	13	12	14	15	12	17	12
22	-	-	-	-	-	-	-	-	-	32	-
23	17	17	25	25	23	22	23	28	23	32	30
24	-	17	16	16	15	17	18	16	26	21	-
25	17	21	22	19	19	21	20	27	22	32	18
26	-	27	33	30	33	30	29	31	30	32	-
28	15	13	20	17	15	14	15	14	17	13	12
29	30	28	-	25	31	32	31	29	32	-	32
30	28	28	25	25	23	23	24	21	26	25	21
31	27	12	17	14	11	10	12	14	19	17	19
32	-	11	13	11	10	10	9	10	10	13	15
33	27	30	28	32	27	28	25	30	28	24	29
34	-	20	23	23	19	25	21	19	22	-	21
35	-	32	-	-	-	-	-	-	33	-	33
36	-	14	21	23	13	12	17	15	28	28	-
37	27	28	32	29	28	26	28	30	28	-	-
38	29	19	32	26	22	27	27	26	19	34	-
39	32	28	29	33	28	33	-	33	31	-	31
40	26	17	19	16	15	17	14	30	26	21	15
41	25	28	26	23	26	24	28	24	23	22	18
42	14	9	19	14	17	10	12	11	-	-	-
43	-	-	24	22	23	22	21	21	-	23	22
44	15	12	14	10	28	9	11	10	32	30	10
45	19	15	15	10	19	13	16	14	13	26	13
46	-	14	9	10	9	11	22	10	20	12	20
47	19	17	18	18	32	20	18	18	31	22	24
48	-	20	26	18	-	19	24	25	28	-	-
50	-	22	20	20	19	22	31	22	27	-	-
51	30	28	24	-	20	23	27	27	31	33	20
52	-	32	31	-	31	33	-	-	33	-	-

Table 4.2: *Analysis thresholds obtained from Kolmogorov-Smirnov, for all channel-dataset pairs, expressed in keV.*

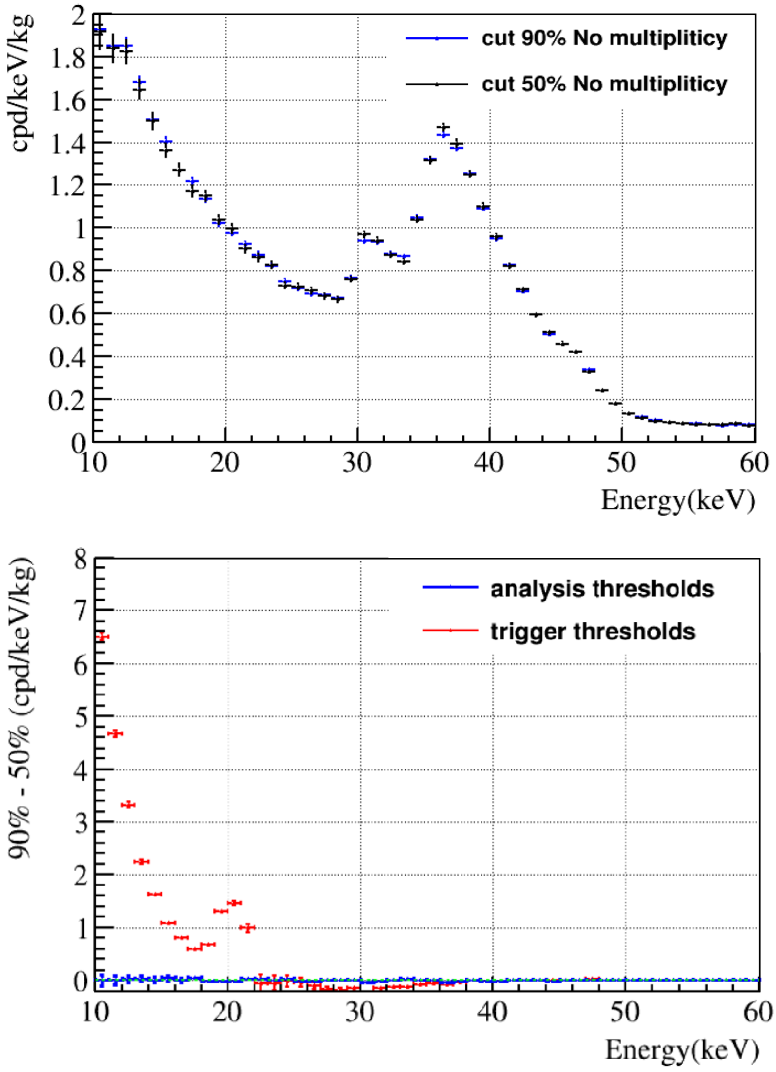

Figure 4.10: *Effects of the analysis thresholds on the low energy spectrum. Top panel: CUORE-0 spectrum considering all channels and datasets for 90% (blue) and 50% (black) signal acceptance ($\chi^2_{90\%}$ and $\chi^2_{50\%}$ evaluated in the 35-50 keV region). Bottom panel: in blue, difference between the two spectra of the top panel; in red, the same difference not considering the analysis thresholds. In this last case the difference of the two spectra reaches 6.5 cpd/keV/kg, while in the former case all the values are compatible with zero within one sigma. Figure from [14].*

excited state of ^{210}Bi with a branching ratio of 80%. ^{210}Bi de-excitation happens through the emission of a 46 keV γ that can cause internal conversion, with electron emission at 30.2, 42.5 and 45.6 keV. Even if the low statistics avoids a clear confirmation of this hypothesis, a ^{210}Pb background has been considered in the modulation analysis (see section 5.4.1).

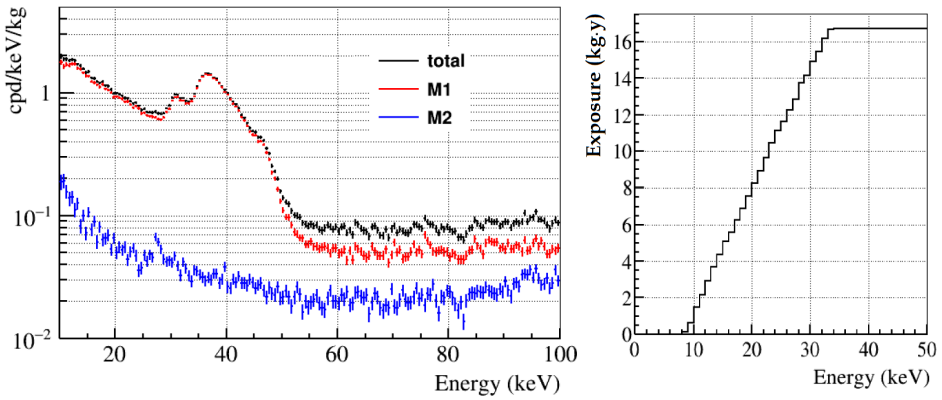

Figure 4.11: *CUORE-0 low energy spectrum (left) and CUORE-0 exposure (right), after the application of the cuts and considering the analysis thresholds. Figure from [14].*

Chapter 5

Annual modulation analysis

CUORE-0 data used for annual modulation analysis, after the selection, cover a period of about 15 months, from November 2013 to March 2015, and are distributed in 11 datasets (i.e. the elapsed period between two consecutive calibrations). The list of datasets (DS) is given in table 5.1. The main purpose of this analysis is to check if CUORE-0 data, according to equation 2.21, contain a modulation signal and to study how much the observed modulation can be attributed to DM-induced nuclear recoils. This operation is performed by dividing data in several energy slices in order to obtain an energy dependent modulation amplitude (as in figure 2.4). The energy slices, where not specified, are 2 keV wide. For every energy range, data are grouped into several time bins: the systematic effects of time binning are discussed in section 5.4.2. Unless otherwise stated, the time axis will be expressed in days, since January 1^{st} 2013, so that the analyzed period starts at ∼330 days and stops at ∼790 days. In this way a set of histograms is obtained, one per each possible combination of channel and energy bin; these histograms will be called original-total-counts and contain the number of events detected in a specific bolometer, in a specific energy range, over time. In this case only the events that pass all the cuts are considered, without any efficiency correction.

The counting rate can be derived by dividing the number of events, in a specific time bin, by the effective exposure. Effective exposure is defined as

$$\mathcal{E}^{ch,i} = M \cdot E \cdot T_{live}^{ch,i} \cdot \epsilon_{M1} \cdot \epsilon_{\chi^2_{OT}} \tag{5.1}$$

where M is the mass of crystal, E is the width of the energy slice, $T_{live}^{ch,i}$ is the acquisition time and depends on the channel ch and the period covered by the i-th time bin[1], ϵ_{M1} and $\epsilon_{\chi^2_{OT}}$ are the acceptance efficiency of the multiplicity

[1]Here the analysis threshold is considered: a channel-dataset pair does not contribute if its analysis threshold is above the lower energy bound of the considered slice.

Data set	Start date	End date
2079	2013-11-17	2013-12-11
2085	2013-12-20	2014-01-20
2088	2014-01-17	2014-02-24
2091	2014-02-18	2014-03-20
2097	2014-03-24	2014-04-17
2100	2014-04-15	2014-05-15
2103	2014-05-12	2014-06-13
2109	2014-06-13	2014-07-21
2124	2014-08-29	2014-10-03
2130	2014-11-07	2014-12-09
2139	2015-01-19	2015-03-02

Table 5.1: *List of datasets used in this analysis.*

and χ^2_{OT} cut respectively. The histograms obtained by this division will be called efficiency-corrected-rate histograms (an example of the two histograms, obtained by summing the counts from a set of 22 channels, can be found in figure 5.2).

In the first part of this chapter the fitter used to analyze data from a single channel is discussed; in particular the reason why the *minimum* χ^2 method can not be used will be illustrated. The fitting algorithm is based on ROOT C++ classes, and adopts some approximations, the most relevant of which is the "scaling procedure" whose description and validation are given in section 5.2. In section 5.3 the simultaneous fitter, required to analyze data from all the channels at the same time, will be presented. Finally, in section 5.4, results and possible sources of systematic errors will be discussed.

5.1 Single channel fit

5.1.1 Flat function fit

The histogram to be fitted, the efficiency-corrected-rate histogram, contains the event rate vs time. Given the low statistics (from tens to hundred events per bin depending on the exposure and the energy interval) a robust validation of the fitting algorithm is required before the real-data analysis. A first way to highlight a bias in the fitting algorithm is to use the fitter to evaluate the average counting rate. This is obtained by using a flat fit function.

A toy Monte Carlo simulation has been developed to test the fitter and showed that the the fitter is biased when using the *minimum* χ^2 method. The following simulations assume a time binning of 30 days and 5-keV-wide

energy slices.

The test consists in the generation of a set of histograms (I will call them *MC histograms* or *pseudo-experiments*), simulating CUORE-0 data, and check the distribution of the average event rate returned by the fitter. Every pseudo-experiment is produced by means of the Poisson distribution as follows:

1. Assuming a certain value of event rate R_{theo}, evaluate the number of expected counts N_{theo} in every time bin considering also the effective exposure $\mathcal{E}$ in that bin $N^i_{theo} = R_{theo} \times \mathcal{E}^i$

2. Use this value to extract the experimental number of counts using a Poisson distribution with mean value N^i_{theo}: $N^i_{exp} = Poisson(N^i_{theo})$

3. Fill the histogram with the efficiency-corrected rate $R^i_{bin} = N^i_{exp}/\mathcal{E}^i$

4. Set the bin error to $E^i_{bin} = \sqrt{N^i_{exp}}/\mathcal{E}^i$, where $\sqrt{N^i_{exp}}$ is the Poisson standard deviation.[2]

At this moment we have an almost flat histogram, in which the bin errors can be very different because of the different exposures (lower exposure corresponds to higher bin error). An estimation (R_{fit}) of the true rate R_{theo}, per each MC histogram, is then extracted by the flat fit. The pull is used to check the fitter bias; it is defined as

$$\frac{R_{fit} - R_{theo}}{\sigma_{fit}} \tag{5.2}$$

where σ_{fit} is the error of R_{fit} returned by the fitter. This quantity should be described by a Gauss distribution centered on zero and standard deviation equal to one. When using the *maximum likelihood* method the average value is found not to be compatible with zero (see figure 5.1). This procedure shows that the fitter is biased, in particular it underestimates the rate. This behavior can be due to two facts. The first is that the bin content is described by a Poisson distribution, on the contrary the *minimum* χ^2 fit method assumes the bin errors to be Gauss-like. In particular, the lower is the statistics in the bin, the higher this effect is. The second is that, since the bin error $\sqrt{N^i_{exp}}/\mathcal{E}^i$ is evaluated using the randomly extracted number N_{exp} instead of the original number N_{theo}, when the extracted value is small also its error is small, and vice versa, while the error should be independent from

[2] This assumes the bin error to be symmetric, this wrong assumption is the origin of the failure of this first test.

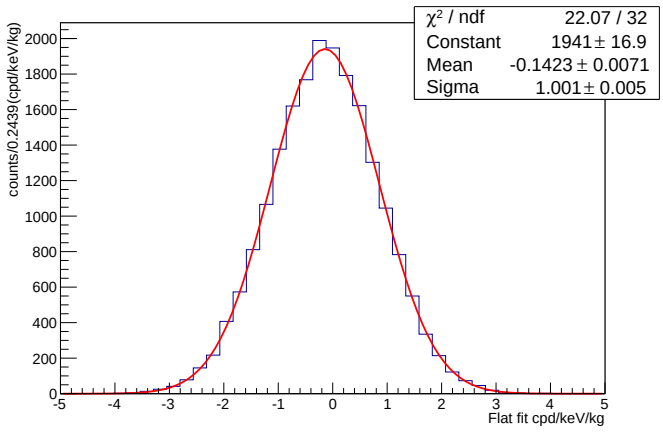

Figure 5.1: *Average rate pull distribution obtained from maximum likelihood flat fit, using 20000 simulated experiments that do not contain any modulation signal. Note that the mean value -0.1423±0.0071 is not compatible with zero.*

the extracted value. This second fact could explain why the fitter underestimates the rate: every time the random extraction in a certain bin gives a value smaller than R_{theo}, the fitter is driven by that bin (and its small error) to a smaller value of R_{fit}. On the contrary, when the extraction gives a value bigger than R_{theo}, the fitter is less affected by that bin because its error is bigger than in the previous case.

This bias can be removed by using the *maximum likelihood* fit method. In this case the likelihood function is based on the assumption that the bin error is the asymmetric error of the Poisson distribution. This assumption, perfectly satisfied by the toy MC data, is also valid for the original-total-counts histogram if we assume that only statistical fluctuations affect the bin content. Other sources of uncertainty are discussed in 5.2. Consequently an interval-defined function is required to fit the original-total-counts histogram, in order to take into account different exposures in different bins. The interval-defined function is shown by the red solid line in the bottom plot of figure 5.2. The pull distributions obtained with the *maximum likelihood* method (using the original-total-counts histogram) and the *minimum* χ^2 method (using the efficiency-corrected-rate histogram) have been compared with a third pull distribution. The third distribution is obtained simply evaluating the algebraic mean of the rate per every MC histogram, since the goal of this check is to test fitter capability to evaluate the average rate. The three pull distributions, from a set of 100 000 simulations, have been fitted with a Gauss function whose parameters are reported in table 5.2. The likelihood method, with respect to the χ^2 one, shows an average pull value closer to

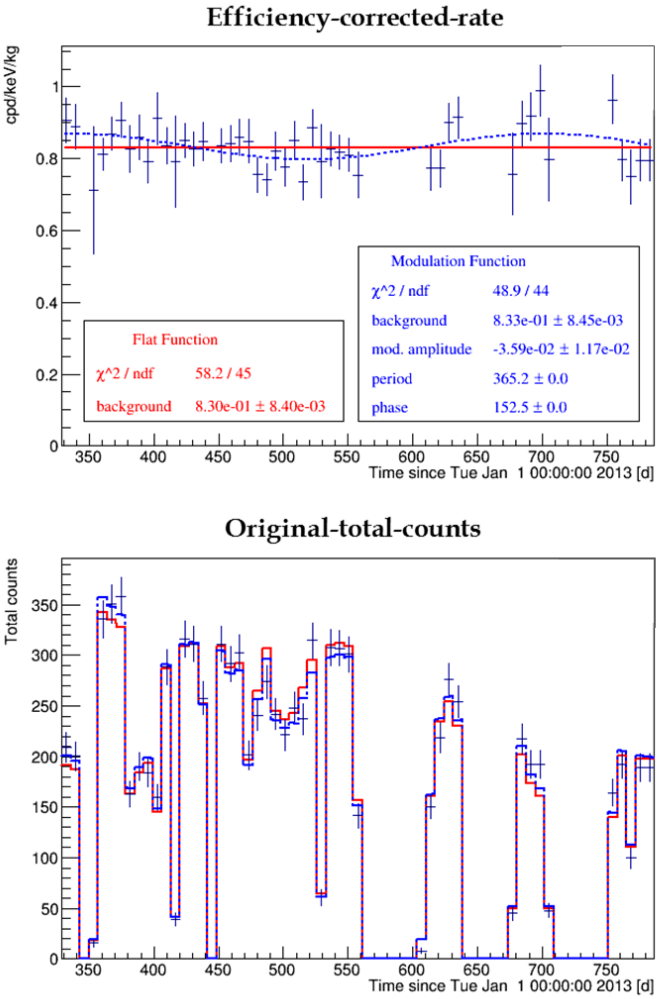

Figure 5.2: *An example of fitted histograms obtained by summing the events, in the 32-34 keV energy interval, of all the 49 available channels. The efficiency-corrected-rate histogram (top) used by the first implementation of the fitter and original-total-counts histogram (bottom) processed by the fitter that uses the maximum likelihood method. The red solid lines represent the flat fit function, the blue dotted lines represent the modulated function (explained in the next section). In this case a time binning of 7.6 days has been used*

Parameter	Algebraic mean	likelihood	χ^2
Amplitude	5333±21	5334±21	5332±21
Mean	-0.0051±.0032	-0.0055±0.0032	-0.0878±0.0032
Sigma	0.997±0.002	0.996±0.002	0.997±0.002
χ^2/ndf	81/57	82/57	51/57

Table 5.2: *Comparison between the pulls obtained from different methods. The pull distributions are fitted with a Gauss function and parameters values are reported. The maximum likelihood fit results (third column) are more similar to the ones from the simple algebraic mean of the rate (second column) than the ones from minimum χ^2 fit (fourth column). In particular the Mean, which in the likelihood fit is 2σ-compatible with zero, demonstrates a bias in χ^2 fit.*

zero (less than 2σ of deviation) and very close the one obtained by the simple average method.

5.1.2 Modulating function fit

The second check has the goal to test if the fitter is biased when using the sinusoidal function which is needed to test the modulation hypothesis. The MC efficiency-corrected-rate histograms, not containing modulation signal, are fitted with the *minimum* χ^2 method. The fit function contains a cosine describing a modulating rate (corresponding to the time-dependent rate expressed in 2.21)

$$f_{\chi^2}(t) = R(t) = R_0 + R_m \cdot Cos\left(\frac{2\pi}{T}(t - t_0)\right) \tag{5.3}$$

where R_0 is the rate background amplitude, R_m is the rate modulation amplitude, t_0 is the maximum position (namely June 2^{nd}) and T is the modulation period.

The MC original-total-counts histograms are fitted, indeed, with the *maximum likelihood* and including the effective exposure, defined in equation 5.1, in the fit function:

$$f_{likelihood}(t) = R(t) \cdot \mathcal{E}^i \tag{5.4}$$

In these fits the period is fixed to 365.25 days, and the phase is fixed to a random value between 0 and 365.25 days, in order to scan all the possible values of the phase. The reason of the phase scan is to check how the detector efficiency pattern affects amplitudes results; for example we can expect a larger amplitude dispersion when the maximum, or the minimum, of the cosine function falls in a bin with low detector efficiency (because that bin

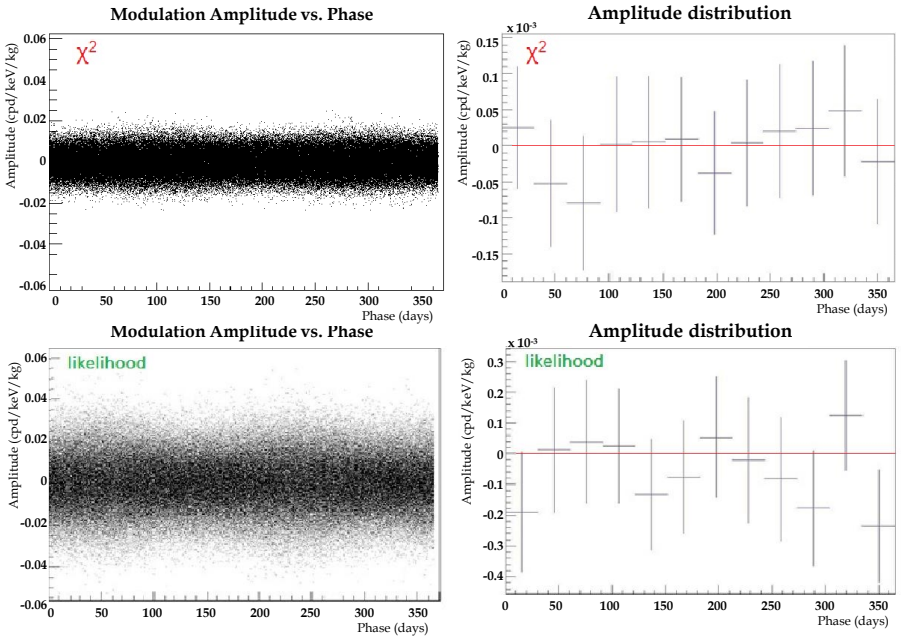

Figure 5.3: *On the left: scatter plot of estimated modulation amplitude versus phase (fixed to a random value) using minimum χ^2 (top) and maximum likelihood (bottom) fit method. The simulation assumes a detector efficiency constant over time. On the right: the scatter plots are divided in 12 phase regions (one per month) and the corresponding average amplitudes are reported (with 1σ error bars).*

presents a larger uncertainty). During this check it has been seen that the starting value of amplitude does not affect fit result.

When using a constant-in-time exposure, the obtained amplitudes from *minimum* χ^2 and *maximum likelihood* fitters are almost equal, even if the second one shows a bigger spread of returned values. This is visible in the scatter plots in figure 5.3 (left) in which every point represents a pseudo-experiment. To better compare the results, all the values falling inside a month-wide phase range have been grouped and the average amplitude of that subset of simulations has been evaluated (figure 5.3, right). In case of unbiased fitter we expect that each subset has an average value compatible with zero. Both fitters passed this test since all the values are compatible with zero within two sigma, even if, as expected from scatter plots, the likelihood method returns wider distributions.

This test doesn't represent a realistic scenario because of the large variability of the exposure from bin to bin. When using real efficiency values, we obtain very different results. The likelihood fitter shows deviations from zero, for the modulation amplitude, smaller than two sigma like in the previ-

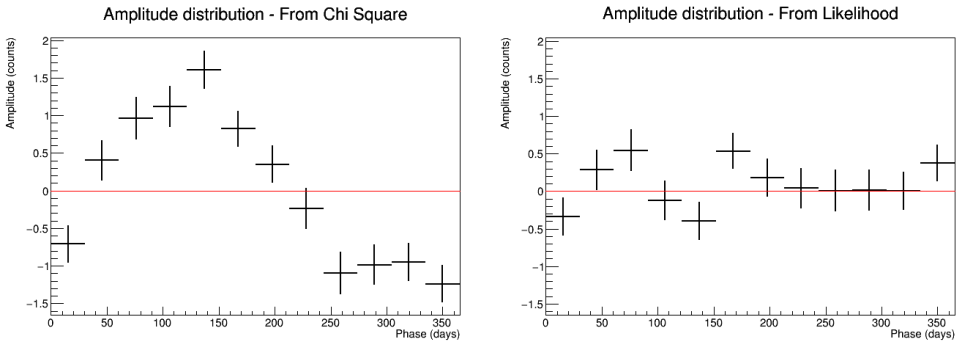

Figure 5.4: *Each point represents the average modulation amplitudes of a subset of simulated experiments, obtained binning the phase which is fixed fit by fit to a random value. The pseudo-experiments did not contain a modulation signal but the detector exposure has been considered in data production (this is the difference with respect to fig. 5.3). The modulation amplitudes have been estimated by means of minimum χ^2 fit (left plot) and maximum likelihood fit (right plot). The vertical error bars represents 1σ errors of the mean value. Values returned by χ^2 fits (left plot) show a bias which depends on the modulation phase.*

ous test, while the *minimum* χ^2 method produces significant deviations from zero, in correspondence of certain phases. Figure 5.4 illustrates the results obtained considering CUORE-0 efficiencies evaluated in the energy range 25-30 keV. In this case the residuals reaches a value bigger than 6 for the χ^2 fitter (fifth bin of left plot) and slightly bigger than 2 for the likelihood one (sixth bin of right plot).

In conclusion, the *minimum* χ^2 method introduces a bias both using a flat function, underestimating the average rate, and using the modulation function, because it returns, in average, modulation amplitudes far from zero even if the used pseudo-experiments are generated with a constant-in-time event rate. On the contrary, the *maximum likelihood* method works as expected because it assumes that every bin is affected by Poisson fluctuations. This assumption is satisfied by the original-total-counts histogram, which contains the number of events without efficiency correction, and is not valid for the efficiency-corrected-rate histogram. As consequence, using the original-total-counts histogram, the effective exposure, which is different from bin to bin, must be included in the fit function.

5.2 χ^2_{OT}-cut efficiency uncertainty

In the previous section only the statistical fluctuations have been considered as source of uncertainty of bin occupancy. Even if this is true when considering the original-total-counts histogram, it must be noticed that the fit function, which contains the effective exposure, is still affected by several uncertainty sources.

The fit function used to fit the original-total-counts histogram (already presented in eq. 5.4) describes the expected rate, as function of time, multiplied by the bin-dependent effective exposure $\mathcal{E}^i$ defined in equation 5.1:

$$f_{likelihood}(t) = \left[R_0 + R_m \cdot Cos\left(\frac{2\pi}{T}(t - t_0)\right)\right] \cdot \mathcal{E}^i \tag{5.5}$$

being R_0 the average rate, R_m the modulation amplitude of the rate and

$$\mathcal{E}^i = M \cdot E \cdot T^i_{live} \cdot \epsilon_{M1} \cdot \epsilon_{\chi^2_{OT}} \tag{5.6}$$

where M is the mass of a CUORE-0 crystal, E is the width of the considered energy range, ϵ_{M1} is the efficiency of the multiplicity cut due to random coincidences, T^i_{live} is the detector live time of the bin which contains the time t and $\epsilon_{\chi^2_{OT}}$ is the signal acceptance of the χ^2_{OT}-cut (typically 0.5 or 0.9).

The uncertainty of detector live time T^i_{live} can be easily estimated: it is the error in measuring the run duration ($\sim$1 second) times the number of run that fall into the considered time bin which is of the order of 10 runs per month. In practice the relative uncertainty is about tens of seconds per month ($O(10^{-5})$), so it is negligible.

A more significant source of uncertainty is represented by the χ^2_{OT}-cut signl acceptance efficiency $\epsilon_{\chi^2_{OT}}$. As explained in sec. 4.4.2 it is caused by the statistical fluctuations in the 35-50 keV range and it is estimated with Agresti-Coull method. At this point we can consider that each bin in total counts vs time histogram is affected by two independent sources of uncertainty: statistical fluctuations and fluctuations (in the number of counts) induced by χ^2_{OT}-cut uncertainty ($\sigma_{\chi^2_{OT}}$). We can handle the first source of uncertainty simply performing the fit using the *maximum likelihood* algorithm but this prevents to set bin errors to include $\sigma_{\chi^2_{OT}}$.

5.2.1 χ^2_{OT}-cut uncertainty inclusion

The algorithm to include $\sigma_{\chi^2_{OT}}$, here explained, is based on an approximation so a consistency check of the implementation is required and provided in sec. 5.2.2.

Even if a more rigorous implementation could be done by using a more sophisticated tool such as CERN RooFit[3], we will show here that this approximate method matches the analysis requirements. Moreover the approach here adopted consists in few simple algebraic steps and thus it does not affect significantly the computation time; on the contrary, an exact approach to this problem would lead to a complex and time-consuming calculation. This last aspect is particularly relevant in case of MC simulation (as for the test described in sec. 5.1), where the computation time of a simulation, involving several thousands of fit procedures, can reach a few days if it is faced with exact tools.

The explanation of this method is based on two considerations. The first consideration is that, in first approximation, (i) the $\sigma_{\chi^2_{OT}}$ uncertainty has the effect to increase the standard deviation of the bin content. According to this, the total bin error is the square sum of the two single-effect errors.[4]

$$\sigma_{tot} = \sqrt{\sigma^2_{pois} + \sigma^2_{\chi^2_{OT}}} \tag{5.7}$$

where σ^2_{pois} represents the Poisson fluctuations already treated in the previous section. The fit algorithm must consider σ_{tot} instead of simply σ_{pois}.

The second consideration is that (ii) if, in a generic fit, we multiply the bin contents N^i, the bin errors σ^i[5] and the fit function $f(t)$ by the same value (I will refer to this scale factor as S_f) the best-fit function does not change, because the relative errors r (the ratio between bin error and bin content) does not change.

Regarding this second point, it must be noticed that a similar approach has been used in sec. 5.1.2 when the original-total-counts histogram has been used in place of the efficiency-corrected-rate histogram. In that case (see eq. 5.5) the scaling factor was the bin-dependent effective exposure $\mathcal{E}^i$.

On the other hand in a *maximum likelihood* fit the bin error cannot be set by the user but is automatically set by the Poisson distribution, whose standard deviation is the square root of the bin content. In this case the scale factor can be applied only to the bin content and the fit function (the

[3] It is a toolkit for Data Modeling that allows for modeling probability distributions in the ROOT framework.

[4] They are two independent uncertainty sources.

[5] This cannot be done in a *maximum likelihood* fit, but it is possible in a *minimum* χ^2 fit.

apostrophe denotes the after-scaling quantities):

$$N^i \longrightarrow N'^i = S_f N^i, \qquad f(t) \longrightarrow f'(t) = S_f f(t) \tag{5.8}$$

This means that the standard deviation attributed to the bin content (or simply the bin error) is scaled by a factor $\sqrt{S_f}$:

$$\sigma^i = \sqrt{N^i} \quad \longrightarrow \quad \sigma'^i = \sqrt{S_f N^i} = \sqrt{S_f}\sigma^i, \tag{5.9}$$

and the relative error is scaled by a factor $1/\sqrt{S_f}$:

$$r^i = \frac{\sigma^i}{N^i} \quad \longrightarrow \quad r'^i = \frac{\sqrt{S_f}\sigma^i}{S_f N^i} = \frac{r^i}{\sqrt{S_f}} \tag{5.10}$$

If we scale both the bin content and the fit function, the total effect in a *maximum likelihood* fit is to change the relative errors.

This effect can be used to manipulate the bin error, in order to force the fit to consider the real error σ^i_{tot} instead of σ^i_{pois}, which means to require that:

$$r'^i = \frac{1}{\sqrt{N'^i}} = \frac{1}{\sqrt{S_f N^i}} \equiv \frac{\sigma^i_{tot}}{N^i} \qquad \Longrightarrow \qquad S_f = \frac{N^i}{(\sigma^i_{tot})^2} \tag{5.11}$$

The inclusion of $\sigma_{\chi^2_{OT}}$ in the fit procedure is obtained by finding, in every bin, the value of S^i_f that produces the required relative error of that bin. The values S^i_f are then used to multiply both the bin content and the portion of the fit function corresponding to that bin. In practice, here it is how the scaling procedure works:

1. The DS-dependent χ^2_{OT}-cut signal acceptance efficiency uncertainty σ^{DS}_ϵ is computed by means of the Agresti-Coull method.

2. When the original-total-counts histogram is produced, the DS-dependent errors on the efficiency σ^{DS}_ϵ are converted into the bin-dependent errors on the bin occupancy $\sigma^i_{\chi^2_{OT}}$,

$$\sigma^i_{\chi^2_{OT}} = \sqrt{\sum_{DS} \left(N^{i,DS} \, \frac{\sigma^{DS}_\epsilon}{\epsilon_{\chi^2_{OT}}} \right)^2} \tag{5.12}$$

   where a sum over the datasets is performed and $N^{i,DS}$ is the number of events, from dataset DS, that contributes to the i-th time bin. $\sigma^i_{\chi^2_{OT}}$ is used to evaluate σ_{tot}, according to eq. 5.7.

3. The scale factors S^i_f are computed, according to eq. 5.11, for every bin,

and used to scale (reduce) the bin contents of the original-total-counts histogram.

4. The fit function is also scaled by the same factors: the portion of the function corresponding to the i-th time-bin is multiplied by S_f^i.

At this point the usual *maximum likelihood* fit is performed.

5.2.2 Consistency checks

The *maximum likelihood* fitting procedure is based on the minimization of the negative log-likelihood function (which corresponds to the maximization of the likelihood function). The likelihood function is defined by assuming a specific probability density function (PDF) for the content of every bin, in this case the number of events that CUORE-0 measured during a certain period. Therefore it is fundamental that the PDF assumed by the fitter to build the likelihood function, which is a Poisson distribution, is as similar as possible to the real continuous distribution underlying the experimental data. The first check consists in the production of a set of bin content values, also reproducing the effect of the $\sigma_{\chi^2_{OT}}$ uncertainty, whose distribution is compared with the one adopted by the fitter (i.e. the Poisson distribution).

The bin content in the original-total-counts histogram probability distribution comes from, in first approximation, the combination of the two described effects: the statistical fluctuation and the χ^2_{OT}-cut selection. The "compatibility" of the two distributions can be quantified by generating a set of values, representing possible values of the experimental data, by scaling them, with the procedure described in sec. 5.2.1, and fitting the obtained distribution with the Poisson function.

Each value of the experimental distribution is generated as follows. First, a number of events N_{pois} is randomly generated by the Poisson PDF whose mean value is N_{mean}:

$$N_{pois} = \texttt{TRandom3::Poisson}(N_{mean}) \tag{5.13}$$

where N_{mean} is the expected number of events and `TRandom3` is the ROOT class used to generate random values. To reproduce the variability induced by $\sigma_{\chi^2_{OT}}$, a second number N_{exp} is randomly extracted by the Gauss distribution whose mean value is N_{pois} and standard deviation is $\sigma_{\chi^2_{OT}}$:

$$N_{exp} = \texttt{TRandom3::Gaus}(N_{pois}, \sigma_{\chi^2_{OT}}) \tag{5.14}$$

By the repetition of this double extraction a set of N^j_{exp} is obtained,

where j is the index that runs over the number of extractions; it represents the experimental probability distribution of the content of a single bin.

If the N^j_{exp} values are shrunk by the factor S_f ($N^j_{exp} \rightarrow N^j_{exp}/S_f$), the scaling procedure is reproduced. At this point the distribution N^j_{exp}/S_f is fitted with a Poisson distribution whose mean value is expected to be $\mu = N_{mean}/S_f$.

In figure 5.5, for implementation and graphical reasons, the Poisson distribution has been stretched out in place of the shrinking of the experimental distribution. This means that the N^j_{exp} distribution is compared with $Poisson(x/S_f)$ (scaled Poisson function) in place of the simple $Poisson(x)$. The red histogram has been filled with 100 000 values of N_{pois}, generated from $N_{mean} = 25$, and the fit function is a Poisson function with mean value 25. The blue histogram has been filled with 100 000 values of N_{exp}, generated from N_{pois}, in which $\sigma_{\chi^2_{OT}} \equiv \sigma_{pois} = \sqrt{25} = 5$ has been set. This is a conservative assumption since $\sigma_{\chi^2_{OT}}$, in this analysis, is always smaller than the statistical fluctuations.

According to equation 5.7, $\sigma_{tot} = \sqrt{2}\sigma_{pois} = 5\sqrt{2}$ which means that (from equation 5.11) $S_f = 0.5$. The blue line represents the scaled Poisson function that has mean value 25 but standard deviation $5\sqrt{2}$, in other words it is a regular Poisson function with mean 12.5, stretched out by a factor $1/S_f = 2$. The scaled Poisson function represents the probability density function used by the likelihood fitter to handle the error of a bin containing 12.5 counts.

In conclusion the experimental data obtained by this simulation (the blue histogram) and the scaled Poisson function (the blue function) are in good agreement since the fit returns the value $\chi^2/ndf = 54.1/68$. Moreover the scaled Poisson fit gives an unbiased estimation of the mean value $\mu = 24.995 \pm 0.071$, well compatible with the true value $N_{mean} = 25$.

The second check consists in the production of a set of randomly generated original-total-counts histograms that do not contain modulation signal. The pull distribution returned by a flat fit (as in sec. 5.1.1) is then computed. The bin content is generated assuming a constant rate, equal to $N_{mean} = 1000$ events divided by the maximum possible exposure (i.e. a detector duty cycle equal to 100%). As opposed to the first check described in 5.1.1, bin content is generated not only using the Poisson distribution but doing a second extraction from a Gaussian distribution. This second extraction is done, as usual, to simulate the χ^2_{OT} efficiency uncertainty. In order to be as general as possible, the χ^2_{cut} efficiency uncertainty is randomly fixed to a different value, uniformly distributed from 5% to 10% of N_{mean}, in every bin of every pseudo-experiment. This is a conservative assumption because the

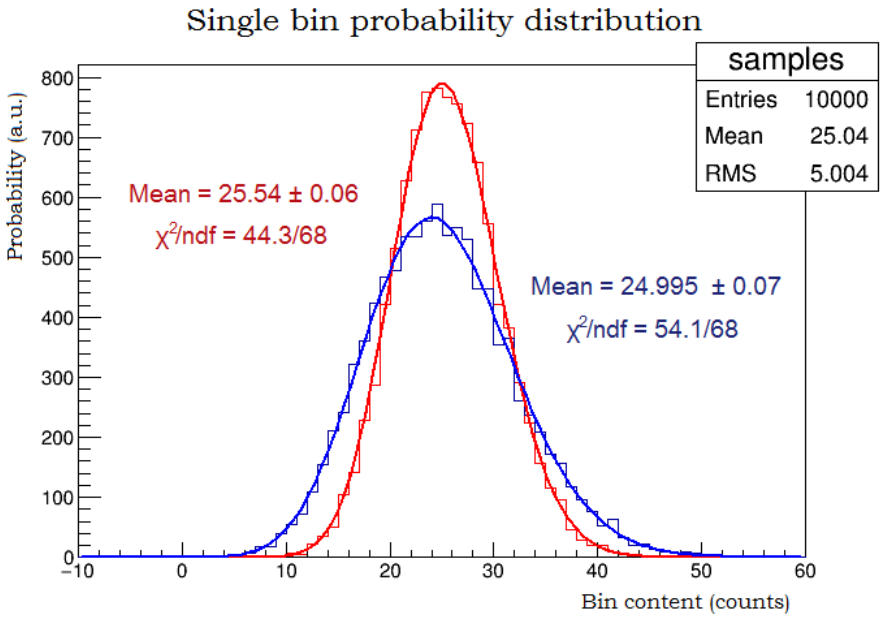

Figure 5.5: *Simulation of the probability distribution of a single bin of the original-total-counts histogram. The red histogram represents the case of a bin with mean value* $N_{mean} = 25$ *in which* $\sigma_{\chi^2_{OT}} = 0$ *and is fitted with a Poisson function (red line). The blue histogram shows the simulation results in which* $\sigma_{\chi^2_{OT}} = \sigma_{pois}$ *and is fitted with the corresponding scaled Poisson function having standard deviation equal to* $5\sqrt{2}$.

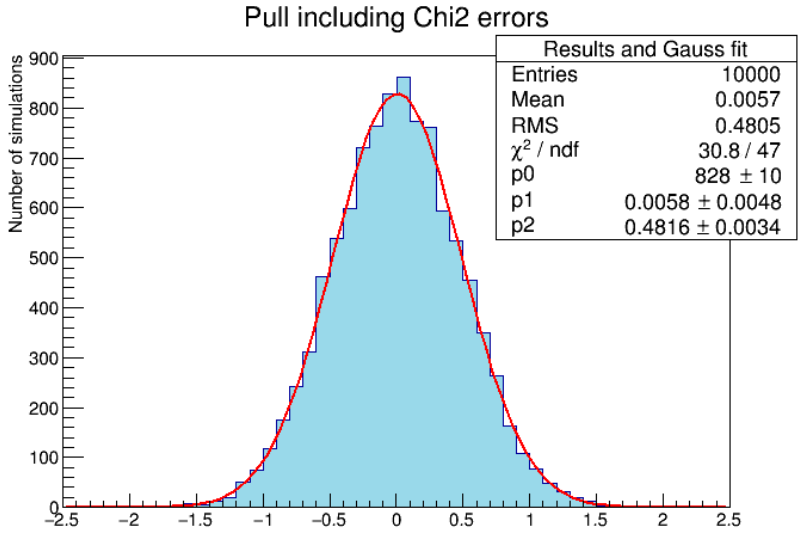

Figure 5.6: *Pull of the number of events per bin estimated by the fitter over a set of 10000 pseudo-experiments. Each pseudo-experiment has been created assuming a constant-in-time value of 1000 events/bin (no modulation signal), detector live time effect and* $\sigma_{\chi^2_{OT}}$ *uncertainty have been included in the random generation algorithm. The fitter results to be unbiased (the mean value p1 is compatible with zero within* 2σ*).*

χ^2_{OT}-cut efficiency uncertainty is always smaller than 1%.

The scaling procedure is applied to every pseudo-experiment. The pull of the average counts returned by the flat fit is computed for every MC experiment:

$$\frac{N_{fit} - N_{mean}}{\sqrt{N_{mean}}} \tag{5.15}$$

where N_{fit} is the average number of events per bin returned by the fit.

In figure 5.6 the distribution of the pull average amount of event per bin (theoretically $N_{mean} = 1000$ events/bin) for a set of 10 000 generated histograms is shown. Note that the pull standard deviation should be close to 1 but $\sqrt{N_{mean}}$ is not the standard deviation of N_{fit}. $\sqrt{N_{mean}}$ is the standard deviation of a single bin, assuming the biggest possible exposure. Actually every bin has a smaller number of events, because the detector duty cycle and the cut efficiencies are smaller than 1, and this causes a reduction of the uncertainty of a single bin but, at the same time, the uncertainty is increased by the inclusion of the χ^2_{OT}-cut uncertainty. Moreover the fit procedure takes into account 15 bins (representing the 15 months of data available from CUORE-0), so the standard deviation of the fit results is roughly $1/\sqrt{15}$

times the uncertainty of a single bin. These three effects result in an RMS value, given by the simulation, of $0.48\sqrt{N_{mean}}$. The average value of the distribution is 0.0058 ± 0.0048 and is compatible with zero and therefore the scaling procedure does not introduce a bias in the fit.

5.3 Simultaneous fit

The explained fit procedure can be used to analyze a single CUORE-0 channel, but the data here considered come from 49 different channels. A possible approach to consider all the channels could be to sum, time-bin by time-bin, the events from all channels and evaluate the exposure in a given time-bin as the sum of the exposure of the channels that contribute to that time interval. Nevertheless this technique could artificially produce a modulation signal as here explained. Even if the modulation signal is expected to have the same amplitude and phase in all channels, the background rate could be, in principle, channel-dependent. Since the exposure of each channel changes from time-bin to time-bin, also the relative weight of its background changes from time-bin to time-bin. Thus, the presence of data from a channel, with high background rate, in a certain time-bin has the effect to increase the event rate for the corresponding period, which means to introduce an artificial time dependence of the event rate.

In order to avoid this effect, a simultaneous fit procedure is adopted. Every channel is independently fitted, with the constrain that, differently from the background, the modulation amplitude, as well as phase and period, must be the same for all the channels (all crystals have the same probability to detect a DM particle). In practice, to simultaneously consider 49 channels, 49+3 parameters are used: 49 channel-dependent background amplitudes R_0^{ch} and the modulation signal parameters: amplitude R_m, period T and phase $\phi = 2\pi t_0/T$ (the same notation as in eq. 5.5 has been used).

The implementation of the simultaneous fit is based on the fact that the Likelihood function, associated to 49 sets of data (the single channel histograms) is the product of the 49 single-set likelihood functions. If $\theta_m = \{R_m, T, \phi\}$ are the three modulation signal parameters, and x^{ch} are the obtained counts for channel ch, then the total likelihood $\mathcal{L}_{tot}$ can be expressed as:

$$\mathcal{L}_{tot}(\theta_m, R_0^1, ..., R_0^{49}|x^1, ..., x^{49}) = \prod_{ch=1}^{49} \mathcal{L}(\theta_m, R_0^{ch}|x^{ch}) \tag{5.16}$$

and the negative log-likelihood, which is minimized by ROOT to find the parameters best values, becomes the sum of the single-channel contributions.

As described in the previous section, in order to include χ^2_{OT}-cut uncer-

tainty, also in this case single channel histograms and fit functions are scaled by the scale factors (time and channel dependent) before the fit.

5.4 Results

Results from simultaneous fits, performed with the same χ^2_{OT}-cut efficiency and in different energy slices, are grouped to form a "modulation amplitude spectrum". Since every channel-dataset pair has a different analysis threshold, it contributes only in the energy bins above its threshold. The channel-dataset pairs that present an analysis threshold higher than 35 keV are totally rejected because such threshold is above the low boundary of the energy region used to estimate the χ^2_{OT}-cut (see sec. 4.4.2).

Figure 5.7 (top) shows the obtained rate modulation amplitudes, expressed in cpd/keV/kg, in 2-keV-wide energy slices, for the 48 available CUORE-0 channels (see tab. 4.2) and using the $\chi^2_{90\%}$ cut. The time binning for the simultaneous fit is 7.6274 days. Period and phase were fixed to 365.25 days and 152.5 days respectively (according to WIMP-induced modulation signature). Modulation amplitude values are reported in table 5.3.

The uncertainty bands (blue bands) show 1σ, 2σ and 3σ errors on the modulation amplitude obtained by the fit. They present a large energy dependence that can be explained as follows. The uncertainty on the modulation amplitude is related to the single time bin errors which is, excluding minor sources of uncertainty, roughly proportional to $\sqrt{N^i}/\mathcal{E}^i$ (N^i and $\mathcal{E}^i$ are the number of counts and the exposure in the i-th time bin respectively).

CUORE-0 multiplicity 1 spectrum (figure 4.11) shows a larger background at low energies. Moreover the exposure increases as the energy increases up to 35 keV (fig. 4.11, right). According to this, the first energy slices, up to 30 keV, show a large amplitude uncertainty. In addition to this, the error grows as the square root of the counts; this effect is well visible in the 34 - 40 keV bump.

In total four intervals show amplitudes bigger than 1σ: 14 - 20 keV, 24 - 26 keV, 30 - 34 keV and 40 - 44 keV. The modulation is more than 2σ far from zero in only one bin: 32 - 34 keV. The region above 50 keV is plotted mainly as a check, because the WIMP signal contribution is expected to be negligible in that region.

Figure 5.7 (bottom) shows the likelihood ratio test values [106]. The likelihood ratio test $\chi^2_{\mathcal{L}}$ is used to compare two nested hypothesis H_0 and H_1. H_0 is nested with H_1 if it can be considered a particular case of H_1, obtained by constraining some of the H_1 parameters. In this case the flat fit (H_0) can be considered the particular case of the modulated fit (H_1) in

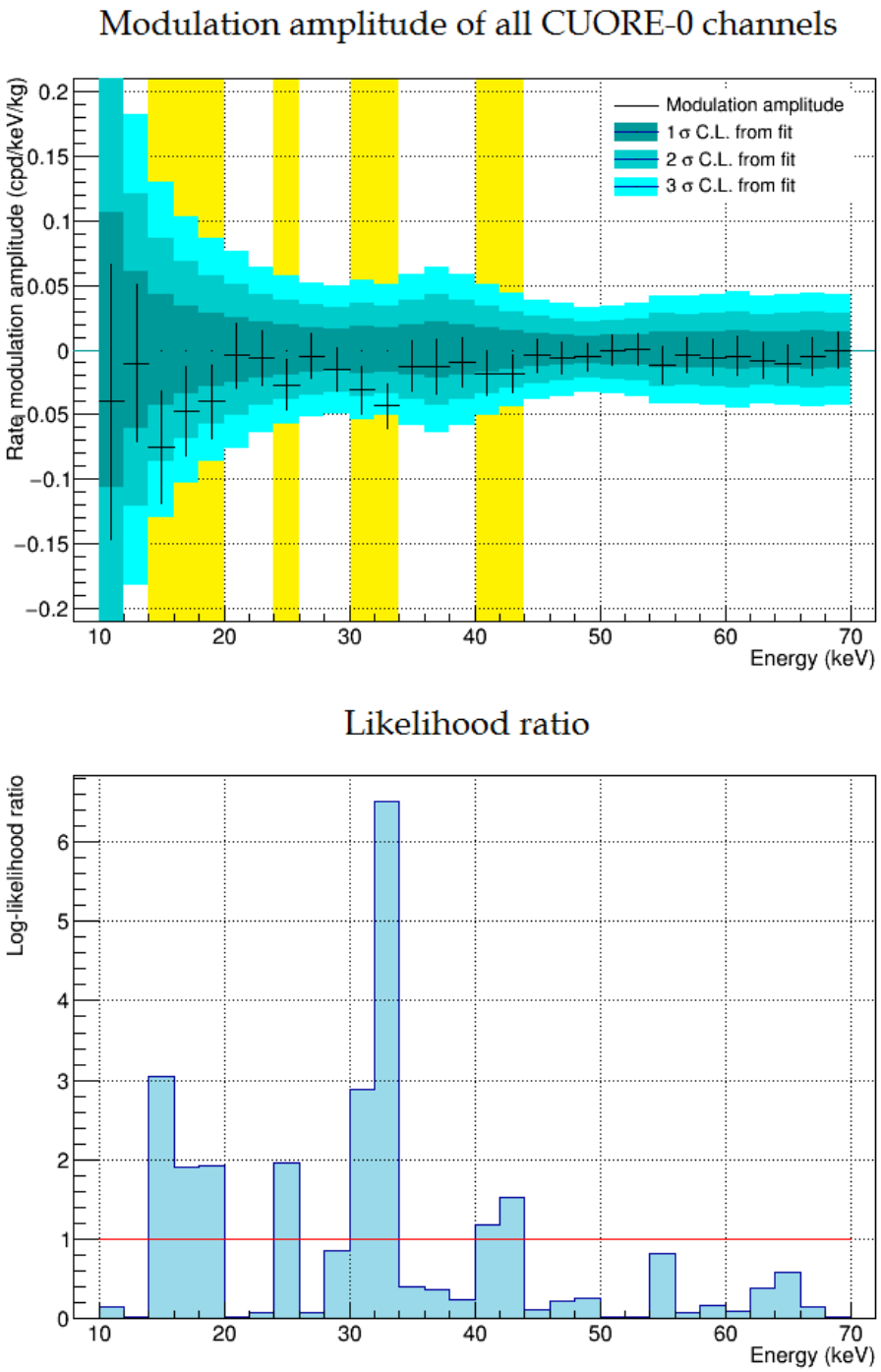

Figure 5.7: *Top: Modulation amplitude spectrum obtained for all CUORE-0 channels. Every modulation fit has been made on a 2-keV-wide energy slice, with a time binning of 7.6 days. The* $\chi^2_{90\%}$ *cut (90% of signal acceptance) has been used. Bottom: The likelihood ratio test can be used to compare the statistical significance of every modulation fit compared with the flat fit of the same energy slice.*

which the modulation amplitude if fixed to zero. $\chi^2_{\mathcal{L}}$ is defined as:

$$\chi^2_{\mathcal{L}} = 2\ln\mathcal{L}^1_{tot} - 2\ln\mathcal{L}^0_{tot} \tag{5.17}$$

where $\mathcal{L}^1_{tot}$ and $\mathcal{L}^0_{tot}$ are the likelihood values obtained by the simultaneous modulated and flat fits respectively. The test value $\chi^2_{\mathcal{L}}$ asymptotically obeys a chi-square distribution in which the number of degree of freedom (ndf) is given by the difference of the numbers of free parameters of the two models. When fixing both modulation period and phase, the only free parameters, which is considered in $\mathcal{L}^1_{tot}$ and not in $\mathcal{L}^0_{tot}$, is the modulation amplitude so ndf is 1.

Above 50 keV, where no modulation is expected, $\chi^2_{\mathcal{L}}$ is close to 1 or smaller. This means that, for that energies, the null hypothesis must be preferred to the modulated one with p-values roughly equal or bigger than 50%. In 32 - 34 keV interval, where the modulation is more than 2σ far from zero, the log-likelihood value is bigger than 3.84. $\chi^2_{\mathcal{L}} = 3.84$ corresponds to the flat hypothesis rejection at 95% C.L.

In general the statistical significance of the amplitude in the single energy bins is small, however it must be noticed that all the amplitudes are negative. This last fact is not in contrast with the expectations: in fact, for kinematic reasons, the amplitude can be negative for low recoil energies (see fig. 2.4). Nevertheless the modulation energy dependence, which is not smooth but presents a local minimum at 33 keV, is not reflected in WIMP-induced modulation signature (see again fig. 2.4). In particular the correspondence of this peak in the modulation amplitude spectrum with the unexplained bump in the CUORE-0 low energy spectrum rises the suspect that such modulation is induced by a radioactive source.

In conclusion, even if we see a hint of modulation its energy dependence prevent us to conclude that it is induced by WIMPs.

In the next sections some possible sources of systematic error are taken into account.

5.4.1 ^{210}Pb background

As stated is section 4.4.5, the bump around 40 keV that is clearly visible in CUORE-0 multiplicity 1 spectrum (see figure 4.11) could be due to a ^{210}Pb contamination. In principle, a ^{210}Pb-induced decaying background could affect the modulation analysis results. This effect has been studied by adding a new component to the fit function (see equation 5.5):

$$f_{likelihood}(t) = \left[R_{Pb}\cdot e^{-t/\tau} + R_0 + R_m \cdot Cos\left(\frac{2\pi}{T}(t-t_0)\right)\right]\cdot\mathcal{E}^i \tag{5.18}$$

Energy (keV)	Mod. Ampl. (cpd/keV/kg)	Residual	Time Binning Error (10^{-3} cpd/keV/kg)	Exposure (kg·year)
10-12	-0.040 (0.106)	-0.38	12.4	1.39
12-14	-0.010 (0.061)	-0.17	5.89	2.86
14-16	-0.076 (0.043)	-1.74	0.427	4.30
16-18	-0.047 (0.034)	-1.38	7.39	5.51
18-20	-0.040 (0.029)	-1.39	9.23	6.86
20-22	-0.0041 (0.025)	-0.16	7.19	8.18
22-24	-0.0063 (0.021)	-0.30	2.62	9.59
24-26	-0.027 (0.019)	-1.40	1.90	11.08
26-28	-0.0046 (0.017)	-0.27	2.19	12.15
28-30	-0.015 (0.017)	-0.93	0.338	13.98
30-32	-0.031 (0.018)	-1.70	2.19	14.83
32-34	-0.043 (0.017)	-2.55	1.90	16.13
34-36	-0.012 (0.019)	-0.63	2.61	16.66
36-38	-0.013 (0.021)	-0.61	1.53	16.66
38-40	-0.094 (0.019)	-0.48	0.855	16.66
40-42	-0.018 (0.017)	-1.09	0.161	16.66
42-44	-0.018 (0.014)	-1.23	0.352	16.66
44-46	-0.0044 (0.013)	-0.34	2.20	16.66
46-48	-0.0056 (0.012)	-0.46	1.31	16.66
48-50	-0.0054 (0.011)	-0.50	1.64	16.66
50-52	-0.0002 (0.011)	-0.02	2.78	16.66
52-54	0.0007 (0.012)	0.06	9.62	16.66
54-56	-0.012 (0.014)	-0.83	4.62	16.66
56-58	-0.0038 (0.014)	-0.27	4.30	16.66
58-60	-0.0056 (0.014)	-0.40	4.79	16.66
60-62	-0.0045 (0.015)	-0.30	1.14	16.66
62-64	-0.0083 (0.014)	-0.60	0.253	16.66
64-66	-0.011 (0.014)	-0.75	2.46	16.66
66-68	-0.0053 (0.015)	-0.37	1.70	16.66
68-70	-0.0001 (0.014)	-0.01	2.70	16.66

Table 5.3: Modulation amplitudes, with errors (1σ) and residuals, are provided for every energy slice. The fourth column contains the systematic errors induced by the time binning in units of 10^{-3} cpd/keV/kg (see section 5.4.2). The exposure depends on the energy interval because a given dataset-channel pair is considered in the analysis only if its analysis threshold is below the low energy boundary on the interval. See text for fit details.

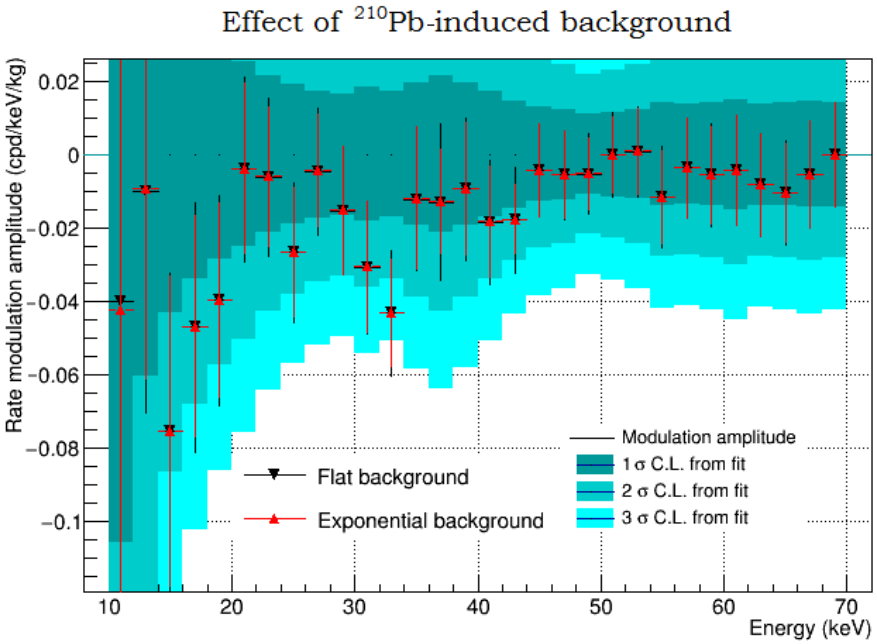

Figure 5.8: *Modulation amplitude spectrum obtained for different background models. All CUORE-0 channels have been used, with a time binning of 7.6 days. The $\chi^2_{90\%}$ cut (90% of signal acceptance) has been used. Black markers represents the modulation amplitude best values obtained by considering a flat background while the red markers show the amplitudes obtained by including a decaying background in the fit function (together with the flat component, see eq. 5.18). The decay time constant has been fixed to 32.03 years (i.e. ^{210}Pb decay time.*

where R_{Pb} is the ^{210}Pb-induced counting rate at the beginning of CUORE-0 data acquisition and $\tau = 22.20/(\ln 2)\ yr = 32.03\ yr$ is the decay time.

Figure 5.8 shows the comparison between the modulation amplitudes with (red triangles) and without (black triangles) this new component. In some fits, depending on energy and channel, the decaying background rate R_{Pb} is not compatible with zero. Nevertheless, even considering a decaying background, modulation amplitudes do not change.

5.4.2 Time binning effects

The systematic uncertainty induced by the time binning can be estimated by using different time binnings. Figure 5.9 shows a comparison between the amplitudes obtained by using bins of 7.6274, 15.2548 and 30.5096 days. The discrepancy between data points comes from the wrong assumption that detector duty cycle is constant during the period covered by a time bin. If,

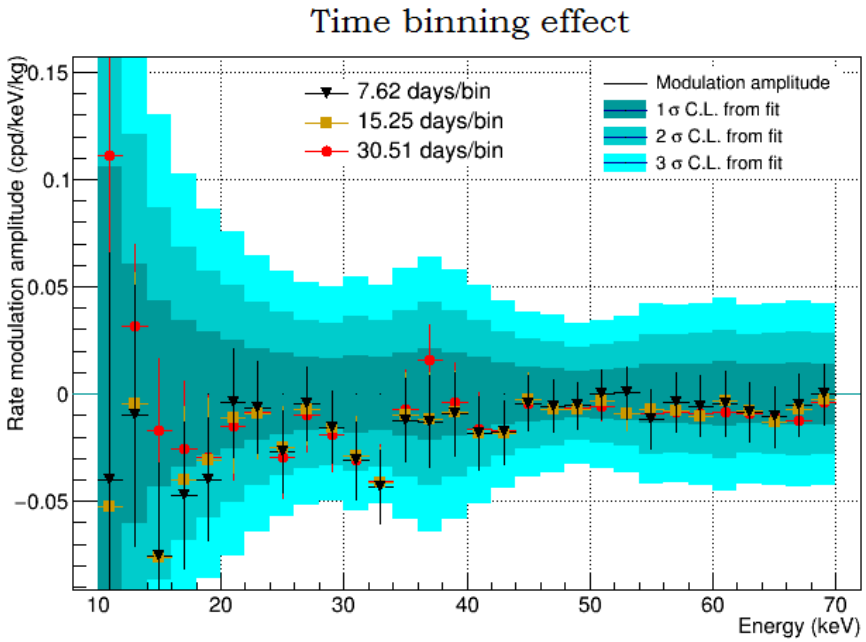

Figure 5.9: *Modulation amplitude spectrum obtained for different time binnings. All CUORE-0 channels have been considered, and $\chi^2_{90\%}$ cut (90% of signal acceptance) has been used to select the events. Three different time binnings have been considered: 7.63 days (black triangles), 15.25 days (yellow squares) and 30.51 days (red circles).*

for example, all the event of a given time bin have been acquired in the second half of that period, the event rate measured for that bin should be compared with the values that the fit function assumes in the second half of the bin instead of the entire bin. The smaller is the bin width the smaller is this effect so results obtained with smaller time binning must be considered more reliable. Nevertheless all values are compatible within less than half standard deviation. Systematic errors induced by this effect can be estimated, bin by bin, as the difference between the values obtained for 7.6 and 15.3 days. This value is well below the modulation uncertainty in every bin (see table 5.3).

5.4.3 χ^2_{OT}-cut acceptance effects

In order to investigate if the observed modulation is due to noise events a more conservative χ^2_{OT}-cut has been tested. In this case $\chi^2_{50\%}$, which is defined as the cut that provides a 50% signal acceptance, has been used.

This more conservative cut produces in general modulation amplitudes larger than the ones obtained from $\chi^2_{90\%}$-cut (figure 5.10, top). However their

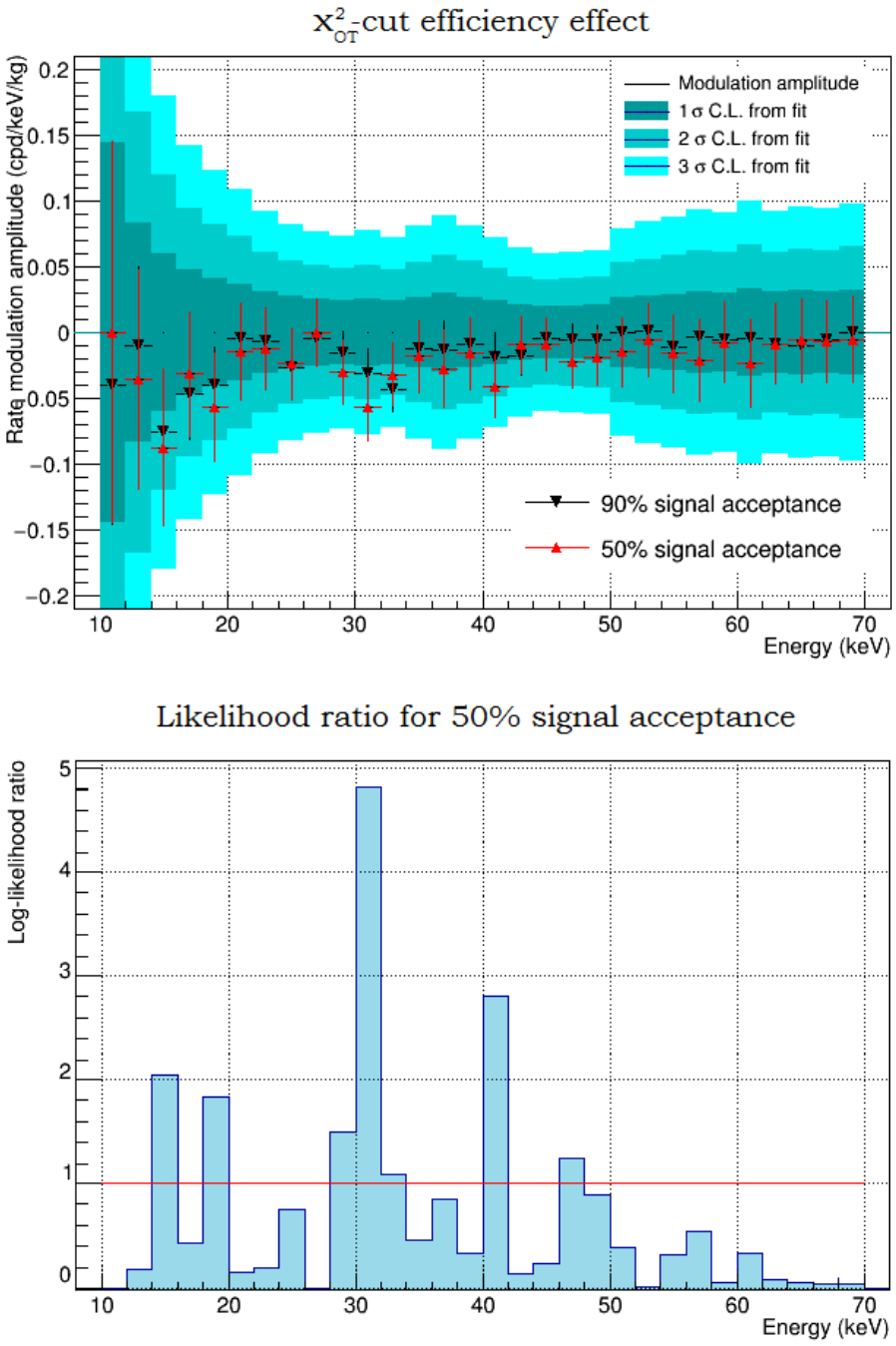

Figure 5.10: *Modulation amplitude spectrum obtained for different χ^2_{OT}-cuts. All CUORE-0 channels have been used, with a time binning of 7.6 days. The adopted cuts are $\chi^2_{90\%}$ (90% of signal acceptance, black triangles) and $\chi^2_{50\%}$ (50% of signal acceptance, red triangles). Uncertainty band (the blue bands) show the modulation amplitude uncertainty of data obtained from $\chi^2_{50\%}$. Since data from $\chi^2_{50\%}$ have less events than data from $\chi^2_{90\%}$, the uncertainty bands are wider for $\chi^2_{50\%}$ data (see fig. 5.7 for comparison).*

statistical significance is almost the same. In fact the $\chi^2_{50\%}$-cut has a smaller acceptance and thus removes more events from data. This effect produces larger uncertainties on the modulation amplitude. Such uncertainties are represented by the blue bands in fig.5.10 (top) from $\chi^2_{50\%}$ and fig. 5.7 (top) from $\chi^2_{90\%}$. The overall effect is that the statistical significance does not drastically change, as illustrated by the respective likelihood ratio test values (bottom plots of figures 5.7 and 5.10).

Conclusions

This Ph.D. thesis illustrates the search of annual modulation signal in the low energy region of CUORE-0 data. The main purpose of this analysis is the detection of Dark Matter according to the WIMP-induced nuclear recoil model which is expected to produce a modulating background in the 0 - 40 keV region (ROI).

A dedicated trigger algorithm, more efficient at low energy, has been used and a strong effort was put in the event selection. In particular, aside from the basic cut such as the multiplicity cut, a fundamental role is played by the χ^2_{OT}-cut. The value of χ^2_{OT} is evaluated for every pulse by fitting the pulse with a spline function describing the channel-dependent average pulse; it is used to define a selection box, in the χ^2_{OT} vs. energy plane, and reject non-physical signals in the ROI. The obtained CUORE-0 spectrum shows a rate ranging from 2 cpd/keV/kg at 10 keV to 0.1 cpd/keV/kg above 50 keV. It also shows two broad peaks between 30 and 40 keV whose origin is still unclear; they could come from the ^{210}Pb β-decay and this hypothesis has been considered in the modulation analysis. The exposure collected over a period of $\sim$15 months depends on the energy interval - the energy threshold is channel- and dataset-dependent - and ranges, after the cuts, from 1.39 kg·year to 16.66 kg·year above 34 keV.

The last part of the thesis describes the tests performed to identify possible sources of bias for the algorithm used to fit CUORE-0 counting rate with a cosine. Toy Monte Carlo simulations were used to understand, for example, how the pattern of the detector efficiency vs. time can affect fit results. No bias has been found even including the uncertainty of the χ^2_{OT}-cut efficiency.

An independent fit is performed, considering all CUORE-0 channels, for different 2-keV-wide intervals from 10 to 70 keV. Both phase and period have been fixed to the expected values according to the standard Dark Matter halo model (152.5 days and 365.25 days respectively). All fits but one returned negative amplitudes for the annual modulation signal. This fact, in principle, is in agreement with the expectation assuming heavy WIMPs ($\gtrsim$ 100 GeV). In total four intervals show amplitudes bigger than 1σ: 14 - 20 keV, 24 - 26

keV, 30 - 34 keV and 40 - 44 keV. In particular only the energy interval 32 - 34 keV, where a bump is visible in the CUORE-0 spectrum, shows a negative modulation amplitude bigger than 2σ. This correspondence suggests that the modulation signal, at lest at that energy, could be induced by a radioactive source. Moreover the obtained amplitudes are large if compared to the ones reported by the DAMA experiment. In conclusion, even if we see a weak signal of modulation its energy dependence and amplitude prevent us to conclude that it is induced by WIMPs.

Three aspects that can affect modulation results have been considered: the presence of a ^{210}Pb background, the time binning choice and the efficiency of χ^2_{OT}-cut. Modulation results do not change when including a background that exponentially decays over time to include possible ^{210}Pb activity. Different choices of time binning affect fit results but its systematic error has been estimated and resulted well below (roughly one order of magnitude) the statistical uncertainties returned by the fit. Finally the χ^2_{OT}-cut effect has been investigated by comparing the amplitude obtained with 50% and 90% signal acceptance cuts and finding almost coherent results. Nevertheless the dependency of modulation amplitude from the cut enhances the possibility to improve the data selection procedure for CUORE data.

In conclusion, the low exposure of CUORE-0 data prevents us to exclude that the observed modulation is due to effects different from Dark Matter. The CUORE experiment has a mass 19 times larger than the CUORE-0 one and will take data for a longer period. These two aspects, hopefully associated with a lower background (due to the detectors self shielding effect) and more stable operation conditions, will help to investigate the low energy region.

Even if this work is not conclusive from the DM search point of view, it gave the opportunity to face the issues related to this kind of analysis and represents a testing ground and a guideline for future analogue search in CUORE.

Bibliography

[1] C. Alduino *et al.*, "Analysis techniques for the evaluation of the neutrinoless double-β decay lifetime in ^{130}Te with the CUORE-0 detector," *Phys. Rev.*, vol. C93, no. 4, p. 045503, 2016.

[2] M. Agostini *et al.*, "Results on Neutrinoless Double-β Decay of ^{76}Ge from Phase I of the GERDA Experiment," *Phys. Rev. Lett.*, vol. 111, no. 12, p. 122503, 2013.

[3] J. B. Albert *et al.*, "Search for Majorana neutrinos with the first two years of EXO-200 data," *Nature*, vol. 510, pp. 229–234, 2014.

[4] A. Gando *et al.*, "Limit on Neutrinoless $\beta\beta$ Decay of ^{136}Xe from the First Phase of KamLAND-Zen and Comparison with the Positive Claim in ^{76}Ge," *Phys. Rev. Lett.*, vol. 110, no. 6, p. 062502, 2013.

[5] S. Dell'Oro, S. Marcocci, M. Viel, and F. Vissani, "Neutrinoless double beta decay: 2015 review," *Adv. High Energy Phys.*, vol. 2016, p. 2162659, 2016.

[6] P. collaboration, "Planck 2015 results," *Astronomy and astrophysics*, vol. 594, 2016.

[7] M. Martinez, "CUORE-0 sensitivity to WIMP annual modulation and CUORE prospects," cuore collaboration internal report, 2016.

[8] R. Bernabei *et al.*, "First results from DAMA/LIBRA and the combined results with DAMA/NaI," *Eur. Phys. J.*, vol. C56, pp. 333–355, 2008.

[9] C. Patrignani *et al.*, "Review of Particle Physics," *Chin. Phys.*, vol. C40, no. 10, p. 100001, 2016.

[10] F. Alessandria *et al.*, "The 4K outer cryostat for the CUORE experiment: Construction and quality control," *Nucl. Instrum. Meth.*, vol. A727, pp. 65–72, 2013.

[11] C. Alduino *et al.*, "CUORE-0 detector: design, construction and operation," *JINST*, vol. 11, no. 07, p. P07009, 2016.

[12] S. Di Domizio, F. Orio, and M. Vignati, "Lowering the energy threshold of large-mass bolometric detectors," *JINST*, vol. 6, p. P02007, 2011.

[13] G. Piperno, *Dark Matter search with the CUORE-0 experiment.* PhD thesis, Sapienza, Università di Roma, 2015.

[14] P. Mosteiro, K. Lim, G. Piperno, S. Copello, L. Marini, and M. Martinez, "Cuore-0 low-energy data processing," cuore collaboration internal report, 2016.

[15] M. C. Gonzalez-Garcia, M. Maltoni, and T. Schwetz, "Global Analyses of Neutrino Oscillation Experiments," *Nucl. Phys.*, vol. B908, pp. 199–217, 2016.

[16] S. Y. F. Chu *et al.*, "The lund/lbnl nuclear data search." http://nucleardata.nuclear.lu.se/toi/.

[17] M. Goeppert-Mayer, "Double beta-disintegration," *Phys. Rev.*, vol. 48, pp. 512–516, 1935.

[18] W. H. Furry, "On transition probabilities in double beta-disintegration," *Phys. Rev.*, vol. 56, pp. 1184–1193, 1939.

[19] M. G. Inghram and J. H. Reynolds, "Double beta-decay of Te-130," *Phys. Rev.*, vol. 78, pp. 822–823, 1950.

[20] M. Goldhaber, L. Grodzins, and A. W. Sunyar, "Helicity of Neutrinos," *Phys. Rev.*, vol. 109, pp. 1015–1017, 1958.

[21] R. Davis, Jr., D. S. Harmer, and K. C. Hoffman, "Search for neutrinos from the sun," *Phys. Rev. Lett.*, vol. 20, pp. 1205–1209, 1968.

[22] Y. Fukuda *et al.*, "Evidence for oscillation of atmospheric neutrinos," *Phys. Rev. Lett.*, vol. 81, pp. 1562–1567, 1998.

[23] Q. R. Ahmad *et al.*, "Measurement of the rate of $\nu_e + d \rightarrow p + p + e^-$ interactions produced by ^8B solar neutrinos at the Sudbury Neutrino Observatory," *Phys. Rev. Lett.*, vol. 87, p. 071301, 2001.

[24] T. Araki *et al.*, "Measurement of neutrino oscillation with KamLAND: Evidence of spectral distortion," *Phys. Rev. Lett.*, vol. 94, p. 081801, 2005.

[25] M. C. Gonzalez-Garcia and Y. Nir, "Neutrino masses and mixing: Evidence and implications," *Rev. Mod. Phys.*, vol. 75, pp. 345–402, 2003.

[26] P. Adamson *et al.*, "Measurement of Neutrino and Antineutrino Oscillations Using Beam and Atmospheric Data in MINOS," *Phys. Rev. Lett.*, vol. 110, no. 25, p. 251801, 2013.

[27] P. Adamson *et al.*, "Electron neutrino and antineutrino appearance in the full MINOS data sample," *Phys. Rev. Lett.*, vol. 110, no. 17, p. 171801, 2013.

[28] K. Abe *et al.*, "Precise measurement of the neutrino mixing parameter θ_{23} from muon neutrino disappearance in an off-axis beam," *Phys. Rev. Lett.*, vol. 112, no. 18, p. 181801, 2014.

[29] K. Abe *et al.*, "Observation of Electron Neutrino Appearance in a Muon Neutrino Beam," *Phys. Rev. Lett.*, vol. 112, p. 061802, 2014.

[30] L. Kolupaeva, "Current results of the NOvA experiment," *EPJ Web Conf.*, vol. 125, p. 01002, 2016.

[31] K. Nakamura *et al.*, "Review of particle physics," *J. Phys.*, vol. G37, p. 075021, 2010.

[32] K. N. Abazajian *et al.*, "Cosmological and Astrophysical Neutrino Mass Measurements," *Astropart. Phys.*, vol. 35, pp. 177–184, 2011.

[33] N. Palanque-Delabrouille *et al.*, "Constraint on neutrino masses from SDSS-III/BOSS Lyα forest and other cosmological probes," *JCAP*, vol. 1502, no. 02, p. 045, 2015.

[34] F. Simkovic, V. Rodin, A. Faessler, and P. Vogel, "$0\nu\beta\beta$ and $2\nu\beta\beta$ nuclear matrix elements, quasiparticle random-phase approximation, and isospin symmetry restoration," *Phys. Rev.*, vol. C87, no. 4, p. 045501, 2013.

[35] J. Menendez, A. Poves, E. Caurier, and F. Nowacki, "Disassembling the Nuclear Matrix Elements of the Neutrinoless beta beta Decay," *Nucl. Phys.*, vol. A818, pp. 139–151, 2009.

[36] J. Barea, J. Kotila, and F. Iachello, "$0\nu\beta\beta$ and $2\nu\beta\beta$ nuclear matrix elements in the interacting boson model with isospin restoration," *Phys. Rev.*, vol. C91, no. 3, p. 034304, 2015.

[37] H. V. Klapdor-Kleingrothaus and I. V. Krivosheina, "The evidence for the observation of 0nu beta beta decay: The identification of 0nu beta beta events from the full spectra," *Mod. Phys. Lett.*, vol. A21, pp. 1547–1566, 2006.

[38] A. Gando *et al.*, "Search for Majorana Neutrinos near the Inverted Mass Hierarchy Region with KamLAND-Zen," *Phys. Rev. Lett.*, vol. 117, no. 8, p. 082503, 2016. [Addendum: Phys. Rev. Lett.117,no.10,109903(2016)].

[39] R. Arnold *et al.*, "Results of the search for neutrinoless double-beta decay in ^{100}Mo with the NEMO-3 experiment," *Phys. Rev.*, vol. D92, no. 7, p. 072011, 2015.

[40] J. Mott, *Search for double beta decay of ^{82}Se with the NEMO-3 detector and development of apparatus for low-level radon measurements for the SuperNEMO experiment.* PhD thesis, University Coll. London, 2013-09-25.

[41] R. Arnold *et al.*, "Measurement of the double-beta decay half-life and search for the neutrinoless double-beta decay of ^{48}Ca with the NEMO-3 detector," *Phys. Rev.*, vol. D93, no. 11, p. 112008, 2016.

[42] R. Arnold *et al.*, "Measurement of the $2\nu\beta\beta$ Decay Half-Life and Search for the $0\nu\beta\beta$ Decay of ^{116}Cd with the NEMO-3 Detector," 2016.

[43] R. Arnold *et al.*, "Measurement of the $2\nu\beta\beta$ decay half-life of ^{150}Nd and a search for $0\nu\beta\beta$ decay processes with the full exposure from the NEMO-3 detector," *Phys. Rev.*, vol. D94, no. 7, p. 072003, 2016.

[44] R. Arnold *et al.*, "Probing New Physics Models of Neutrinoless Double Beta Decay with SuperNEMO," *Eur. Phys. J.*, vol. C70, pp. 927–943, 2010.

[45] K. Alfonso *et al.*, "Search for Neutrinoless Double-Beta Decay of ^{130}Te with CUORE-0," *Phys. Rev. Lett.*, vol. 115, no. 10, p. 102502, 2015.

[46] F. Zwicky, "The Redshift of Extragalactic Nebulae," *Helv. Phys. Acta*, vol. 6, pp. 110–127, 1933.

[47] H. Boehringer and G. Chon, "Constraints on neutrino masses from the study of the nearby large-scale structure and galaxy cluster counts," *Mod. Phys. Lett.*, vol. 31, p. 1640008, 2016.

[48] V. Trimble, "Existence and Nature of Dark Matter in the Universe," *Ann. Rev. Astron. Astrophys.*, vol. 25, pp. 425–472, 1987.

[49] D. Clowe, M. Bradac, A. H. Gonzalez, M. Markevitch, S. W. Randall, C. Jones, and D. Zaritsky, "A direct empirical proof of the existence of dark matter," *Astrophys. J.*, vol. 648, pp. L109–L113, 2006.

[50] M. Bradac, D. Clowe, A. H. Gonzalez, P. Marshall, W. Forman, C. Jones, M. Markevitch, S. Randall, T. Schrabback, and D. Zaritsky, "Strong and weak lensing united III: Measuring the mass distribution of the merging galaxy cluster 1E0657-56," *Astrophys. J.*, vol. 652, pp. 937–947, 2006.

[51] R. Wilson and A. Penzias, "Isotropy of Cosmic Background Radiation at 408 Megahertz," *Science*, vol. 156, pp. 1100–1101, 1967.

[52] R. Catena and P. Ullio, "A novel determination of the local dark matter density," *JCAP*, vol. 1008, p. 004, 2010.

[53] L. Wyrzykowski *et al.*, "The OGLE View of Microlensing towards the Magellanic Clouds. IV. OGLE-III SMC Data and Final Conclusions on MACHOs," *Mon. Not. Roy. Astron. Soc.*, vol. 416, p. 2949, 2011.

[54] M. Milgrom, "A Modification of the Newtonian dynamics as a possible alternative to the hidden mass hypothesis," *Astrophys. J.*, vol. 270, pp. 365–370, 1983.

[55] M. Milgrom, "MOND theory," *Can. J. Phys.*, vol. 93, no. 2, pp. 107–118, 2015.

[56] D. H. Weinberg, J. S. Bullock, F. Governato, R. Kuzio de Naray, and A. H. G. Peter, "Cold dark matter: controversies on small scales," *Proc. Nat. Acad. Sci.*, vol. 112, pp. 12249–12255, 2014.

[57] G. Bertone *et al.*, *Particle Dark Matter: Observations, Models and Searches*. 2010.

[58] G. Servant and T. M. P. Tait, "Is the lightest Kaluza-Klein particle a viable dark matter candidate?," *Nucl. Phys.*, vol. B650, pp. 391–419, 2003.

[59] S. Profumo, F. S. Queiroz, and C. E. Yaguna, "Extending Fermi-LAT and H.E.S.S. Limits on Gamma-ray Lines from Dark Matter Annihilation," 2016.

[60] J. F. Navarro, C. S. Frenk, and S. D. M. White, "The Structure of cold dark matter halos," *Astrophys. J.*, vol. 462, pp. 563–575, 1996.

[61] J. Einasto, "On the Construction of a Composite Model for the Galaxy and on the Determination of the System of Galactic Parameters," *Trudy Astrofizicheskogo Instituta Alma-Ata*, vol. 5, pp. 87–100, 1965.

[62] M. G. Aartsen *et al.*, "Search for annihilating dark matter in the Sun with 3 years of IceCube data," 2016.

[63] F. Halzen *et al.*, "The AMANDA neutrino telescope and the indirect search for dark matter," *Phys. Rept.*, vol. 307, pp. 243–252, 1998.

[64] T. Tanaka *et al.*, "An Indirect Search for WIMPs in the Sun using 3109.6 days of upward-going muons in Super-Kamiokande," *Astrophys. J.*, vol. 742, p. 78, 2011.

[65] K. Bechtol *et al.*, "Eight New Milky Way Companions Discovered in First-Year Dark Energy Survey Data," *Astrophys. J.*, vol. 807, no. 1, p. 50, 2015.

[66] A. Drlica-Wagner *et al.*, "Search for Gamma-Ray Emission from DES Dwarf Spheroidal Galaxy Candidates with Fermi-LAT Data," *Astrophys. J.*, vol. 809, no. 1, p. L4, 2015.

[67] D. G. Cerdeno and A. M. Green, "Direct detection of WIMPs," 2010.

[68] F. J. Kerr and D. Lynden-Bell, "Review of galactic constants," *Mon. Not. Roy. Astron. Soc.*, vol. 221, p. 1023, 1986.

[69] M. Feast and P. Whitelock, "Galactic kinematics of cepheids from hipparcos proper motions," *Mon. Not. Roy. Astron. Soc.*, vol. 291, pp. 683–693, 1997.

[70] J. D. Lewin and P. F. Smith, "Review of mathematics, numerical factors, and corrections for dark matter experiments based on elastic nuclear recoil," *Astropart. Phys.*, vol. 6, pp. 87–112, 1996.

[71] C. Kouvaris and N. G. Nielsen, "Daily modulation and gravitational focusing in direct dark matter search experiments," *Phys. Rev.*, vol. D92, no. 7, p. 075016, 2015.

[72] A. Bandyopadhyay and D. Majumdar, "On Diurnal and Annual Variations of Directional Detection Rates of Dark Matter," *Astrophys. J.*, vol. 746, p. 107, 2012.

[73] M. L. Sarsa, A. Morales, J. Morales, E. Garcia, A. Ortiz de Solorzano, J. Puimedon, C. Saenz, A. Salinas, and J. A. Villar, "A search for

annual and daily modulations of dark matter with NaI scintillators at Canfranc," *Nucl. Phys. Proc. Suppl.*, vol. 48, pp. 73–76, 1996.

[74] C. E. Aalseth *et al.*, "Results from a Search for Light-Mass Dark Matter with a P-type Point Contact Germanium Detector," *Phys. Rev. Lett.*, vol. 106, p. 131301, 2011.

[75] J. H. Davis, C. McCabe, and C. Boehm, "Quantifying the evidence for Dark Matter in CoGeNT data," *JCAP*, vol. 1408, p. 014, 2014.

[76] Q. Yue *et al.*, "Limits on light WIMPs from the CDEX-1 experiment with a p-type point-contact germanium detector at the China Jingping Underground Laboratory," *Phys. Rev.*, vol. D90, p. 091701, 2014.

[77] R. Bernabei *et al.*, "DAMA/LIBRA–phase1 model independent results," *Int. J. Mod. Phys.*, vol. A31, no. 31, p. 1642006, 2016.

[78] R. Bernabei *et al.*, "No role for neutrons, muons and solar neutrinos in the DAMA annual modulation results," *Eur. Phys. J.*, vol. C74, no. 12, p. 3196, 2014.

[79] F. Froborg, "SABRE: WIMP modulation detection in the northern and southern hemisphere," *J. Phys. Conf. Ser.*, vol. 718, no. 4, p. 042021, 2016.

[80] N. Bozorgnia and T. Schwetz, "What is the probability that direct detection experiments have observed Dark Matter?," *JCAP*, vol. 1412, no. 12, p. 015, 2014.

[81] K. Abe *et al.*, "Direct dark matter search by annual modulation in XMASS-I," *Phys. Lett.*, vol. B759, pp. 272–276, 2016.

[82] E. Aprile *et al.*, "Dark Matter Results from 225 Live Days of XENON100 Data," *Phys. Rev. Lett.*, vol. 109, p. 181301, 2012.

[83] D. S. Akerib *et al.*, "First results from the LUX dark matter experiment at the Sanford Underground Research Facility," *Phys. Rev. Lett.*, vol. 112, p. 091303, 2014.

[84] G. Angloher *et al.*, "Results from 730 kg days of the CRESST-II Dark Matter Search," *Eur. Phys. J.*, vol. C72, p. 1971, 2012.

[85] G. Angloher *et al.*, "Results on light dark matter particles with a low-threshold CRESST-II detector," *Eur. Phys. J.*, vol. C76, no. 1, p. 25, 2016.

[86] R. Agnese *et al.*, "Silicon Detector Dark Matter Results from the Final Exposure of CDMS II," *Phys. Rev. Lett.*, vol. 111, no. 25, p. 251301, 2013.

[87] R. Agnese *et al.*, "Search for Low-Mass Weakly Interacting Massive Particles with SuperCDMS," *Phys. Rev. Lett.*, vol. 112, no. 24, p. 241302, 2014.

[88] E. Fiorini and T. O. Niinikoski, "Low Temperature Calorimetry for Rare Decays," *Nucl. Instrum. Meth.*, vol. A224, p. 83, 1984.

[89] E. Andreotti *et al.*, "130Te Neutrinoless Double-Beta Decay with CUORICINO," *Astropart. Phys.*, vol. 34, pp. 822–831, 2011.

[90] E. Buccheri, M. Capodiferro, S. Morganti, F. Orio, A. Pelosi, and V. Pettinacci, "An assembly line for the construction of ultra-radiopure detectors," *Nucl. Instrum. Meth.*, vol. A768, pp. 130–140, 2014.

[91] C. Ligi *et al.*, "The CUORE Cryostat: A 1-Ton Scale Setup for Bolometric Detectors," *J. Low. Temp. Phys.*, vol. 184, no. 3-4, pp. 590–596, 2016.

[92] A. Alessandrello *et al.*, "Measurements of internal radioactive contamination in samples of Roman lead to be used in experiments on rare events," *Nucl. Instrum. Meth. B*, vol. 142, pp. 163–172, 1998.

[93] J. S. Cushman *et al.*, "The detector calibration system for the CUORE cryogenic bolometer array," *Nucl. Instrum. Meth.*, vol. A844, pp. 32–44, 2017.

[94] TDK-Lambda web page. http://www.us.tdk-lambda.com/hp/product_html/genesys1u.htm.

[95] Keithley web page. http://www.tek.com/tektronix-and-keithley-dc-power-supplies/keithley-2220-2230-2231-series.

[96] Scientific Linux web page. https://www.scientificlinux.org/.

[97] National Instruments, PXI-6284 digitizers board web page. http://sine.ni.com/nips/cds/view/p/lang/it/nid/14120.

[98] National Instruments, PXI-1044 chassis web page. http://sine.ni.com/nips/cds/view/p/lang/it/nid/14561.

[99] National Instruments, MXI-4 Series controller board user manual. http://www.ni.com/pdf/manuals/370840b.pdf.

[100] S. Di Domizio, *Search for double beta decay to excited states with CUORICINO and data acquisition system for CUORE*. PhD thesis, Università degli studi di Genova, 2009.

[101] E. Gatti and P. F. Manfredi, "Processing the Signals From Solid State Detectors in Elementary Particle Physics," *Riv. Nuovo Cim.*, vol. 9N1, pp. 1–146, 1986.

[102] A. Alessandrello *et al.*, "The thermal detection efficiency for recoils induced by low-energy nuclear reactions, neutrinos or weakly interacting massive particles," *Phys. Lett.*, vol. B408, pp. 465–468, 1997.

[103] K. E. Lim, "Nuclear quenching factor of TeO_2 measured in CUORE-0," cuore collaboration internal report, 2016.

[104] A. Agresti and C. B. A., "Approximate Is Better than "Exact" for Interval Estimation of Binomial Proportions," *The American Statistician*, vol. 52, pp. 119–126, 1998.

[105] K. E. Lim, "CUORE-0 Cut Efficiency Evalution," cuore collaboration internal report, 2016.

[106] S. Baker and R. D. Cousins, "Clarification of the Use of Chi Square and Likelihood Functions in Fits to Histograms," *Nucl. Instrum. Meth.*, vol. 221, pp. 437–442, 1984.